Interaction of low-level cloud and sea surface temperature around oceanic frontal region in summertime North Pacific

Doctoral Thesis

Interaction of low-level cloud and sea surface temperature around oceanic frontal region in summertime North Pacific

Naoya Takahashi

Department of Geophysics
Graduate School of Science
Tohoku University

Supervisor

Professor Tadahiro Hayasaka

Thesis Committee Members

Professor Toshio Suga (Chair)
Professor Tadahiro Hayasaka
Professor Takeshi Yamazaki
Associate Professor Hironobu Iwabuchi
Professor Bo Qiu (University of Hawaii at Manoa)
Professor Kelvin Richards (University of Hawaii at Manoa)
Professor Niklas Schneider (University of Hawaii at Manoa)

2019

博士論文

夏季北太平洋における海洋前線帯周辺の下層雲と海面水温の相互作用に関する研究

東北大学大学院理学研究科
地球物理学専攻

高橋　直也

指導教員

早坂　忠裕　教授

論文審査委員

須賀　利雄	教授（主査）
早坂　忠裕	教授
山崎　剛	教授
岩渕　弘信	准教授
Bo Qiu	教授（ハワイ大学マノア校）
Kelvin Richards	教授（ハワイ大学マノア校）
Niklas Schneider	教授（ハワイ大学マノア校）

令和元年

Abstract

Oceanic low-level clouds play a key role in modulating the Earth's radiation budget, which generally have strong cooling effect due to their large albedo and warm cloud top temperature. Variability of the low-level cloud interacts strongly with the sea surface temperature (SST) via two-way physical processes between them. Through the stratification process of the atmospheric boundary layer, decreasing SST promotes the low-level cloud formation, which promotes cooling of the sea surface itself by more reflection of the solar radiation by the low-level cloud. As a result, a positive feedback exists between the radiative impact of the low-level cloud and SST, especially in summertime North Pacific (NP). Main problem about the relationship is "a dependence on timescale for a key trigger of the positive feedback loop, particularly for the role of SST". Thus, we investigated the causal relationship between the low-level cloud properties and SST on various timescales based on the observational data analysis and numerical experiments using atmospheric regional model. We mainly focused on three timescales; 1) synoptic, 2) intra-seasonal, and 3) inter-annual. The goal of this study is to advance our understanding of the two-way processes and its timescale dependence in summertime NP.

First, we investigated the two-way physical processes on an intra-seasonal timescale in summertime (June to October) North Pacific (165-175˚E and 30-40˚N) based on satellite observational and reanalysis datasets from 2003 to 2016. The intra-seasonal timescale (20-100 days) is dominant not only for the low-level cloud cover (LCC), but also for LCC controlling factors such as SST, estimated inversion strength (EIS), and horizontal temperature advection (T_{adv}). Thus, there is a possibility of the two-way process between LCC and SST on this timescale. To reveal the detailed lead-lag relationship among these variables, we conducted phase composite analysis with a bandpass filter based on the intra-seasonal variability of LCC. The composite analysis suggests that intra-seasonal variability of LCC precedes to that of SST, and that horizontal dry-cold advection from the poleward region is a trigger for increasing LCC and decreasing SST. The increase of LCC anomaly corresponds to a positive relative humidity anomaly which is due to the decreasing saturated water vapor pressure by anomalous cold temperature advection within the boundary layer. Heat budget analysis of the ocean mixed-layer suggests that the horizontal dry-cold advection cools SST not only by enhancing latent heat release but also by decreasing downward shortwave radiation at the sea surface through a positive LCC anomaly. Determining the detailed lead-lag relationship between LCC and its controlling factors is an effective approach to understand the mechanisms of both low-level cloud evolution and air–sea interaction.

Second, we investigated the active role of the SST front in modulating oceanic low-level cloud properties in the Oyashio Extension during summertime based on a Weather Research and Forecasting numerical simulation. It is known that the SST front in wintertime modulate the

atmospheric variability in the mid-latitudes, but it is not known whether the SST front in summertime does. To reveal the impact of SST anomaly associated with the front on the low-level cloud, we conducted two experiments with different bottom boundary conditions. The first was constrained by 0.25° daily SST data from July to August 2016 (CTL experiment) and the second by spatially smoothed SST without SST frontal characteristics in the same period (SMO experiment). The period-mean cloud water mixing ratio of marine fog near the sea surface in the CTL experiment was larger than that in the SMO experiment by 20%–40% on the northern flank of the SST front. This result indicated that the SST front affected the mean-state of the low-level cloud properties. The SST front also affected the synoptic variability of low-level cloud, and the magnitude of the effect depended on the meridional wind across the SST front. We found two competing physical processes modulating the marine fog properties around the SST front. First, a local cold SST anomaly on the northern flank reduced the saturated water vapor pressure near the surface, which are favorable for the marine fog formation (SST anomaly effect). Second, horizontal temperature advection from the warm to cold flanks of the SST front suppressed the marine fog formation, and the suppression was effective when the horizontal gradient of SST anomaly was large (SST frontal effect). Thus, the overall impact of the SST front on the marine fog properties depended on the local SST anomaly, the meridional wind across the front position, and the horizontal gradient of SST. Our results indicated the importance of SST frontal characteristics in summertime Oyashio Extension for the marine fog formation.

Finally, we investigated the active role of the variation of the summertime Oyashio Extension SST front in modulating low-level cloud properties (LCC, cloud optical thickness [COT], and shortwave cloud radiative effect [SWCRE]) on an inter-annual timescale, based on various observational datasets during 2003–2016. First, we examined the mechanism of summertime SST front variability. The strength of the SST front (S_{SSTF}), defined as the maximum horizontal gradient of SST, has clear inter-annual variations. Frontogenesis equation analysis and regression analysis for oceanic subsurface temperature indicated that the inter-annual variation of the summertime S_{SSTF} in the western North Pacific is strongly related to variabilities in the Kuroshio and Oyashio Extensions but not surface heat flux. The response of low-level cloud to intensified the S_{SSTF} is that positive (negative) SWCRE with smaller LCC (larger COT) on the southern (northern) flank of the SST front which is induced by warm (cold) SST anomalies. The spatial scale of the low-level cloud response was larger than the SST frontal scale (~300 km), and the responses were strongly localized over the western boundary currents (i.e., Kuroshio and Oyashio Currents). The SST played the largest role in modulating low-level cloud among the controlling factors (i.e., EIS, T_{adv}) accounting for more than 40% of the variation. This implies the presence of active SST role in summertime. Using combined datasets, the present study provides observational evidence for the active role of summertime SST anomalies in the Oyashio and Kuroshio Extensions. Entire results in the present study provides new insight into two-way physical processes between low-level cloud and SST in the mid-latitudes.

Contents

Abstract i

Contents iii

1. General Introduction 1

1.1 Background 1

1.2 Unresolved problems 4

1.2.1 Causal relationship between low-level cloud and SST 4

1.2.2 Timescale of cloud and SST variabilities 8

1.3 Objective of this study 10

2. Intra-Seasonal Variability of Low-Level Cloud and Sea Surface Temperature in Summertime North Pacific based on MODIS Satellite Observation 13

2.1 Introduction 13

2.2 Data and Methods 15

2.2.1 Data 15

2.2.2 Methods 17

2.3 Results 19

2.3.1 Dominant timescale of low-level cloud cover (LCC) variability in summertime North Pacific (NP) 19

2.3.2 Characteristics of the intra-seasonal variability (ISV) of LCC 21

2.3.3 Mechanism of evolution of LCC and changes in humidity field 27

2.3.4 Air-sea interaction process between low-level cloud and SST associated with the ISV of LCC 29

2.4 Discussion and Summary 34

Appendix 2A : Random overlap assumption for daily-mean dataset of MODIS 36

Appendix 2B : Temperature budget analysis in the atmospheric boundary layer 37

3. Active role of Oyashio Extension SST Front for Modulating Summertime Oceanic Low-Level Cloud based on WRF Numerical Experiments 39

3.1 Introduction 39

3.2 Data and Methods 41

3.2.1 Atmospheric Regional Weather Research and Forecasting Model 41

3.2.2 Experimental design 42

3.2.3 Comparison of low-level cloud in the WRF model output with the observational dataset 43

3.3 Results 45

3.3.1 Impacts of SST front on the mean state of low-level cloud 45

3.3.2 Impacts of SST front on the synoptic variability of low-level cloud 48

3.3.3 Mechanism of the impacts of SST front on marine fog with northerly or southerly; SST anomaly effect vs SST frontal effect 54

3.4 Discussion and Summary 60

Appendix 3A : Sensitivity of low-level cloud properties to PBL schemes 62

4. Observed Low-Level Cloud Response to Inter-Annual Variation of the Strength of Oyashio Extension SST Front in Summertime 63

4.1 Introduction 63

4.2 Data and Methods 67

4.2.1 Data 67

4.2.2 Methods 69

4.3 Mechanism of SST front variations in summertime western NP 70

4.3.1 Climatology of SST front in summertime (JJA) from 2003 to 2016 70

4.3.2 Inter-annual variations of the SST fronts and subsurface temperature 71

4.3.3 Mechanisms of frontogenesis in Isoguchi Jet 2 (IJ2) region; atmospheric forcing vs oceanic forcing 74

4.4 Response of summertime low-level cloud properties to the strength of the SST front (S_{SSTF}) in the IJ2 region 77

4.5 Discussion and Summary 83

5. General Conclusion and Future Prospects 87

References 91

Acknowledgements 104

Chapter 1

General Introduction

1.1 Background

Climate in the Earth is determined by the balance of shortwave (SW) radiation from the sun and longwave (LW) radiation emitted from the Earth (Fig 1.1). Albedo, defined as the fraction of incoming SW radiation that is reflected, is a key parameter to modify the incoming radiation absorbed in the climate system. The albedo is mainly constrained by surface condition such as snow cover, aerosol, and cloud optical properties. For determining the outgoing LW radiation, it is important how much the atmospheric gas absorb the emitted radiation from the surface and re-emit it to the space. Major atmospheric components to modify the LW radiative flux are water vapor and carbon dioxide. Cloud can also significantly modulate the LW radiation. Therefore, clouds have the significant impact on the radiation budget to regulate both of SW and LW radiative fluxes in the climate system. Radiative impact of cloud is called cloud radiative effect (CRE), which is defined as the difference between cloudy-sky and clear-sky downward radiative flux. There are two types of CREs: SW and LW CREs. The former one indicates how much SW radiation from the sun is reflected by the cloud, it is always negative and exerts cooling effect. While the latter one indicates how much LW radiation that emitted by the Earth's surface and atmosphere is prevented from escaping into the space by cloud, LW CRE is positive and has warming effect. The net CRE is expressed as the sum of the SW and LW CREs. As shown in Fig 1.1, SW and LW radiations are balanced at the top of atmosphere (TOA). SW and LW CREs, however, do not have the same magnitude. The SW CRE with cooling effect tends to be larger than the LW CRE with warming effect (Harrison et al., 1990; Ramanathan et al., 1989), as shown in Fig. 1.2. Thus, the global annual average of net CRE based on the satellite observations is estimated as negative value.

Besides, the magnitude and sign of the net CRE depend on season, region (i.e. tropics, mid-latitude, polar region), and cloud type (Fig. 1.3). In terms of cloud type, low-level clouds (e.g. stratus, stratocumulus) generally have strong cooling effect due to their large albedo and warm cloud top temperature. On the other hand, optically thin mid- and high-level clouds (e.g. cirrus, altostratus) tend to have warming effect because of their cold cloud top temperature. Deep convective clouds (e.g.

cumulonimbus) with large albedo and cold cloud top temperature has both of cooling and warming effect, which could almost cancel each other. Overall, the net CREs are primarily determined by the cloud optical thickness and cloud top temperature.

The net CREs also depend on the cloud occurrence frequency, which is normally referred as "cloud fraction" or "cloud cover". Fig. 1.4 shows the maps of climatological-mean low-level cloud cover (LCC), mid-level cloud (MCC), high-level cloud (HCC), and total cloud cover (TCC), estimated by the Moderate Resolution Imaging Spectroradiometer (MODIS) observation. Those three types of clouds are classified by their cloud top pressure (CTP): low-level (680 hPa≤ CTP <1000 hPa), mid-level (440 hPa≤ CTP <680 hPa), and high-level (CTP <440 hPa). For the impact of the cloud occurrence frequency on the net CRE, cloud coverage of the low-level cloud dominates over the other two cloud types as it composes at least 40% of the total cloud coverage (Fig. 1.4). Among the low-level clouds, oceanic stratiform clouds (i.e. stratus, stratocumulus, fog) are suggested as the most horizontally-extensive clouds, compared with other low-level clouds such as cumuliform and cirriform clouds. In this context, it is important to get a thorough understanding of the variation and modulation/response/feedback mechanisms of the oceanic low-level cloud, for further quantitative investigation of the climate variability.

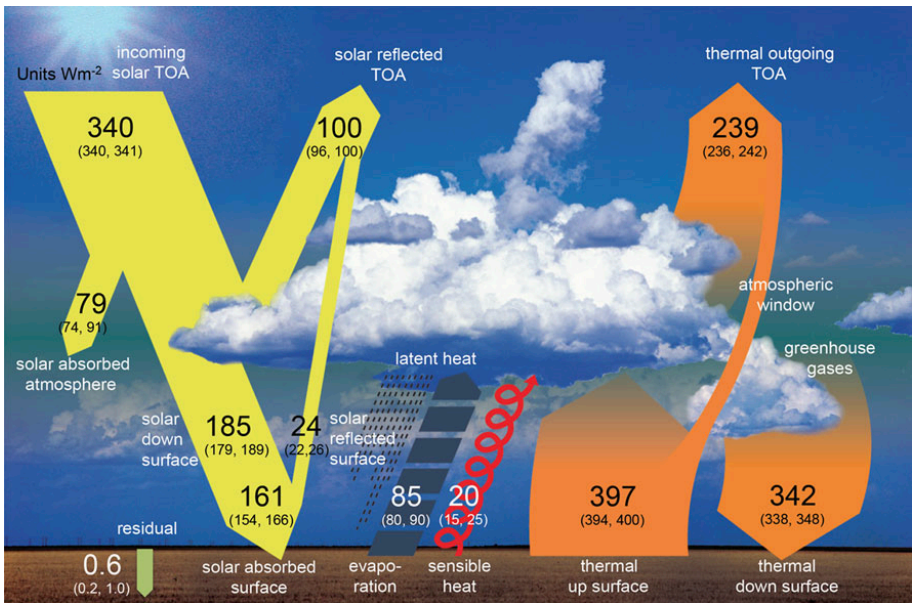

Fig. 1.1 Schematic diagram of the global mean energy balance of the Earth. Numbers indicate the best estimates for the magnitudes of the globally averaged energy balance components together with their uncertainty ranges, representing present-day climate conditions at the beginning of the twenty first century. Units is Wm^{-2}. Adapted from Wild et al. (2013).

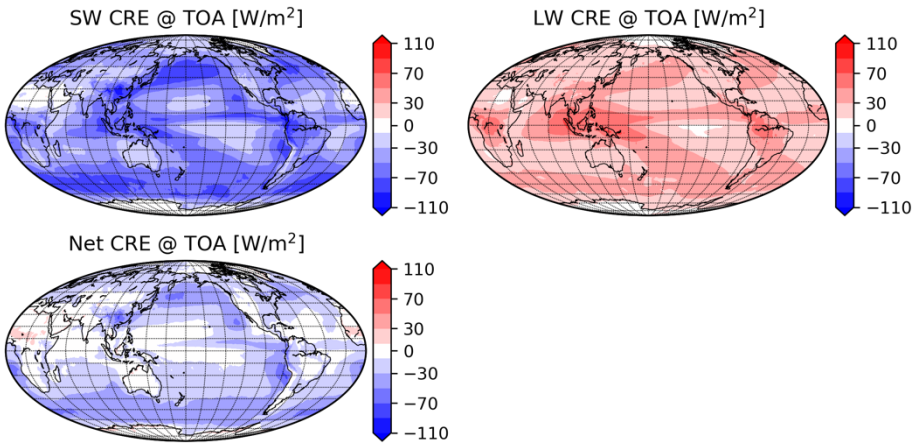

Fig. 1.2 Climatology of SW CRE (upper left), LW CRE (upper right), and Net CRE (lower left) based on CERES observations from July 2005to June 2015. Downward flux is defined as positive; Red (Blue) color indicates warming (cooling) effect.

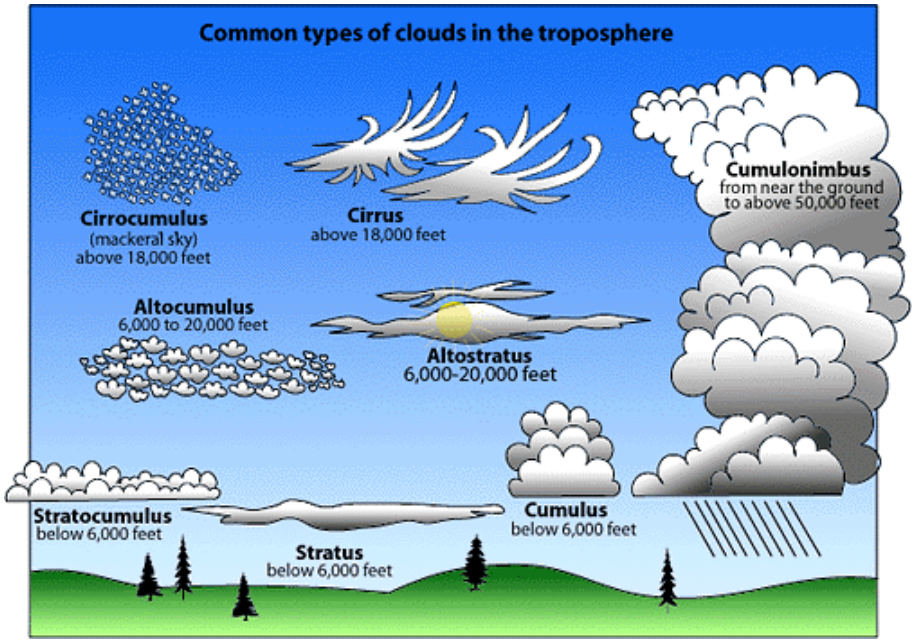

Fig. 1.3 Cloud types classification provided by NCAR. https://scied.ucar.edu/learning-zone/clouds/cloud-types

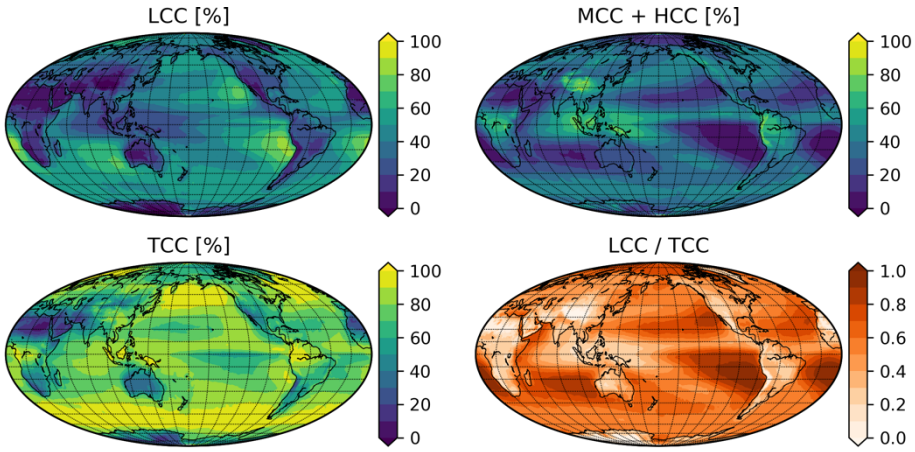

Fig. 1.4 Climatology of LCC (upper left), MCC+HCC (upper right), and TCC (lower left) based on MODIS observations from January 2003to December 2016. Lower right figure shows the ratio of climatological-mean LCC and TCC.

1.2 Unresolved problems

1.2.1 Causal relationship between low-level cloud and SST

Mean-state and variability of the low-level cloud properties are strongly modulated by atmospheric environments and sea surface conditions, which has been revealed as the "low-level cloud controlling factors" by numerous previous studies based on satellite datasets or numerical simulation (summarized in Klein et al., 2017). The physical linkage between the low-level cloud properties and the controlling factors are mainly utilized for the future prediction of cloud distribution along with the scenario associated with global warming (McCoy et al., 2017; Myers & Norris, 2016; Qu et al., 2014, 2015; Seethala et al., 2015). Predictions of environmental condition, such as large-scale atmospheric circulation, sea surface temperature, and thermodynamic state, have small ensemble errors in many General Circulation Models (GCMs). In contrast, the prediction of cloud has large uncertainty among these GCMs, as reported in the Intergovernmental Panel on Climate Change (IPCC) Fifth report.

In terms of the "feedback" to global warming, cloud feedback remains to be one of the largest uncertainties when compared with other feedback processes (i.e. water vapor feedback, lapse rate feedback, and so on) (Fig. 1.5; Zelinka & Hartmann, 2012). As a result, the representation of the cloud response to the global warming in GCMs is not represented well by and has large uncertainty, in particular the cloud process with aerosol indirect effect (Fig. 1.6). It is due to the problem related with the coarse resolution of GCMs which cannot resolve the small spatial scale associated with turbulence within the atmospheric boundary layer, cloud microphysical process, cloud-aerosol interaction, and so on. It is therefore imperative to understand not only the physical linkage between low-level cloud

properties and environmental conditions but also the feedback process between cloud and environmental conditions; i.e. cloud-radiation feedback, cloud-ocean feedback, and cloud-aerosol feedback. Thus, we need to further investigate the mechanism within these feedback processes to reduce the uncertainty of prediction in the models.

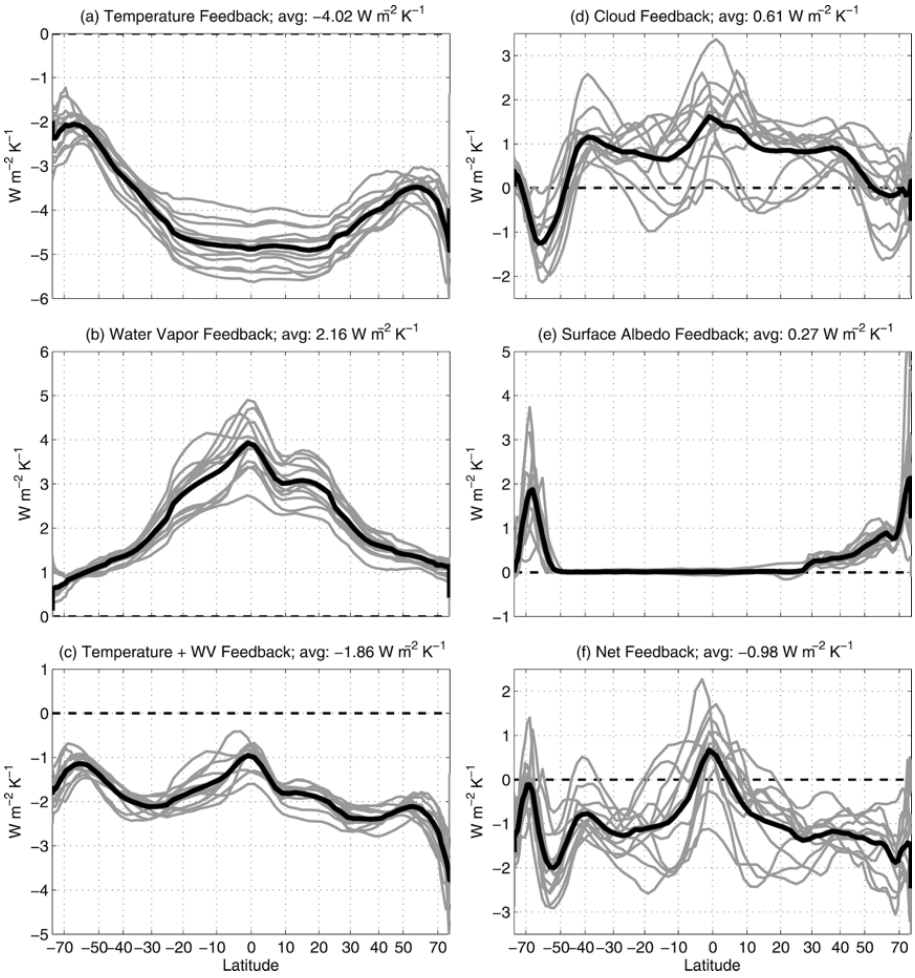

Fig.1.5 Zonal-mean (a) temperature, (b) water vapor, (c) combined temperature–water vapor, (d) cloud, and (e) surface albedo feedbacks, along with (f) the sum of all feedbacks. Each of the 12 models from CMIP3 is represented by an individual gray line, and the thick black line represents the multi-model mean. The abscissa is sine of latitude so that the visual integral is proportional to watts per kelvin of mean surface temperature change. Note that the vertical axis limits vary among panels, but all span a range of 6 W m^{-2} K^{-1}. Adopted from Zelinka and Hartmann (2012).

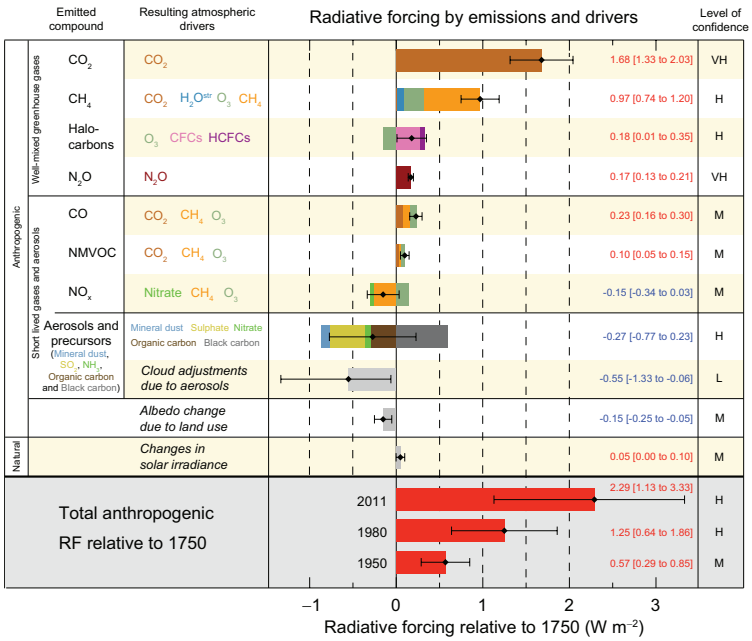

Fig.1.6 Radiative forcing estimates in 2011 relative to 1750 and aggregated uncertainties for the main drivers of climate change. Values are global average radiative forcing (RF14), partitioned according to the emitted compounds or processes that result in a combination of drivers. Total anthropogenic radiative forcing is provided for three different years relative to 1750. Adopted from IPCC AR5 reports (2014).

Sea surface temperature (SST) is traditionally known as one of key modulators of the low-level cloud properties (Bretherton et al., 2013; Norris & Leovy, 1994; Qu et al., 2015). As shown in a map of the climatological-mean LCC and its ratio to TCC (Fig. 1.4), low-level cloud tends to appear in the regions off the west coasts of North and South America, Australia, and Africa continents, where SST is relatively low due to the coastal upwelling. Lower SST is favorable for the formation of low-level cloud because of the suppressed convection and entrainment of dry-air from the free-troposphere (Bretherton et al., 2013). In turn, the low-level clouds can cool the local SST through their strong cooling effects, especially with thin mixed layer depth in summertime mid-latitude. It is, therefore, known as the negative correlation between LCC and SST. As a result, positive feedback between low-level cloud and SST exists in summertime mid-latitude ocean-basin. Norris and Leovy (1994) for the first time investigated the map of the correlation coefficient between LCC and SST on inter-annual timescale, showing that the highest correlation lies in the summertime SST frontal zone where the horizontal gradient of SST is the largest in the north Pacific (NP) (Fig. 1.7), due to the western boundary currents such as the Kuroshio Extension (KE) and the Oyashio Extension (OE).

Generally, it had been recognized that mid-latitude ocean plays a passive role by the atmospheric variability, especially in summertime. It is because mixed-layer depth in summertime mid-latitude is so thin (about 20 m) that SST variation strongly depends on surface heat flux variability (Cronin et al., 2013). Although the general recognition of the passive role of ocean, recent studies have revealed the active role of ocean particularly around the western boundary current regions (i.e. Kuroshio Extension, Gulf stream) based on high-resolution satellite data analysis and coupled ocean-atmosphere models (e.g. Kwon et al. 2010). Most of the studies, however, focused on the wintertime because of the huge amount of the heat release from ocean to atmosphere induced by the warm western boundary currents in wintertime. In these frontal regions, oceanic dynamics associated with the western boundary currents are also important for local SST variations (Qiu, 2001; Qiu et al., 2017). Thus, there is a possibility for the active role of ocean associated with the western boundary currents while the general recognition is that atmospheric forcing is a dominant factor to control local SST variability in summertime. Some studies have investigated and pointed out the importance of the active role of SST, but almost all of studies are based on the in-situ observations and numerical simulations. Previous studies based on the satellite observation tend to analyze only the correlation between low-level cloud and SST, thus causal relationship in summertime is still unclear. Process-oriented understanding of the linkage between them and its observational evidence are needed. We expect to improve the air-sea interaction process in the coupled GCMs based on new knowledge of cloud-sea interaction, coming from detailed analysis for the feedback loop.

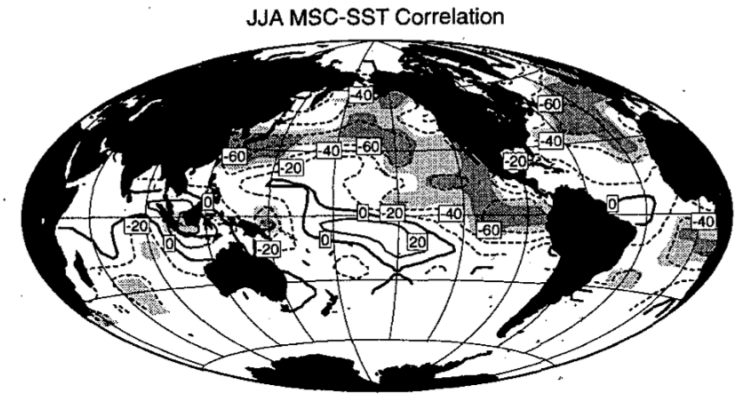

Fig1.7 Correlation map of SST and stratiform cloud amount in JJA. Adapted from Norris and Leovy. (1994), but modified version is displayed.

1.2.2 Timescale of cloud and SST variabilities

While the coupling of low-level cloud and SST has been observed, typical timescales of their variabilities are quite different. For instance, de Szoeke et al. (2016) focused on the marine boundary layer cloud in the subtropics and showed the spectrum of LCC, SST, and estimated inversion strength (EIS) (Fig. 1.8). EIS is estimated inversion strength calculated by potential temperature at 700 hPa and the surface (Wood & Bretherton, 2006), which represents the lower atmospheric stability taking into account for overestimation derived from lapse rate and is considered as another important controlling factor of LCC (Klein et al., 2017). As clearly seen in Fig 1.8, spectrum of LCC based on 6-hourly data, indicated by the blue line, has the strongest peak at diurnal cycle and secondary peaks at synoptic timescale (3-7 days). On the other hand, SST spectrum based on daily data, shown as the green line in Fig. 1.8, has the strongest peak at annual cycle, which is much longer than that in LCC. Difference in typical timescales of cloud and SST is derived from their own specific heat capacities. Considering this, degree of the coupling of cloud with SST and further the main driver of the possible feedback loop are also different with the timescales we focused on. Kubar et al. (2012) examined the correlation between low-level cloud fraction and SST in terms of timescale dependence (i.e. 2-day [Daily] to 90-day [Seasonal] running mean filter). Figure 1.9 shows that correlation coefficients dramatically increase with time from one-day to approximately 2 weeks, then nearly stay at high value when passing after that point. It implies that atmospheric variability is more dominant to control the low-level cloud properties than SST variability on the synoptic timescale shorter than two weeks (i.e. synoptic atmospheric disturbances).

We have an awareness of the timescale dependence of the feedback loop between low-level cloud and SST, similar with the previous studies described above (Kubar et al., 2012; de Szoeke et al., 2016). We hypothesize that the main driver of the feedback depends on the timescale: Cloud for shorter timescale and SST for longer timescale. In other word, we are expecting that ocean plays a more important role with the extension of the timescale length, from inter-annual variations, to decadal variations, and global warming, despite in summertime. Besides, we would also pay attention to the interaction processes across different timescales. In addition, inter-mediate timescales between the typical timescales of cloud and SST are also interesting phenomena, i.e. intra-seasonal timescale. As shown in Chapter2 later, coherence between LCC and SST reaches maximum on the intra-seasonal scale, implying the tight linkage between them with two-way physical processes (Wang et al., 2012). Thus, we need to understand the role of ocean for the low-level cloud variability on various timescales (i.e. synoptic, intra-seasonal, inter-annual) and that across the timescales.

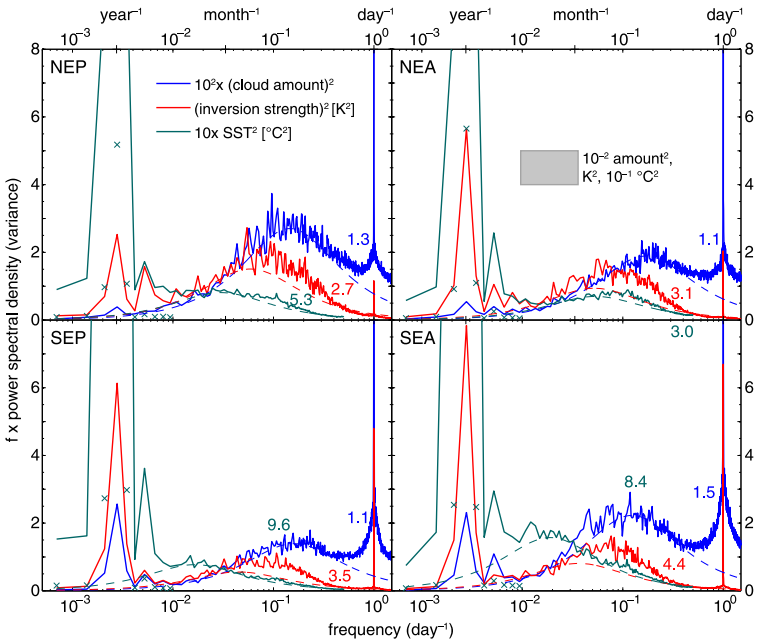

Fig1.8 Variance-preserving spectra of low cloud amount and inversion strength in the four eastern tropical or subtropical Pacific and Atlantic stratocumulus regions: North-East Pacific (NEP), North-East Atlantic (NEA), South-East Pacific (SEP), and South-East Atlantic (SEA). Dashed lines are red noise fits to the portion of the respective spectra between the annual and daily peaks. The damping time scale (days) is printed beside the curves. Adopted from de Szoke et al. (2016).

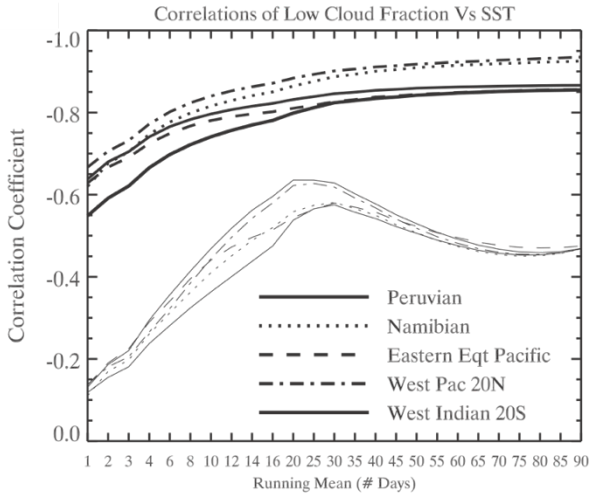

Fig1.9 Dependence of correlation coefficient on timescale used in the running mean procedure for time series of SST and low-level cloud fraction (LCF). The dependences of correlation coefficient were calculated in five selected regions (Peruvian, Namibian, Eastern Equatorial Pacific, West Pacific around 20˚N, and West Indian around 20˚N). Adapted from Kubar et al. (2012), but modified version is displayed.

1.3 Objective of this study

Main problem about the relationship is “a dependence on timescale for a key trigger of the positive feedback loop, in particular, the impact of SST on low-level cloud properties”. Thus, we investigated causal relationship between the low-level cloud properties and SST on various timescales based on the observational data analysis and numerical experiments using atmospheric regional model. In each chapter, we focused on

- two-way physical processes between LCC and SST on “intra-seasonal” timescale in summertime western NP
- active role of SST anomaly associated with SST frontal characteristics in modulating the low-level cloud properties on “synoptic” timescale by numerical experiments
- observational evidence of the active SST role in summertime on “inter-annual” timescale and regionality of passive/active SST role in the interaction process with low-level cloud

In the rest of this section, we will briefly introduce the scientific questions in each chapter. The detailed objectives are described in the “Introduction” part of each chapter.

Chapter 2 describes the phase relationship between low-level properties and SST in order to reveal the relative roles of atmosphere and ocean in the two-way physical processes on intra-seasonal timescale. Key scientific question is “Which is a primarily trigger of the feedback loop on intra-seasonal timescale; low-level cloud or SST in summertime?”. To answer this question, we conducted satellite-based analysis and revealed the detailed physical mechanism of evolutions of low-level cloud properties and SST.

Chapter 3 focuses on the mechanism of the impact of SST anomaly associated with the SST front on low-level cloud properties in summertime NP, based on the WRF numerical simulation. The timescales focused on in this chapter is the synoptic timescale. Key scientific question is “Does the SST front play an active role in modulating the synoptic variability of the low-level cloud properties in summertime? If so, what is the mechanism?”. We ran two numerical experiments forced by different SST conditions, the obtained results suggest two physical modulation processes of the low-level cloud by the SST changes. One is consistent with traditional process, and the other is a new process associated with the temperature advection across the SST front modulated by its frontal characteristic.

In Chapter 4 we investigated again the active role of SST in modulating the low-level cloud properties, but based on satellite data analysis. Key scientific question is “Can we obtain the observational evidence of the active role of SST? How much variation of the low-level cloud properties on inter-annual timescale can be attributed to the SST effect in the real world?”. It is similar to Chapter 3, however, we tried to investigate the variabilities of not only SST but also oceanic subsurface temperature based on Argo float observation. In addition, we quantified the SST contribution

compared with other controlling factors for low-level cloud properties by constructing the multi-linear regression model.

Finally, we gave a general conclusion about the two-way physical processes between low-level cloud and sea surface temperature, and ocean's role in the feedback loop from the overall results in this thesis. Future prospects are also given in Chapter 5.

Chapter 2

Intra-Seasonal Variability of Low-Level Cloud and Sea Surface Temperature in Summertime North Pacific based on MODIS Satellite Observation

2.1 Introduction

Oceanic low-level cloud in summertime North Pacific (NP) plays an important role in air-sea interaction processes because it has a strong cooling shortwave cloud radiative effect (SWCRE) at the sea surface and the low-level cloud properties are sensitive to sea surface state. The SWCRE of low-level cloud is derived from its high albedo and warm cloud top temperature (Hartmann and Short, 1980). Low-level cloud cover (LCC) is an important parameter to determine SWCRE at the sea surface. Despite the importance of LCC and SWCRE, the projection quality of these parameters associated with climate variability in general circulation models (GCMs) is a major source of uncertainty in future climate projections (Bony & Dufrense, 2005; Brient & Bony, 2013; Myers & Norris, 2016; Qu et al., 2014, 2015).

One of the reasons for the large uncertainty in GCMs is a difficulty in representing of low-level cloud with turbulence within the boundary layer, cloud-radiative interaction, and cloud microphysical process in a coarse grid resolution. Additionally the evolution process of LCC is so complex and can be modulated by many environmental factors, which is called as LCC controlling factors, that is, estimated inversion strength (EIS), horizontal temperature advection (T_{adv}), sea surface temperature (SST), and so on (see Klein et al. 2017 for a summary). In previous studies, the accuracy of a projection of the sensitivity of LCC and SWCRE to controlling factors in GCMs was investigated and compared with observational results using a multi-linear regression method to estimate the inter-annual variability of the monthly mean state (Myers & Norris, 2016; Qu et al., 2014, 2015). Previous studies also showed that the relative contributions of the LCC response to each controlling factor, for example, EIS is the dominant LCC controlling factors on an inter-annual timescale.

On a longer timescale (e.g. inter-annual timescale), SST is recognized as a one of LCC controlling

factor and driver of local LCC variability through a stratification of boundary and suppression of entrainment process of dry-air from free troposphere (Bretherton et al., 2013). However, on short timescales (e.g. diurnal cycles and synoptic disturbance), the causal relationship between low-level cloud and SST might change. Low-level cloud variability on synoptic timescale tends to be modulated by atmospheric variability rather than SST variability because typical timescale of SST is much longer than that of low-level cloud properties. The short timescales are much more suitable when evaluating the evolution process of low-level cloud. Xu et al. (2005) investigated the sub-seasonal variability of cloud liquid water in the southeastern Pacific using satellite, buoy observation, and reanalysis datasets, and conducted a lead-lag composite analysis of low-level cloud properties and LCC controlling factors. They concluded that the low-level cloud variability is caused by changes in atmospheric circulation rather than by the underlying oceanic state and revealed an important role of cold advection in modulating low-level cloud variability. Other studies also reported the importance of horizontal T_{adv} near the sea surface for controlling LCC variation using both satellite and ship-based observations (Klein, 1997; Mauger & Norris, 2010; Miyamoto et al., 2018; Norris & Iacobellis, 2005; Xu et al., 2005; Zelinka et al., 2018). Norris and Iacobellis (2005) investigated the horizontal distribution of the amount of each cloud type associated with the synoptic variability of T_{adv} in the NP. Their results showed that warm advection in summertime NP enhances optically thick and high-level cloud, fog, and stratus, as observed by satellite and ship-based observation; in contrast, the cold advection produces favorable conditions for low-level cloud, in particular stratocumulus and cumulus. The mechanism of LCC enhancement with cold advection over a warm sea surface is related with the processes which destabilizes lower atmosphere near the sea surface and enhances turbulent heat flux from ocean to atmosphere, meaning that advected cold air above the warm sea surface leads to unstable conditions in the marine boundary layer, and this destabilization can create stratocumulus or cumulus (Wood, 2012). Therefore, horizontal cold advection is known to be a key parameter which enhances turbulent heat flux and the formation of low-level cloud in the subtropical and mid-latitude ocean, especially in summertime. However, uncertainty remains regarding the causal relationship among low-level cloud, horizontal temperature advection, and SST on intermediate timescales (i.e. intra-seasonal timescales).

Intra-seasonal timescale is intermediate timescale between the dominant timescales of cloud (e.g. synoptic timescale) and SST (e.g. seasonal to annual timescale). Thus, it is important to reveal relative contribution of atmospheric variability or oceanic process for trigger of feedback loop between LCC and SST. The intra-seasonal variability (ISV) of atmospheric circulation is a prominent phenomenon, especially in summertime NP. Many previous studies observed the oscillation or variability of atmospheric circulation or precipitation on an intra-seasonal scale and investigated the detailed mechanism of such a variability in summertime NP (Yasunari, 1979; Kawamura et al., 1996; Wang et al., 2012; Wang et al., 2013). Cloud cover also varies with the ISV of atmospheric circulation related to remote forcing from the tropics and internal dynamics in the mid-latitudes. Wang et al. (2012)

investigated the ISV of the SST anomaly (SSTA) in the Kuroshio Extension region on an intra-seasonal timescale as well as air–sea interaction using reanalysis and satellite observational datasets. They showed that the ISV of the large-scale atmospheric circulation anomaly induces an SSTA due to changes in the surface heat flux. On the other hand, the SSTA also induces the atmospheric circulation anomaly, therefore implying the two-way interactions, which in turn shows the importance of local air–sea interaction for the ISV of the SSTA. Wang et al. (2013) revealed the cause of the ISV of a large-scale atmospheric circulation anomaly in summertime NP from a different perspective, and showed that the Rossby wave propagation generated in western North America is important to the variability of the change in the circulation in summertime NP. Therefore, there is a possibility that the SSTA plays an active role not only in atmospheric circulation but also in the evolution of low-level cloud on an intra-seasonal timescale, similar to what occurs on an inter-annual timescale.

Here, we examined the air–sea interaction process, especially LCC versus SST, on an intra-seasonal timescale, considering the timescale of LCC evolution. Additionally, lead-lag composite analysis was conducted based on the local LCC anomaly (LCCA) in order to investigate not only the causal relationship between LCC and LCC controlling factors, but also the evolution process of LCC with changing humidity field. Important questions addressed by the present chapter are, *"Which is a primarily trigger of the feedback loop on intra-seasonal timescale; low-level cloud or SST in summertime?"* and *"Which is the dominant controlling factor for the ISV of LCC, atmospheric circulation or local SST?"*.

The remainder of this chapter is organized as follows. In Section 2.2, the observational dataset used in the present chapter is described. This section also explains the filtering method used to extract the ISV of LCC and the phase composite analysis method used to describe the evolution process of LCC and other LCC controlling factors. Section 2.3 gives the results of the observed LCC evolution and air–sea interaction associated with the ISV of LCC. Section 2.3 is divided into four subsections: (1) dominant timescale of LCC variability in summertime western NP based on spectral analysis; (2) ISV of LCC and cloud controlling factors; (3) the mechanism of LCC evolution and humidity field; and (4) two-way interaction process associated with the ISV of LCC, especially for atmospheric forcing into oceanic subsurface variability. The active role of the ocean in the properties of low-level cloud is discussed in Section 2.4. A summary and the rest of the discussion are also presented in Section 2.4.

2.2 Data and methods

2.2.1. Data

The L3 gridded cloud product (MYD08_D3) from the latest Moderate Resolution Imaging Spectroradiometer (MODIS) release (version 6) from MODIS instruments on board the Aqua satellite

platform (Platnick et al, 2015) was used to estimate LCC. The daily-mean MODIS dataset is produced by twice-daily observation at 01:30 and 13:30 local time. The daily cloud cover of each type in a 1°×1° grid is calculated using the histogram of cloud top pressure and the number of observational grid points in the grid. Estimation of the LCC using passive sensors is difficult due to the problem of cloud overlapping, that is, the obscuring of mid- and high-level clouds. Therefore, to avoid the overlapping problem, the actual LCC was calculated assuming random overlap as LCC = $f_L/(1-f_M-f_H)$, where f_L, f_M, and f_H are the fraction of the scene covered by each cloud type whose top is low (680 hPa≤ cloud top pressure [CTP] <1000 hPa), middle (440 hPa≤ CTP <680 hPa), and high altitude (CTP <440 hPa), respectively. Validity of the random overlap assumption applied to daily-mean dataset of low-level cloud coverage from passive sensor is still needed for further discussion because daily mean LCC estimated with this assumption strongly depends on f_M, and f_H, as noted in Appendix 2A. The missing LCC values for a certain grid point for daily data were linearly interpolated using the LCC values one day before and after the day of interest. The period from 2003 to 2016 was analyzed because all of the datasets described below were available for this time period.

The National Oceanic and Atmospheric Administration (NOAA) optimum interpolation (OI) objectively analyzed SST version 2 (OISST; Reynolds et al., 2002) was used to analyze the variability of SST. The spatial and temporal resolution of OISST are 0.25° and daily, respectively. To investigate the meteorological field associated with the ISV of LCC and SST, we used ERA-Interim reanalysis data (Dee et al., 2011) with a horizontal resolution of 0.75° and 37 vertical levels. Using the 6-hourly ERA-Interim dataset, we obtained daily mean data for each variable. There are many other atmospheric reanalysis datasets (e.g. MERRA2 [Gelaro et al. 2017]; JRA-55 [Kobayashi et al. 2015]), but I choose the ERA-Interim dataset for investigating humidity field in the atmospheric boundary layer because bias of low-level cloud cover in summertime North Pacific is the smallest compared with the other reanalysis datasets while we focused on the monthly-mean state (not shown). Daily data of temperature at 700 hPa and 1000 hPa, horizontal wind speed at 1000 hPa, and sea level pressure were used to calculate the EIS and horizontal temperature advection, which was used as a proxy for LCC controlling factors. EIS was calculated following the method of Wood and Bretherton (2006). Additionally, T_{adv} was calculated as the product of the horizontal gradient of SST obtained from OISST and the horizontal wind speed at 1000 hPa obtained from ERA-Interim.

For the heat flux datasets (shortwave radiation [SW], longwave radiation [LW], sensible heat, and latent heat) at the sea surface, two observational datasets were used in this chapter. To estimate daily-mean radiative fluxes (SW and LW), we used the Clouds and the Earths Radiant Energy System (CERES) Synoptic Radiative Fluxes and Clouds (SYN) product Edition 4.0 (Ed4A) (Wielicki et al. 1996). The variables were calculated by a radiative transfer model initialized using satellite-based cloud and aerosol and meteorological assimilation data from reanalysis. The variables were also

constrained by observed top-of-atmosphere radiative fluxes. The Objectively Analyzed air-sea Heat Fluxes (OAFlux) project at the Woods Hole Oceanographic Institution (WHOI) provided the global ocean-surface heat flux products from 1955 to present (Yu et al., 2008). We used the daily mean turbulent fluxes dataset. OAFlux products are constructed not from a single data source, but from an optimal blending of satellite retrievals and three atmospheric reanalysis datasets. The horizontal resolution of CERES and OAFlux product is 1° in longitude and latitude.

2.2.2. Methods

In order to extract the intra-seasonal (20–100 days) signal from the original time-series of each variable, we applied a Lanczos bandpass filter to the time-series of all variables from 2003 to 2016. Before the filtering process, we removed the seasonal cycle signal from the original time-series, which is the climatological mean value on each calendar day.

We applied a composite phase analysis method to the filtered LCCA in order to investigate how the LCCA and the controlling factors of LCC evolve within one cycle in the ISV of LCC. A based index which was used in the composite analysis was calculated as the area-mean LCCA in the target region (165−175˚E and 30–40˚N), where the standard deviation of the LCC is the largest in the NP. The other way to describe the evolution of LCCA is the lagged-day composite analysis method. However, this method is not suitable when the filtering time-range is broad (20−100 days), and a large error could occur for far days from a lag of 0. Then, we applied a composite phase analysis technique to the LCCA index in a similar way to SSTA in Wang et al. (2012). In the composite phase analysis method, each cycle of the ISV of LCC is divided into 12 phases with an interval of 30˚ (i.e., -180˚, -150˚, -120˚, …, 150˚, 180˚). A phase of 0˚ corresponds to the time when the LCCA reaches a maximum value, and phases of −180˚ and 180˚ correspond to the time when the LCCA reaches a minimum value. The phase ranges from −180˚ to 0˚ (from 0˚ to 180˚) can be defined as the “development” (“dissipation”) stage of the LCCA in the target region. To find the days with other phases, linear interpolation was conducted using the days with phases of −180˚, 0˚, and 180˚. The composite cases include only days when the maximum and minimum LCCA exceed one standard deviation.

The target region was chosen because the variability of both LCC and SST on an intra-seasonal timescale is exceptionally large in summertime NP. Figure 2.1a and b show the horizontal distributions of mean climatological conditions and the standard deviations of LCC and SST in summer NP (July) from 2003 to 2016. The standard deviation of the unfiltered daily LCC is large in the meridional band from 30–40˚N and 150˚E–150˚W (shown by the black rectangle in Fig. 2.1b); in contrast, the standard deviation in the meridional band from 40–50˚N and 150˚E–150˚W is relatively small. This difference in standard deviation is likely to correspond to the distribution of the climatological mean LCC shown in Fig. 2.1a, meaning that the standard deviation of the mean LCC

in summertime is large. Figure 2.1c shows the mean seasonal variation of the sub-seasonal standard deviation of LCC (shaded) and SST (contours) in the southern flank of the SST frontal zone where meridional gradient of SST is strong around 40˚N. The sub-seasonal standard deviation of each variable was calculated as the standard deviation for the period between 45 days before and 45 days after the day of interest. The degree of variability was found to have clear seasonality, with the variability being largest in summertime (Fig. 2.1c). In the present chapter, we define summertime as June–October (JJASO), the time when the LCC variability is largest in the mid-latitude NP. Additionally, the standard deviation of SST is also large in the southern flank of the front and in summertime NP, although its peak of is located just over the SST front (Fig. 2.1b and c). It is because the local interaction between low-level cloud and SST is strong in summertime NP compared with wintertime. For the following analysis, we selected a target region where the variabilities of LCC and SST in summertime are especially large (30–40˚N and 165–175˚E; shown by the black rectangle in Fig. 2.1c). Domain size of 10˚ is determined by the typical spatial scale of ISV of LCC from hovmöller diagram result (not shown), and results shown in later do not strongly depend on the domain size.

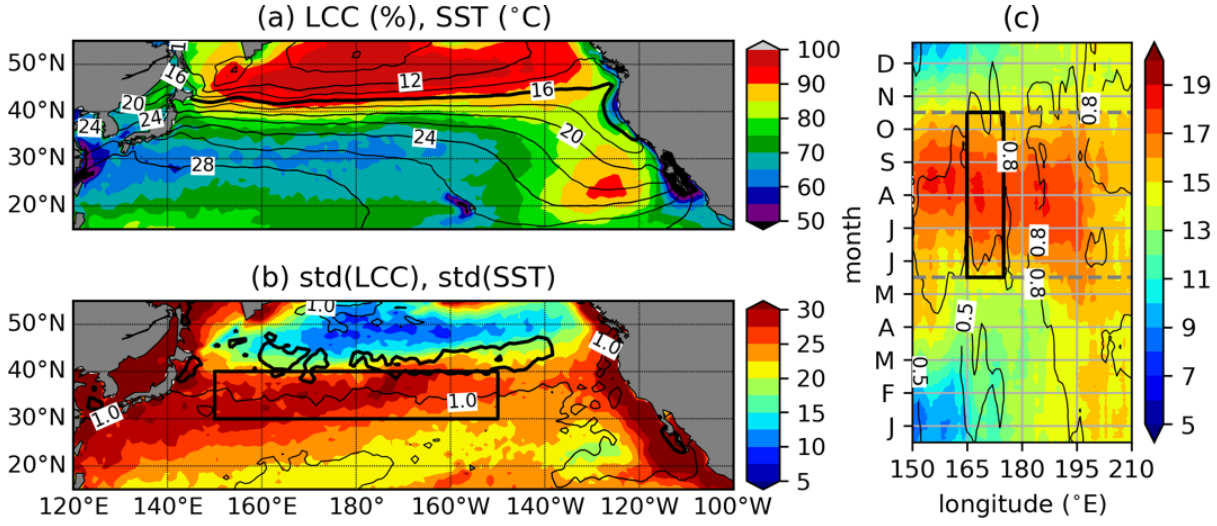

Fig. 2.1. **(a)** Climatology of low-level cloud cover (LCC) derived from the Moderate Resolution Imaging Spectroradiometer (MODIS; shaded; %) and sea surface temperature (SST) derived from OISST (contours; ˚C, Contour Interval (CI) = 2˚C, Thick Contour (TC) = 16˚C) in the North Pacific in July from 2003 to 2016. **(b)** Standard deviation of de-seasonal daily LCC data (shaded; %) and SST (contours; ˚C, CI=0.5˚C, TC=1.5˚C). The black rectangle shows the region where the standard deviation of LCC is large and the target meridional band from 30–40˚N used in the present chapter. **(c)** Mean seasonal variation of the sub-seasonal standard deviation of LCC (shaded; %) and SST (contours; ˚C, CI=0.3˚C) for the target meridional band. The standard deviation for each variable on day *i* is calculated as the standard deviation of LCC and SST from day *[i–45]* to day *[i+45]* using a method similar to that of Wang et al. (2012). The two gray horizontal dashed lines show the season analyzed in the present chapter (JJASO). The black rectangle shows a target longitudinal band from 165–175˚E where the standard deviation of LCC and SST are both large.

To evaluate the SST variability associated with the ISV of low-level cloud, an analysis of the mixed-layer temperature budget was conducted. The mixed-layer temperature budget equation (Moisan & Niiler, 1998) is as follows:

$$\frac{\partial SST'}{\partial t} = \frac{\left(Q_{total} - Q_{pen}\right)'}{\rho C_p H} + R\,, \tag{2.1}$$

where Q_{total} and Q_{pen} represent the sum of the net downward heat fluxes at the ocean surface, and the sum of the penetrated shortwave radiative flux at the bottom of the mixed layer (Paulson and Simpson, 1977), respectively; H is a constant mixed-layer depth (= 25 m); ρ is the density of water; and C_p is the specific heat of water. The constant H was estimated as the climatological mean mixed-layer depth in summertime (JJASO) in the target region as obtained from MIMOC (Johnson et al., 2012). R is a residual term including an oceanic term (i.e., horizontal and vertical advection, entrainment processes, and vertical ocean mixing) and observational error. A prime denotes the filtered variables (20–100 days).

Relative humidity (RH) is an important factor for determining cloud evolution. To investigate the detailed mechanism of LCC evolution, we analyzed the temporal variation of RH and its tendency. RH is calculated by $RH=e/e_s$, where e is the water vapor pressure and e_s is the saturated water vapor pressure. These two variables are determined using temperature (T) and specific humidity (q). Therefore, the tendency of RH is separated into tendencies of T change and q change (Ek and Mahrt, 1994; Babić et al., 2018) as

$$\frac{\partial RH}{\partial t} = \frac{p}{e_s}\frac{0.622}{(0.378q + 0.622)^2}\frac{\partial q}{\partial t} - \frac{qL_v}{(0.378q + 0.622)R_d T^2}\frac{\partial T}{\partial t}\,, \tag{2.2}$$

where p is pressure, L_v is the latent heat of evaporation, and R_d is the constant of dry air. We conducted a quantitative investigation of RH tendency. The formation and dissipation processes of low-level cloud associated with RH change are discussed in Section 2.3.3

2.3 Results

2.3.1. Dominant timescale of LCC variability in summertime NP

We investigated variabilities of the dominant timescales of LCC, SST, and T_{adv} in the target region and conducted Fast Fourier Transfer (FFT) analysis of LCC variability. Figure 2.2a shows the 14-year mean summertime spectrum of the area-mean LCC in the target region. The results indicate that there are two dominant timescales in the variability of LCC: (1) 2–3 days; and (2) 10–50 days. Because the sampling period is once a day, the first timescale is almost equal to the Nyquist frequency, and is likely to correspond to synoptic disturbances. The spectral signal is significantly weaker for the second timescale than for the first timescale. The second spectral signal is likely to be associated with the ISV

of LCC, atmospheric circulation, and SST in summertime NP, which is consistent with the findings of Wang et al. (2012). The squared coherency between the area-mean LCC and area-mean SST in the target region is shown in Fig. 2.2b. No significant coherency peak was observed on the synoptic timescale (2–3 days). However, a significant coherency peak was observed on the intra-seasonal timescale (20–40 days), with a maximum at 30 days. The squared coherency between LCC and T_{adv} has similar characteristics on the intra-seasonal timescale; therefore, we conducted further analysis focusing on the ISV of LCC using a bandpass filter and a phase composite analysis technique as described in Section 2.2. We define the intra-seasonal timescale as 20–100 days, following Wang et al. (2012).

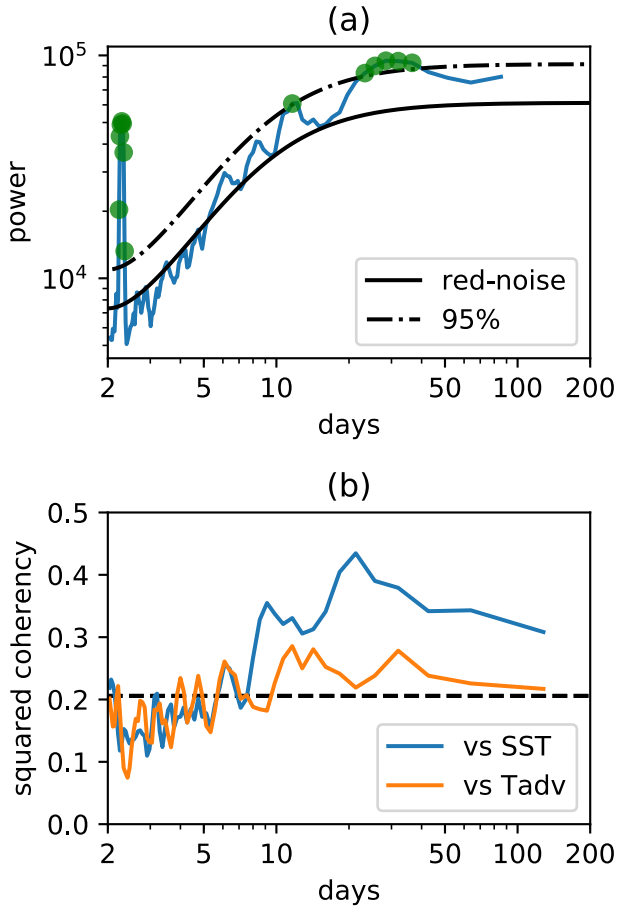

Fig. 2.2. **(a)** Mean power spectrum of the area-mean daily LCC in the target region (165–175°E, 30–40°N). The mean power spectrum was calculated as the mean value of all spectra for each JJASO season from 2003 to 2016. Solid and dashed lines indicate red-noise and the 95% significance level, respectively. Green dots indicate when the power exceeds the 95% significance level line. **(b)** Mean squared coherency between LCC and SST (blue) and between LCC and surface horizontal temperature advection (T_{adv}; orange). The horizontal dashed line indicates the 95% significance level determined by chi-squared distribution.

2.3.2. Characteristics of the ISV of LCC in summertime NP

Next, we investigated the characteristics of LCC evolution in the target region on an intra-seasonal timescale using phase composite analysis method. From the phase composite analysis of the 14-year JJASO LCC time-series, we obtained 46 cycles of LCC ISV in the target region. Figure 2.3 shows the statistical information of the ISV of LCC, indicating the one-cycle period and amplitude (Fig. 2.4a and b, respectively). The amplitude was calculated as the difference between the maximum and minimum values of LCCA divided by 2. The mean cycle period and the mean amplitude were found to be 29.5 days and 11.3%, respectively. No cycle was observed with a period longer than 50 days, implying that, if such a cycle exists, its amplitude is small. The mean cycle period is similar to the largest period determined by the FFT analysis on an intra-seasonal timescale (Fig. 2.2a), and the mean amplitude is about half of the standard deviation of LCC during JJASO (Fig. 2.1c).

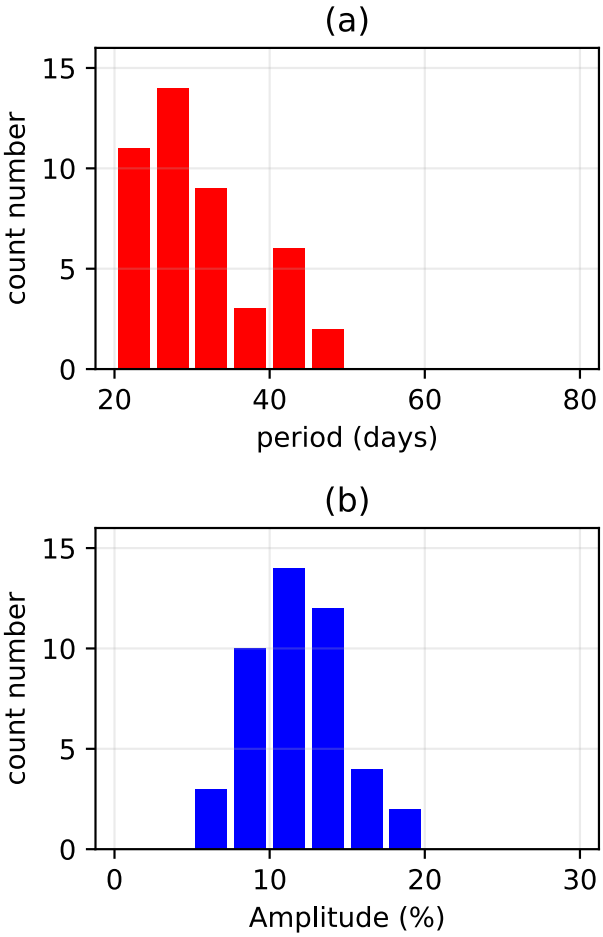

Fig. 2.3. Histograms of **(a)** cycle period and **(b)** amplitude, for each cycle of the intra-seasonal variability of LCC in the target region. The total number of cases is 46 for JJASO from 2003 to 2016. The bin sizes of each histogram are (a) 4 days and (b) 2%.

Figure 2.4 shows the composite mean horizontal distribution of the 20–100 days filtered

LCCA and the anomalous horizontal wind field at 1000 hPa at each phase. Note that, because the mean cycle period is 29.5 days (Fig. 2.2a), the length of time between each phase interval of 30˚ is about 2–3 days. The nature of the phase composite method means that the maximum (minimum) LCCA appears at a phase of 0˚ (phases of −180˚ and 180˚) in the target region (shown by black rectangles in Fig. 2.4). The sign of the LCCA index changes at around a phase of −90˚ (negative to positive) and 90˚ (positive to negative). When the LCCA is minimum (at phases of −180˚ and 180˚), anomalous lower-atmospheric circulation patterns are anti-cyclonic; these patterns weaken and disappear gradually as the phase increases from −180˚, and circulation becomes cyclonic when the LCCA reaches its maximum value (phase of 0˚). Similarly, as the phase decreases again, the cyclonic circulation patterns gradually disappear, and anti-cyclonic patterns appear at a phase of −180˚. Another characteristic feature of atmospheric circulation in the target region is that anomalous equatorward advection occurs during the development stage of the LCCA from phases of −90˚ to 0˚. Anomalous T_{adv} is likely to be an important controlling factor of LCC (e.g. Klein 1997). The evolution of other controlling factors of LCC in the cycle of ISV of LCC, namely EIS and SST, were also investigated using the same phase composite analysis technique (Fig. 2.5). As many studies have reported a strong relationship between LCC, SST, and EIS (e.g., Norris and Leovy 1994; Wood and Bretherton 2006), we also found that SST and EIS anomalies are positive and negative in the target region, respectively, when the LCCA reaches a maximum at a phase of 0˚, and vice versa (Fig. 2.5).

In order to qualitatively analyze the detailed lead-lag relationship between LCC and LCC controlling factors, the evolution of the area-mean anomalies of LCC, SST, EIS, and T_{adv} were calculated as shown in Fig. 2.6. Two prominent features of the lead-lag relationships were found. First, the minimum T_{adv} anomaly (i.e., cold advection) appears at a phase of −30˚, before LCCA reaches a maximum at a phase of 0˚. The phase lags of the minima/maxima of the LCC and T_{adv} anomalies imply that anomalous T_{adv} is a "trigger" of the LCCA variation within the cycle. Anomalous cold T_{adv} impacts LCC variation by modulating the characteristics of the atmospheric boundary layer, that is, a destabilization process or sensible heat flux (e.g. Wood 2012). Thus, we tested the detailed mechanism of LCC evolution associated with T_{adv} in terms of changes to the humidity field, as detailed in the next section. The second prominent feature of the lead-lag relationships is that the minimum SSTA and the maximum EIS anomaly occur at phases of 30˚ and 60˚, respectively, after LCCA reaches its maximum at a phase of 0˚. Considering the physical connections between LCC and SST, this implies that the SST and EIS anomalies are likely to be "followers" of LCCA variation within the cycle, through the interaction between LCC and SST associated with the cloud radiative effect. While, it is doubtful that EIS anomaly is follower of LCCA because lead-lag relationship of EIS and LCC are different in the cases with and without random overlap assumption (Appendix 2A). In the present chapter, the radiative impact of low-level cloud on the SST anomaly was investigated by applying the mixed-layer temperature budget equation (Eq. 2.1). The lead-lag relationships between LCC, T_{adv}, and SST

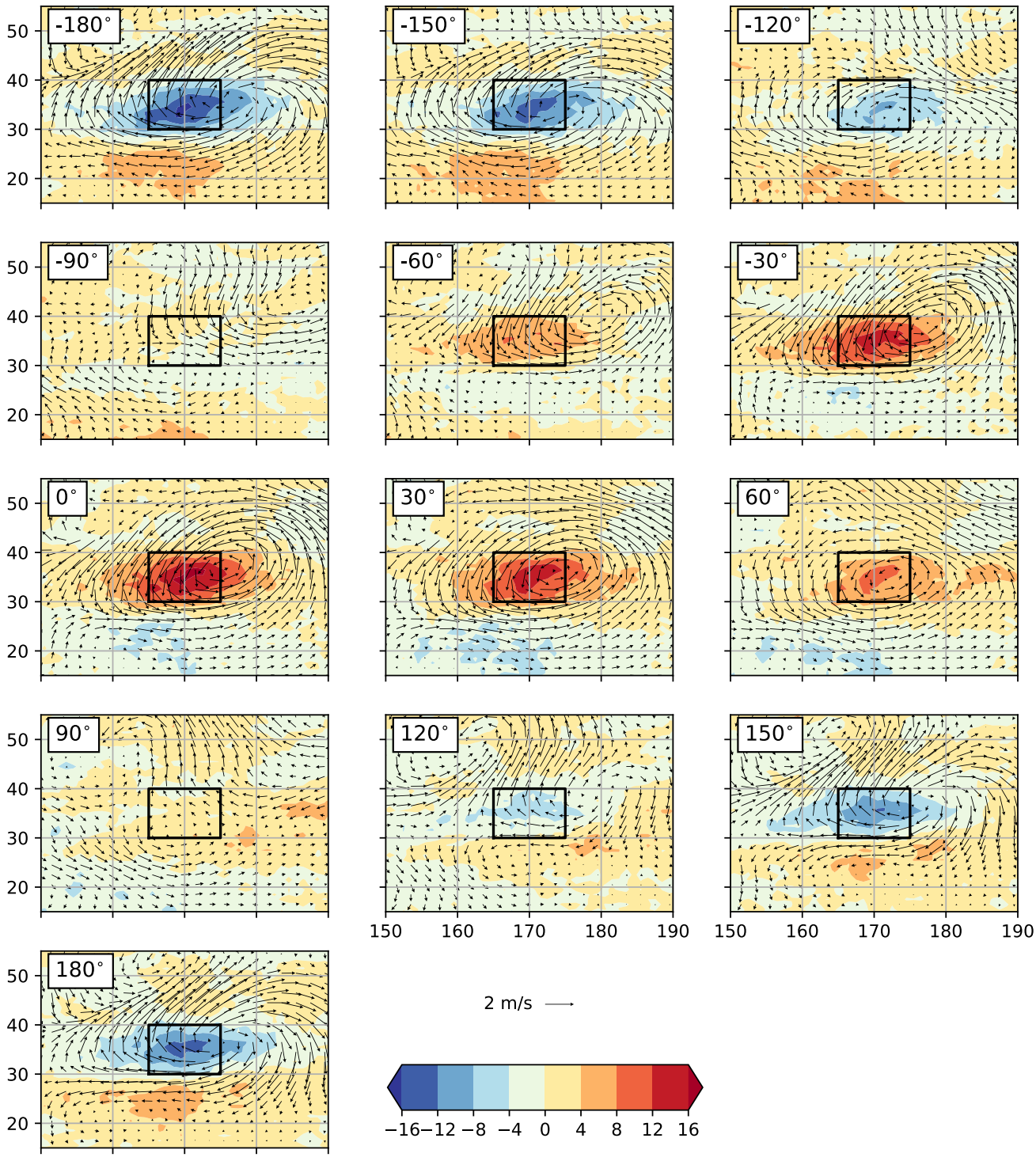

Fig. 2.4. Phase composite of the horizontal distribution of the LCC anomaly (shaded; %) and horizontal wind speed at 1000 hPa (vectors; m/s). The black rectangle denotes the area for which the LCC anomaly index was calculated. The maximum LCC anomaly appears at a phase of 0˚, while the minimum LCC anomaly occurs at phases of –180˚ and 180˚.

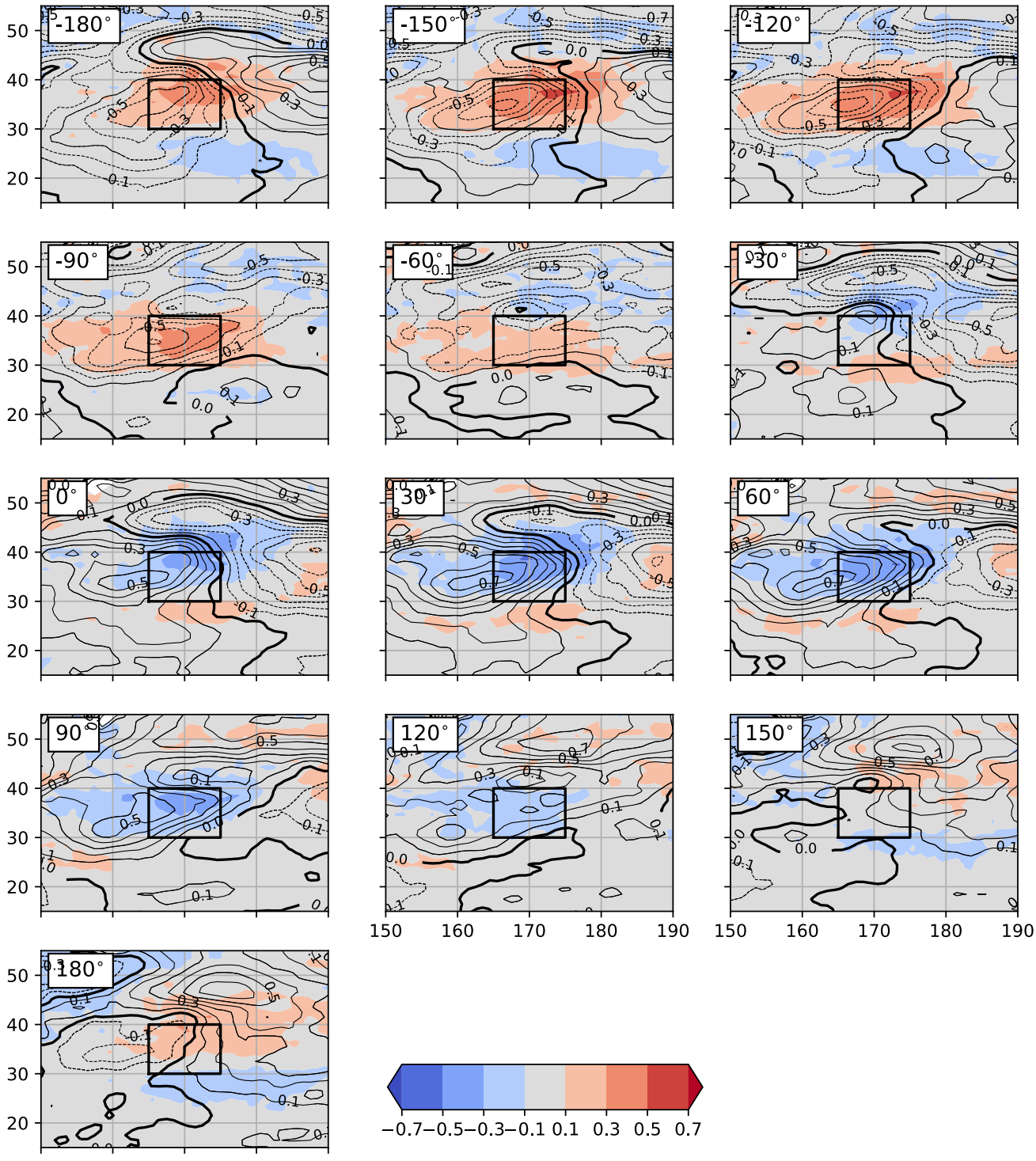

Fig. 2.5. As in Figure 2.4, but for SST (shaded; ˚C) and EIS (contour; CI=0.1 K, TC=0 K).

are consistent with the findings of Xu et al. (2005), who investigated the sub-seasonal variability of the southeast Pacific stratus cloud deck based on satellite, buoy, and reanalysis datasets. While SST and EIS are identified as "followers" of LCC inspired from Fig. 2.6, they have potentials to modulate LCC through processes of suppressed entrainment of dry-air from free troposphere (Bretherton et al., 2013). Thus, there is a possibility of the existences of the positive feedback process and the fast modulation process of negative SST and positive EIS for positive LCC anomaly around phase 0 (Fig. 2.6). However, robust conclusion about the relationship among T_{adv}, LCC, and SST is "T_{adv} is a trigger of LCC and SST" on intra-seasonal timescale in mid-latitude western NP.

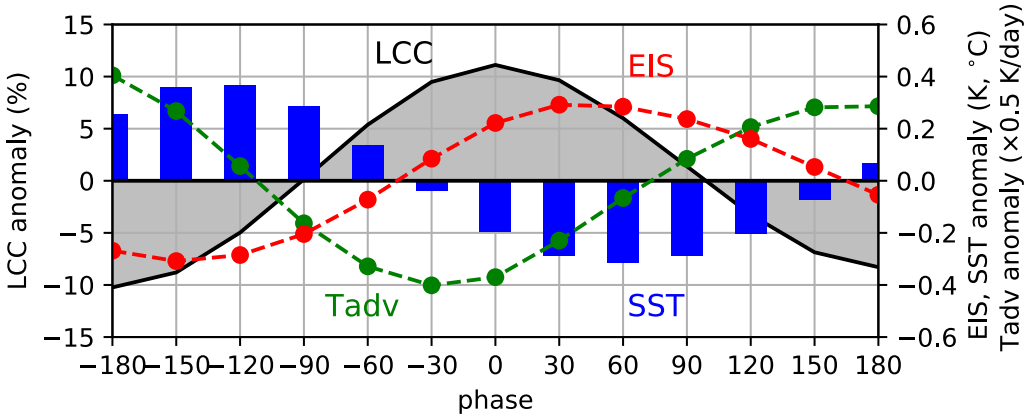

Fig. 2.6. Evolution of composite anomalies of LCC (black), SST (blue), T_{adv} (green), and EIS (red), averaged over the target area.

In order to determine the phenomena which cause anomalous changes in atmospheric circulation on an intra-seasonal timescale, we investigated the evolution of large-scale atmospheric circulation at the surface, mid-level (500 hPa), and upper altitude (250 hPa) to investigate the origin of the ISV of T_{adv}. Figure 2.7 shows the horizontal distribution of geopotential height (GPH) anomalies at 500 hPa (shaded) and 250 hPa (contours) and the corresponding horizontal wind field at 500 hPa (vectors). A similar feature with lower-atmospheric circulation anomalies is visible in Fig. 2.4, including cyclonic (anti-cyclonic) circulation patterns with a negative GPH anomaly which appears at a phase of 0˚ (phases of −180˚ and 180˚) in both the mid- and upper troposphere. This suggests that changes in circulation patterns during the evolution of LCCA have a barotropic structure. GPH anomalies at 500 hPa and 250 hPa are not stationary, but rather propagate westward (see green stars in Fig. 2.7). This westward propagation is likely associated with Rossby-wave excitation around the Rocky Mountains, which is similar to the first mode of summertime GPH on an intra-seasonal timescale (Wang et al., 2013). This anomalous atmospheric circulation pattern is mainly driven by internal atmospheric dynamics in the mid-latitudes; however, the GPH anomaly at 250 hPa shows a weak wave-train pattern with a cyclonic circulation in the middle and two anti-cyclonic circulations at

the two sides from phases of −30˚ to 30˚. Previous studies have shown that atmospheric circulation patterns in the mid-latitudes of summertime NP are remotely forced by intra-seasonal atmospheric oscillation in the tropics (Kawamura et al., 1996; Pan and Li, 2008; Mori and Watanabe, 2008). Although determining the contributions of remote forcing in the tropics and internal dynamics in the mid-latitudes to the anomalous atmospheric circulation pattern in the NP is key to understanding the ISV of atmospheric circulation, this topic will not be investigated further here because it is outside the scope of the present study.

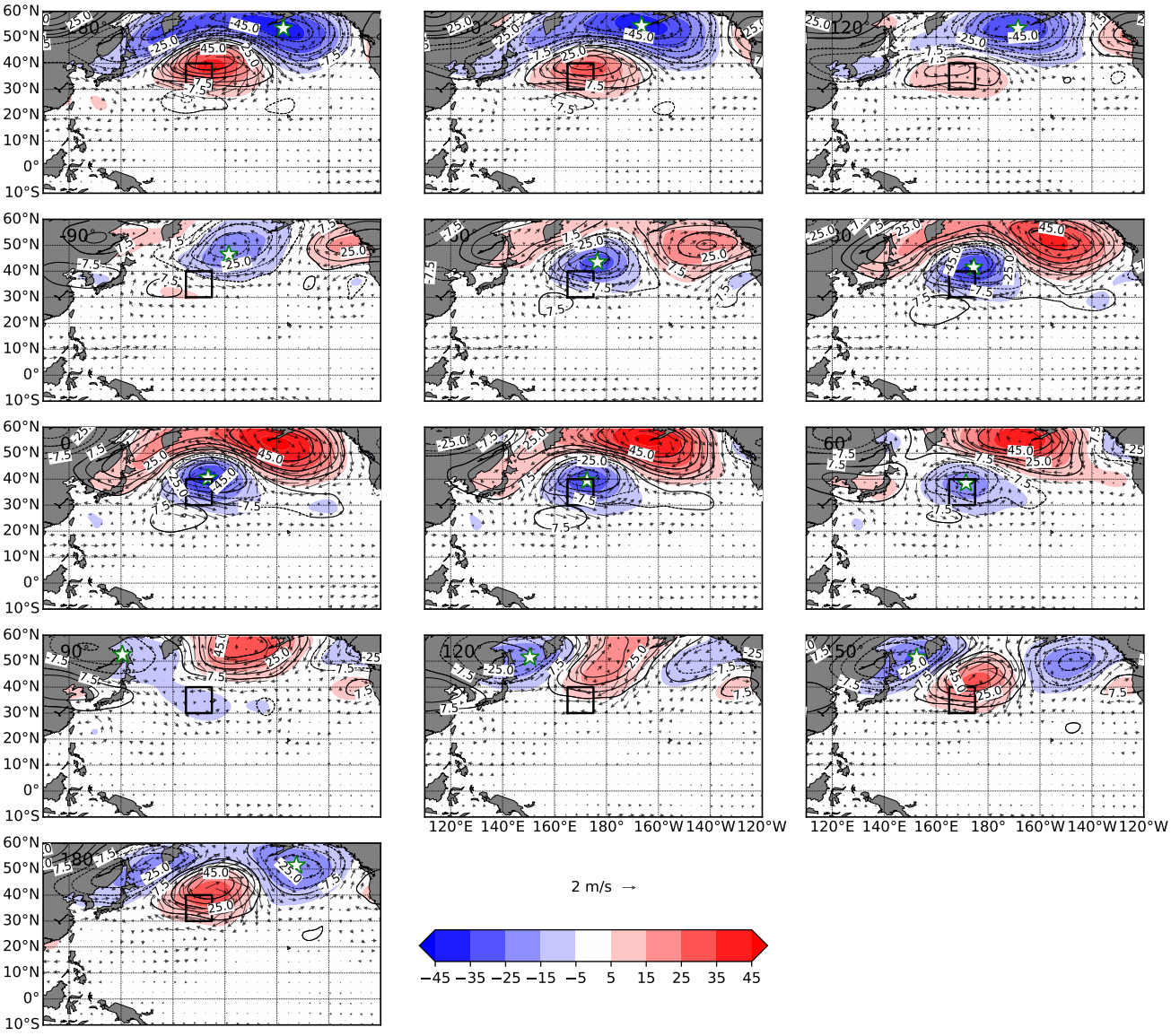

Fig. 2.7. Phase composite of a horizontal map of the anomalies of geopotential height (GPH) at 500 hPa (shaded; m), GPH at 250 hPa (contours; m, CI=7.5 m), and horizontal wind speed at 500 hPa (vectors; m/s). The black rectangle denotes the target area where the LCC anomaly index was calculated. Green star at each phase indicates the position of minimum of GPH anomaly (i.e. cyclonic anomaly) at 500 hPa.

2.3.3. Mechanism of evolution of LCC and changes in humidity field

As many previous studies shown, cold T_{adv} is known as a driver of LCC variability thorough an enhanced turbulence within the atmospheric boundary layer due to the upward surface buoyancy flux from the sea surface (e.g. Wood 2012). In the present chapter, we further investigated the LCC evolution process by focusing on the humidity field. The RH is an important atmospheric environmental controlling factor for LCC formation and cloud microphysics within the atmospheric boundary layer (rather than the specific humidity). Therefore, to determine the physical process of increasing (decreasing) LCCA that is associated with anomalously cold (warm) T_{adv} from the Euler perspective, we further investigated the variations of the q and RH fields associated with the cycle of the ISV of LCC using the same phase composite analysis method used in the previous section. Figure 2.8 shows the evolution of the area-mean vertical distributions of q and RH associated with the evolution of LCC. When the LCCA reaches a maximum at a phase of 0˚, the q anomaly is negative (dry) near the surface below 850 hPa, while the RH anomaly is positive (moist) there. The negative q anomaly results from the anomalous equatorward advection of cold dry air at a phase of 0˚ (Fig. 2.4). Compared with the humidity field near the surface, both the RH and q anomalies are positive between 700 hPa and 850 hPa at a phase of 0˚. When LCCA is minimum (at phases of −180˚ and 180˚), the signs of both humidity anomalies are opposite to those at a phase of 0˚. As described in Section 2.2, RH is a function of T and q. Therefore, the tendency of RH was decomposed into the contributions from the tendencies of T and q (Eq. 2.2) in an attempt to determine the physical process of LCC evolution on an intra-seasonal timescale. Figure 2.9 shows the observed tendency of RH and the contributions from changes in T (T-change) and q (q-change). As shown in Fig. 2.9a, the RH tendency is positive during the development stage of LCCA from a phase of −180˚ to 0˚ and negative in the dissipation stage from a phase of 0˚ to 180˚. The variation of RH tendency is corresponded well with the variation of LCCA. Next, we will discuss the contributions of T and q to the RH tendency as shown in Fig. 2.9b and c. In the development stage, the contribution from q-change is negative from the surface to 800 hPa; this is due to the anomalous dry advection mentioned above (Fig. 2.9b) and has an opposite sign to the RH tendency. In contrast, the contribution to the RH tendency from q-change is positive above 800 hPa. We also conducted an analysis of the specific humidity budget. The results suggest that the positive q and the contribution of q-change to the RH tendency are caused by the zonal advection of the q anomaly (not shown). On the other hand, the contribution from T-change below 700 hPa to RH is largely positive, which is also due to the anomalous cold advection (Fig. 2.9c). T-change makes the largest contribution to the RH tendency at around 900 hPa. However, above 700 hPa, the contribution of T-change to the RH tendency is small compared with that in the marine boundary layer (below 700 hPa). The results shown in Fig. 2.9a–c indicate that the contribution of T-change (q-change) to the RH tendency is dominant below (above) 700 hPa. It means that a decreasing (increasing) saturated water vapor pressure, caused by cooling (warming), promotes the formation (dissipation) of LCC in the development (dissipation) stage. Temperature budget analysis in the atmospheric boundary

layer below 850 hPa also indicates that meridional advection and diabatic cooling term due to the shallow convection are important for the temperature tendency compared with the others (Appendix 2B), in particular the cooling phase before phase of 0˚. Thus, we concluded that anomalous cold advection plays a key role in LCC formation through decreasing of saturated water vapor pressure, despite the fact that cold advection brings dry air in the development stage.

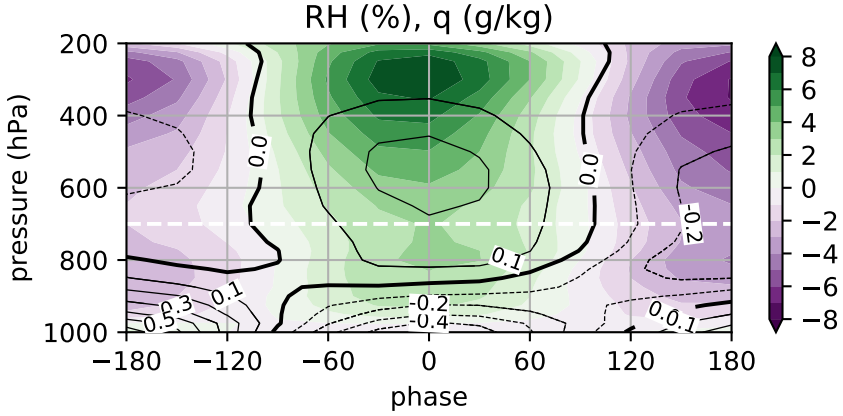

Fig. 2.8. Evolution of the vertical distributions of anomalies of relative humidity (RH; shaded; %) and specific humidity (q; contours; g/kg, CI=0.1 g/kg, TC=0 g/kg).

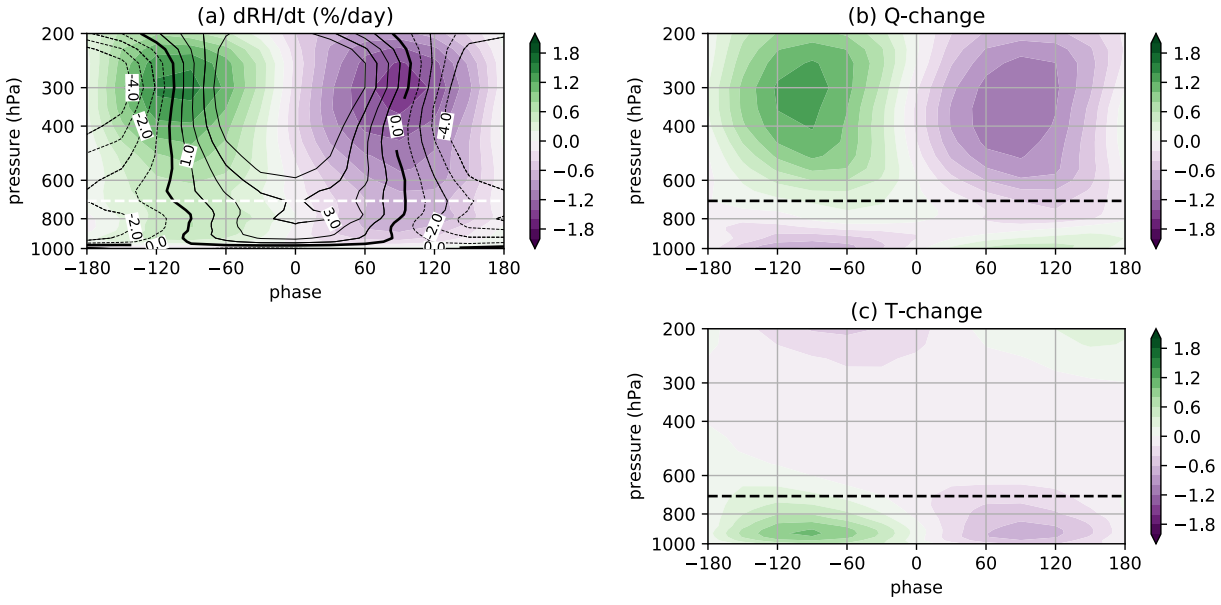

Fig. 2.9. As in Fig. 2.8, but for anomalies of **(a)** RH tendency (dRH/dt; shaded; %/day) and RH (contours; %, CI=1 %, TC=0 %), **(b)** dRH/dt by change in specific humidity (q-change; %/day), and **(c)** dRH/dt by change in temperature (T-change; %/day).

2.3.4. Air–sea interaction process between low-level cloud and SST associated with the ISV of LCC

In this subsection, we discuss the air–sea interaction processes among LCC, surface heat flux, and SST that are associated with the ISV of LCC. In Section 3.2, we determined the lead-lag relationship between the LCC and SST within a cycle of the ISV of LCC, showing that SST variation follows to LCC variation, that is, the maximum LCCA at a phase of 0˚ induces the minimum SSTA at a phase of 60˚ (Fig. 2.6). Surface heat flux into the subsurface ocean is a key component for determining SST variation in summertime NP. In particular, the reflection of incoming shortwave radiation (SW) at the sea surface by oceanic low-level cloud is an important factor in the decrease of SST in summertime NP. Besides the SW radiative heat flux, other factors which determine SST variability on an intra-seasonal timescale include turbulent heat flux, oceanic meridional advection, and Ekman pumping (Wang et al., 2012). In order to qualitatively investigate the relative importance of these factors, we evaluated each term of the mixed-layer temperature budget equation (Eq. 2.1). This equation requires the mixed-layer depth (MLD) at each phase. Unfortunately, no observational daily dataset of MLD exists; therefore, we used a constant value for the MLD (25 m) based on the climatological JJASO-mean MLD in the target region from the MIMOC dataset. Although MLD variation is an important factor for determining the SST tendency (Morioka et al., 2010), we ignored such variation in the present study. As explained above, some terms in the mixed-layer temperature budget equation are associated with oceanic processes (e.g., an advection term and an entrainment term) (Qiu and Kelly, 1993). However, we also ignored these terms because their contributions to SST tendency on an intra-seasonal timescale in summertime Kuroshio Extension region have been reported to be much smaller than the contribution of the surface heat flux term (Wang et al., 2012).

Figure 2.10a shows the evolutions of SST tendency and the surface heat flux term in Equation 2.2 at each phase, based on the phase composite analysis for the ISV of LCC. To the first order, the heat flux term can explain most of the variation of SST tendency. Additionally, there is a slight lag between the observed SST tendency and the heat flux term. We expect that this lag is due either to the fact that oceanic terms were ignored or to the uncertainty in the observational dataset for the total heat flux or SST. Figure 2.10b shows the decompositions of the surface heat flux into SW, longwave radiation (LW), sensible heat (SH), and latent heat (LH), and their evolutions. In addition to the term regarding the phase of SST cooling by surface heat flux (from a phase of −90˚ to 60˚; see Fig. 2.10b), SW and LH are two dominant factors for SST cooling. The contributions of SW and LH to SST cooling are almost the same in the cooling phase. The contributions of SH and LW to SST tendency are negligible compared with the contributions of SW and LH. The contributions of SW and LH to SST tendency are also dominant during the SST warming phase (from phases of 0−180˚ to 120˚ and 120˚ to 180˚, respectively; see Fig. 2.10b), however the SW heating is slightly larger than the LH heating.

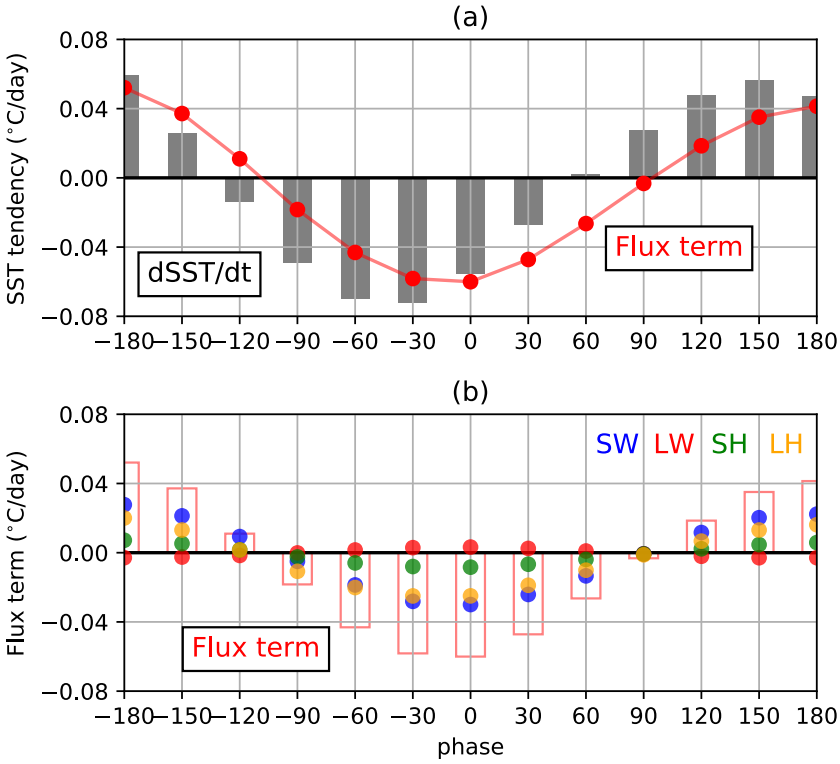

Fig. 2.10. (a) Evolution of anomalies of SST tendency (dSST/dt; black bar) and surface heat flux term (red circles). **(b)** Same as (a), but for anomalies of the total heat flux term (red bar), shortwave radiation (SW), longwave radiation (LW), sensible heat (SH), and latent heat (LH).

As shown in Fig. 2.10, the radiative flux term of SW variation corresponds to the LCC variability, meaning that an increase (decrease) in LCC increases (decreases) the albedo of the entire target region and suppresses (enhances) the downward SW radiation at the sea surface. However, the reason why LH variation is associated with the ISV of LCC is still unclear. Thus, we continued to analyze in detail the ISV of LH by linear decomposition of the bulk formula of LH as expressed below. LH variation is caused by a change in specific humidity at the sea surface (q_s) and near the sea surface (q_a), and a change in wind speed near the sea surface (WS_{10}). The upward LH at the sea surface is represented by the bulk formula

$$LH = \rho_a L C_E \, WS_{10} \, (q_s - q_a), \tag{2.3}$$

where ρ_a is the atmospheric density, L is the latent heat of vaporization, and C_E is the bulk coefficient. We decomposed the LH anomaly into the contributions from q_s, q_a, and WS_{10} using the following equation

$$LH' = \rho_a L C_E \{WS'_{10}(\overline{q_s} - \overline{q_a}) + \overline{WS_{10}}(q'_s) - \overline{WS_{10}}(q'_a)L + WS'_{10}(q'_s - q'_a)\}, \tag{2.4}$$

where the overbar denotes the climatological mean and prime denotes the anomaly from the mean. The first, second, and third terms on the right side of the equation are the contributions to the LH anomaly from changes in WS_{10}, q_s, and q_a, respectively. The fourth term on the right side represents a non-linear term related to changes in wind speed and specific humidity. We ignored the fourth term because its value is significantly smaller than those of the other three terms, differing by two orders of magnitude. Figure 2.11 shows the evolutions of the anomalies of WS_{10}, q_s, and q_a, (Fig. 2.10a), as well as their contributions to the LH anomaly (Fig. 2.10b). At a phase of 0˚, the WS_{10} anomaly is positive and the q_a anomaly is negative. Then, the contributions to the LH anomaly from WS_{10} and q_a are both negative. The amplitude of the contribution to LH from WS_{10} is slightly larger than those of the contributions from q_s and q_a. Additionally, the contribution to LH from WS_{10} is at the same phase as the total LH anomaly. Therefore, we conclude that LH variation associated with the ISV of LCC is driven mainly by WS_{10} change. The results of "strong" northerly winds is opposite sense to the climatological meridional wind direction; i.e mean southerly wind due to the North Pacific Subtropical High in boreal summer. However, scalar wind speeds on shorter timescale than sub-weekly does not depend on not climatological mean state but also synoptic atmospheric variability (Miyamoto et al., 2018; Ogawa & Spengler, 2019). Based on the overall results from Sections 3.2 to 3.4, we also suggest that the ISV of anomalous T_{adv} plays a key role in controlling the surface heat flux via changes not only in turbulent heat flux but also in radiative flux by modulating the evolution of LCC.

Finally, we further tested the regionality of the coupling process among LCC, SST, and T_{adv} described above in entire North Pacific. For this purpose, we performed a simple lead-lag correlation analysis without the filtering method, and without a phase composite analysis in not only the target region but also other region with the same domain size. Figure 2.12 shows the lead-lag correlation between the unfiltered but de-seasonal time-series of LCC and SST and T_{adv} in the target region and northeastern subtropical Pacific region (140˚W-150˚W & 20˚N-30˚N) where low-level cloud frequently appears. As suggested in Section 3.2, in the target region, the lag correlation between LCC and T_{adv} is negative and reaches a minimum at a lag of +1 day (Fig. 2.12a). This supports the result shown in Fig. 2.6 and indicates that anomalous T_{adv} plays a role in triggering LCC variation. In contrast, the lag correlation between LCC and SST is significantly negative from a lag of −8 to +1, and a negative peak appears at a lag of −2 (Fig. 2.12a). These two results imply that SST increases (decreases) after a decrease (increase) in LCC and the radiative impact of LCC on SST, which persists for about a week. As shown in Fig. 2.6, the LCC variability is a leading mode compared with the SST variability. The lag correlation coefficient if SST leads LCC (positive x-axis) is also slightly negative, however it is not significant except for a lag of +1 (Fig. 2.12a). The lead-lag relationship in northeastern subtropical region is quite similar to that in the target region, implying the similar air-sea interaction process described in the present chapter occurs in the other region. Figure 2.13 show horizontal maps of correlation coefficient at lag 0 of LCC and SST, and that of LCC and T_{adv}, respectively, using de-seasonal time-series in grid boxes with 10˚ resolution. We also displayed the

SST persistent days and T_{adv} leading days in each grid defined as the continuous days with the significant correlations at 95% level. Significant negative correlations of LCC and SST, and that of LCC and T_{adv} appears in two specific regions; (1) south of SST frontal region in western and central NP included in the target region and (2) northeastern (subtropical) NP, while SST persistent days are longer in the eastern NP than that in the western and central NP (Fig. 2.13a). The spatial feature of relationship is similar if we focused on only the intra-seasonal timescale (Fig. 2.13c, d). It suggested that lead-lag relationship among LCC, SST, and T_{adv} is robust in the two specific regions through air-sea interaction process presented in the present chapter. Regionality of the SST persistent days seems to be related with the horizontal distribution of oceanic MLD, e.g. MLD in the specific regions is about 25 m in boreal summer.

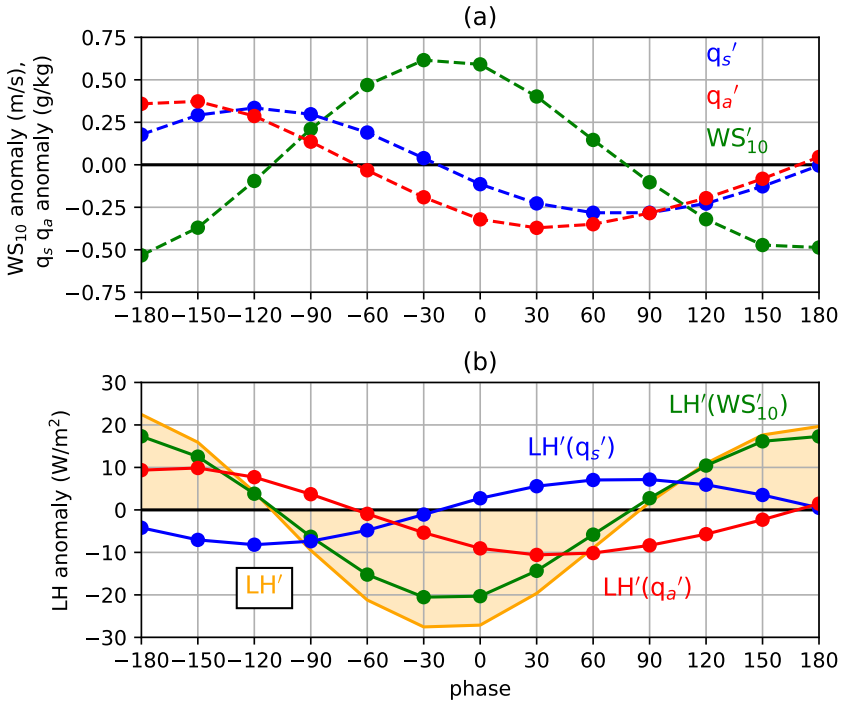

Fig. 2.11. (a) Evolution of anomalies of specific humidity at the sea surface (q_s; blue), specific humidity at the near-surface (q_a; red), and wind speed at 10 m (WS_{10}; green). **(b)** Same as (a), but for anomalies of latent heat flux (LH; orange shading), LH by q_s change ($LH(q_s)$; blue), LH by q_a change ($LH(q_a)$; red), and LH by WS_{10} change ($LH(WS_{10})$; green).

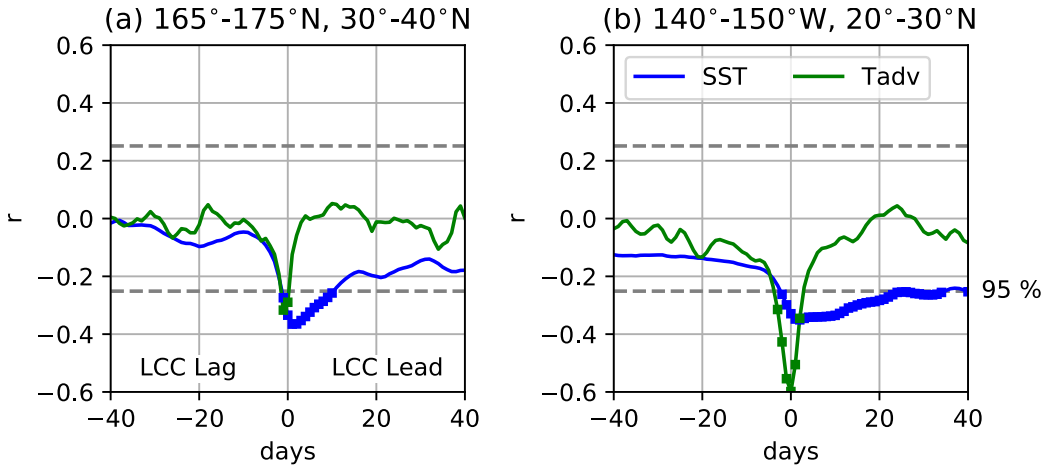

Fig. 2.12. Lag correlation coefficient between LCC and SST (blue) and between LCC and T_{adv} (green) derived from an unfiltered daily dataset for JJASO for 2003–2016 in (a) the target region (165˚E-175˚E & 30˚N-40˚N) and (b) northeastern subtropical Pacific region (140˚W-150˚W & 20˚N-30˚N). Lag correlation coefficients were calculated as mean values over 14 years. Horizontal dashed and solid lines indicate that the minimum correlation coefficient was exceeded at the 95% and 99% significance levels, respectively, calculated with an effective degree of freedom (Neff) of 152/50*12=36. Circles indicate when the coefficient at a certain lag day exceeds the 95% significance level.

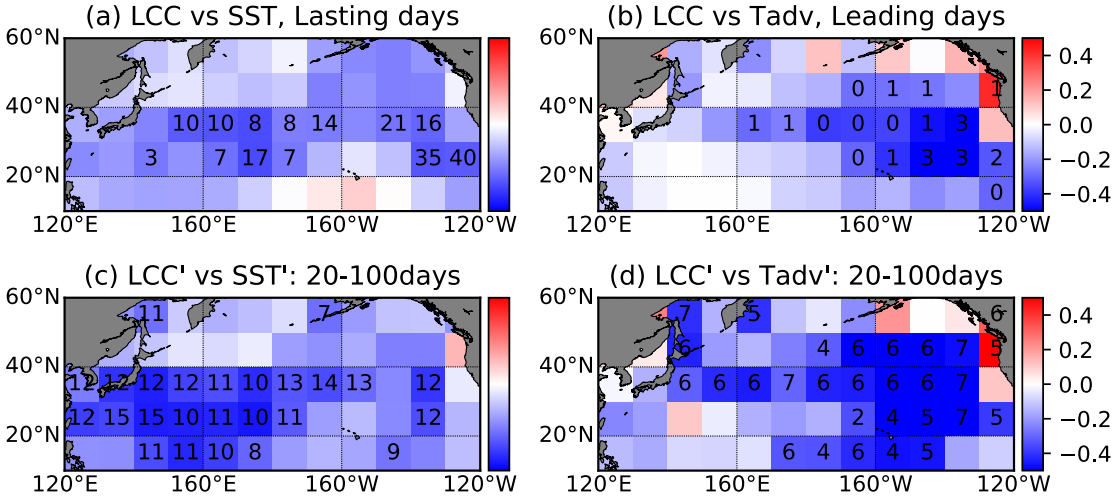

Fig. 2.13. Horizontal map of lag correlation coefficient between LCC and SST (left column) and between LCC and T_{adv} (right column) derived from a de-seasonal daily dataset (top row) and filtered datasets of intra-seasonal timescale (20-100 days) for JJASO for 2003–2016. Lag correlation coefficients were calculated as mean values over 14 years. Numbers in grid box indicate the lasting (leading) days of significant correlation coefficients of SST (T_{adv}) based on the days of maximum of LCC anomaly with 95% confidence level. Grid boxes without the number indicate any significant correlation coefficient do not appear in the day range for lag correlation calculation (from -40 to 40 days).

2.4 Discussion and Summary

This chapter revealed the intra-seasonal (20–100 days) variability (ISV) of oceanic low-level cloud cover (LCC) and associated LCC controlling factors, in particular SST and T_{adv}, in summertime NP using satellite observations and a meteorological reanalysis dataset. We applied a filtering method and a phase composite technique to the LCC anomaly (LCCA) in the western NP and extracted 46 cycles of the ISV of LCC using a 14-year JJASO dataset, whose mean amplitude and period are 11.3% in cloud fraction and 29.5 days, respectively. Within the cycle of the ISV of LCC, an increase in the LCCA is likely to be triggered by anomalous cold advection with a cyclonic atmospheric circulation pattern. Previous studies found that the ISV of the atmospheric circulation pattern in summertime NP is associated with internal atmospheric dynamics in the mid-latitudes (Wang et al., 2013) and remote forcing from the tropics (Mori and Watanabe, 2008). In the evolution process of increasing of LCC, anomalous cold advection is important for inducing a positive RH anomaly, due to the decrease in saturated water vapor pressure by anomalous cold temperature. This process encourages favorable conditions for the formation of LCCA in the lower troposphere below 700 hPa, despite the fact that cold advection brings dry air from the polar region.

Although SST and EIS are important factors controlling LCC variation on seasonal and inter-annual timescales (e.g. Klein and Hartmann, 1993; Klein et al., 2017), SST anomaly is followers to LCCA, that is, SST reaches a minimum after LCC reaches its maximum. EIS is also likely to follower of LCCA, however, further investigation is needed for the relationship between LCC and EIS because the result of their lead-lag relationship depends on overlapping assumption (Appendix 2A). Our thorough analysis of the mixed-layer temperature budget emphasized the importance of anomalous dry and cold advection for not only the formation of LCCA but also for the decrease in the local SST due to the enhanced release of turbulent heat flux. During the cooling phase of the SSTA, the positive LCCA induced by the cold advection leads to radiative cooling of the sea surface. Furthermore, the dry advection enhances the latent heat release from the sea surface. Originality of the present study is to reveal causal relationship implied by the lead-lag composite analysis within the air-sea interaction associated with ISV of LCC (e.g. positive feedback between LCC and SST [Norris and Leovy 1994]) in the summertime western North Pacific. The method is similar to Wang et al. (2012), however, differences in based variables for composite analysis between the present chapter and the previous study brought to us new insights for the formation mechanism of low-level cloud evolution, different pathway of SST variation, and regionality of the robust coupling among LCC, SST, and T_{adv} on intra-seasonal timescale.

Previous studies investigating the lead-lag relationship between cloud and ocean generally suggested that the ocean plays a passive role under the atmospheric forcing via surface heat flux in summertime mid-latitude ocean basins (Frankignoul and Hasselmann, 1977; Frankignoul and Reynolds, 1983; Frankignoul, 1985). We also obtained similar results with it, indicating the passive role of cloud radiative forcing and LH on SST on an intra-seasonal timescale. On the other hand, some

studies have suggested that the ocean plays an active role in the ocean-to-atmosphere circulation pattern on intra-seasonal and inter-annual timescales (Wang et al. 2012). Frankignoul et al. (2011) examined the atmospheric response to variability of the subarctic front associated with the cold Oyashio current and warm Kuroshio current, showing that a change in large-scale circulation is induced by a change in surface heat flux derived from the SSTA, especially in wintertime. Wang et al. (2012) proposed a two-way interaction process between the local SSTA and a change in atmospheric circulation during the transition phase of the change in vertical atmospheric structure from an anomalous barotropic to a baroclinic structure, related with the heating of the lower troposphere by SSTA. This suggests an active role of SSTA in promoting LCC formation in summertime NP. Mauger and Norris (2010) showed that SST has an active impact on the evolution of stratocumulus using the back-trajectory method with a meteorological reanalysis dataset. They also found that the horizontal distribution of SST along the pathway of low-level cloud is important to LCC evolution. Both these previous studies and the present study suggested that, when using local phase composite analysis, the Lagrangian method should be applied instead of the Eulerian method in order to determine the active impact of SST on the properties of oceanic low-level cloud.

Observational evidence of the impact of SST on LCC has been confirmed for inter-annual and longer timescales. However, the impact of SST on LCC has not been confirmed on shorter timescales, such as synoptic and intra-seasonal timescales. This is due to the fact that the dominant timescales of cloud and SST variabilities are less than 3 days and more than 7 days, respectively (Fig. 2.2a). This was also investigated by de Szoeke et al. (2016). This difference between the timescales of cloud and SST variability complicates the characterization of air–sea interaction. To further understand the importance of the interaction between cloud and ocean in mid-latitude oceanic basins for the timescale of cloud variability, it is necessary to consider and investigate the interaction process across different timescales; for example, the relationship between the monthly mean state and variability of LCC on a synoptic or intra-seasonal timescale. In other word, large variability of LCC appears in the region where mean SST is high and mean LCC is small around the specific meridional zone from 30˚N to 40˚N, which is implied in Fig. 2.1a and b. Further analysis is required using high temporal resolution cloud datasets (e.g., from geostationary satellites) for combined analysis of cloud variability on shorter timescale with SST variability on longer timescale.

Despite the difficulty in detecting the active role of SST in the evolution of LCC, the method used in the present chapter is useful for model output evaluation. Myers et al. (2017) evaluated the difference in the feedback processes of low-level cloud and SST in CMIP5 model outputs, showing that summer-to-summer SST variability depends on the representation of the feedback between low-level cloud and SST in each model. To reduce the uncertainty in the feedback process on an inter-annual timescale, it is necessary to reveal the complex process of low-level cloud evolution associated with many controlling factors. Additionally, evaluations of each air–sea interaction process on a timescale shorter than inter-annual are required. The method used in the present chapter is helpful to

better understand the physical processes involved in the evolution of LCC and evaluate model performance of the air-sea interaction.

Appendix 2A : Random overlap assumption for daily-mean dataset of MODIS

To estimate the "true" low-level cloud cover based on passive sensor, we applied the random overlap assumption in the present study. Basically, high-level cloud tends to co-appear with low-level cloud in the target region of western North Pacific. Thus, we investigated the vertical profile of cloud fraction observed by active sensor on CloudSat/CALIPSO corresponded with certain estimated LCC from passive sensor. We also compared the cloud occurrence profiles obtained from 2B-GEOPROF-LIDAR product based on estimated LCC from MODIS with "random overlap assumption" and "non-overlap assumption", Figure 2.A.1 show the composited-mean cloud occurrence profiles based on estimated LCC with and without the assumption. It shows that LCC estimated from random overlap assumption increases with increasing high-level cloud cover (HCC) (Fig. 2.A.1a). On the other hand, estimated LCC without any assumption increases with decreasing HCC (Fig. 2.A.1b). These results imply that LCC estimated from passive sensor in the western NP depends on middle- and high-level cloud covers, with large uncertainty due to the HCC variation. To confirm the conclusion about the lead-lag relationship among LCC, SST, EIS, and T_{adv}, we conducted the same analysis based on anomaly of LCC without random overlap assumption (Fig. 2.A.2). Results about the evolution of the area-mean anomalies of LCC without any assumption, SST, and T_{adv} is qualitatively similar to that with random overlap assumption. In contrast, lead-lag relationship between EIS and LCC is slightly different, that is, there is no lag between their variabilities. Thus, further analysis is needed for the LCC-EIS relationship in the western NP where high-level cloud occurrence is relatively frequent compared with northeastern subtropical Pacific.

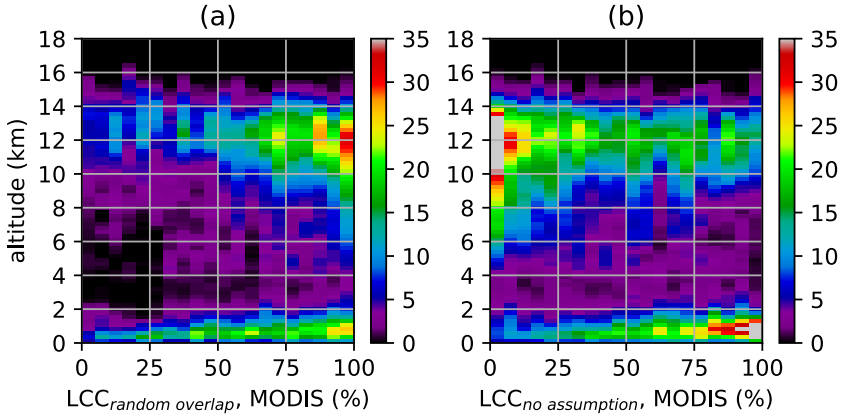

Fig. 2.A.1. Cloud occurrence profiles based on estimated LCC with **(a)** random overlap assumption and **(b)** no assumption in the target region (165˚E to 175˚E & 30˚N to 40˚N) from 2007 to 2010 JJA, using daily data of MODIS grid data and level2 profile data of 2B-GEOPROF-LIDAR product.

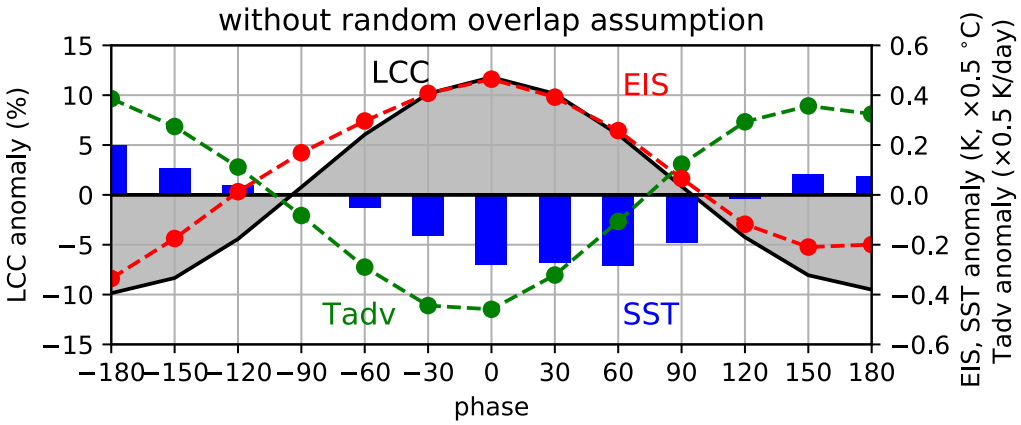

Fig. 2.A.2. As in Fig. 2.6, but for the results based on LCC anomaly calculated without random overlap assumption.

Appendix 2B : Temperature budget analysis in the atmospheric boundary layer

We estimated the detailed process of cooling atmospheric boundary layer which is important to modulate saturated water vapor pressure (Section 3.3). We applied the temperature tendency equation for filtered variables on intra-seasonal timescale described like below

$$\frac{\partial T'}{\partial t} = -\left(u\frac{\partial T}{\partial x}\right)' - \left(v\frac{\partial T}{\partial y}\right)' - \left(\omega\frac{\partial T}{\partial p}\right)' - \left(\omega\frac{\alpha}{c_p}\right)' + \left(\frac{Q_1}{c_p}\right)', \qquad (2.B.1)$$

where (u, v, ω) is the three-dimensional wind, α is the specific volume, and Q_1 is the apparent diabatic heating rate. A prime denotes the filtered variables (20–100 days). First three terms in the right-hand side (RHS) indicate the advection term, and fourth term in the RHS means adiabatic cooling term due to the vertical pressure velocity. Fifth term is diabatic heating term (i.e. radiative cooling, latent heating, surface turbulent heat flux, and so on), which is calculated as the residual of the Equation 2.B.1. Figure 2.B.1a displays the evolution of the area-mean anomalies of each term integrated in the boundary layer (from 850 hPa to 1000 hPa) calculated from the phase composite analysis based on LCCA in the target region, similar to Fig. 2.6. It indicates that cooling and warming within the boundary layer occurs before and after phase of 0˚, respectively. In particular, in the phases from -150˚ to -30˚, significant cooling occurs due to the meridional advection term and adiabatic cooling term (Fig. 2.B.1b). The adiabatic cooling term seems to be related with the shallow convection because the updraft occurs within the boundary layer when LCCA is positive (not shown). Additionally, in terms of the phase relationship between total temperature tendency term and each term in the RHS, the variation of meridional advection corresponded well with that of the total temperature tendency term. Thus, the results imply the importance of meridional cold advection in the atmospheric

boundary layer cooling process in the developing stage of LCCA (before phase of 0˚).

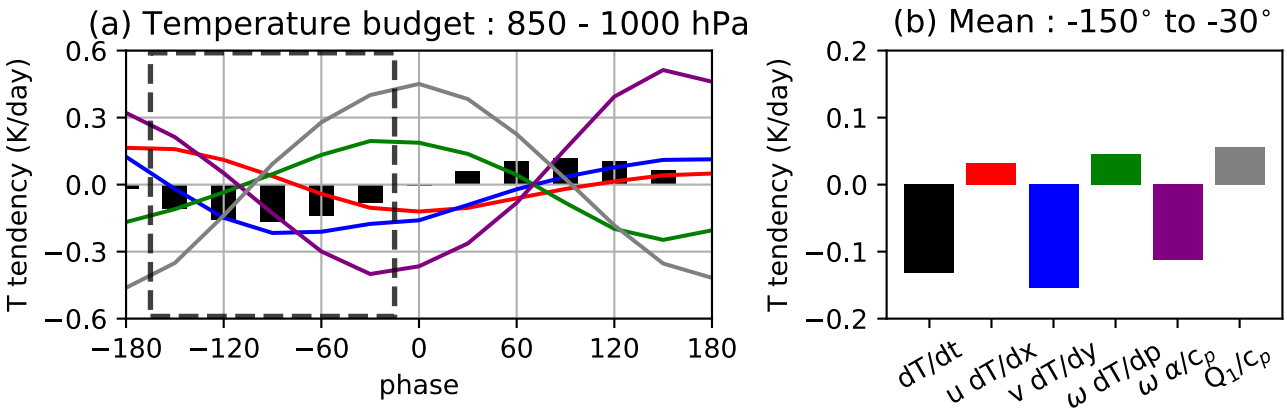

Fig. 2.B.1. (a) Composited mean of each term in temperature budget integrated from 1000 hPa to 850 hPa in the target region. **(b)** Phase-mean of each term in cooling phase (from phase -150˚ to -30˚) is also displayed. Colors in line and bar are corresponded within two panels (black: total tendency, red: zonal advection term, blue: meridional advection term, green: vertical advection term, purple: adiabatic heating term associated with vertical pressure velocity, grey: diabatic heating term calculated as a residual).

Chapter 3

Active Role of Oyashio Extension SST Front in Modulating Summertime Oceanic Low-Level Cloud based on WRF Numerical Experiments

3.1 Introduction

Sea surface temperature (SST) front is a key driver for modulating surface wind, atmospheric boundary layer properties, and mid-latitude atmospheric circulation on the mesoscale and large scale (Chelton, 2005; Frankignoul et al., 2011; Kuwano-Yoshida & Minobe, 2017; Minobe et al., 2010; O'Neill et al., 2005; Small et al., 2008; Xie, 2004). Through SST-induced atmospheric stability and secondary atmospheric circulation anomalies, the SST fronts also modulate cloud properties, including those of convective cloud on the warm western boundary current (Minobe et al., 2008) and oceanic low-level cloud (H. Kawai et al., 2015; Tanimoto et al., 2009; Tokinaga et al., 2009), namely, marine fog, stratus (St), and stratocumulus (Sc) in the subarctic region. The effect of the SST front on the atmosphere tends to be stronger in wintertime than in summertime due to the low air temperature over the sea surface and increased heat and moisture supplied by the sea surface (Nakamura and Yamagata, 1999). However, the state of the mid-latitude ocean in summertime is generally not recognized as the driver of atmospheric conditions because SST variability in summertime is mainly driven by atmospheric forcing rather than oceanic forcing. Thus, the active role of SST or SST fronts in summertime is not well understood in the mid-latitudes.

Although the active role of SST fronts in summertime may not be substantial, resent studies based on ship-based and satellite observations indicated that the SST front modulates the atmospheric boundary layer and low-level clouds overlying it (Tokinaga et al. 2009; Liu et al. 2014; Y. Kawai et al. 2015; Miyamoto et al. 2018; Jiang et al. 2019). There are local effects of the SST anomaly associated with the front on the low-level cloud and atmospheric boundary layer, such as thickness and turbulent mixing, in summertime. Most of the previous studies have focused on the relationship of the SST front with warm western boundary currents (i.e., the Kuroshio Extension in the North Pacific [NP], the Gulf stream in North Atlantic, and the Agulhas Return Current in the South Indian

Ocean), but not the relationship with cold western boundary currents (e.g., the Oyashio Current in the NP). There are warm and cold western boundary currents around Japan, called the Kuroshio and Oyashio Currents, respectively. Their confluence zone has a strong horizontal SST gradient, that is, an SST front, which is a main contributor to producing surface atmospheric baroclinicity in wintertime, which can enhance storm track activity (Nakamura et al., 2004). The detailed spatial distribution of the SST front reported by Kida et al. (2016) shows that the strongest SST fronts in the confluence zone are the Isoguchi Jets 1 and 2 (IJ1 and IJ2, respectively; Isoguchi et al. 2006), which are related to the Oyashio Extension (OE) trapped by the topography of the ocean floor around 42°N. The SST front in the Kuroshio Extension (KE) around 35°N is weaker than that in the OE, but heat and moisture supplies from Kuroshio Current and KE are the largest in the world due to large differences in air-sea temperature in wintertime. Thus, previous research has focused on the active role of KE in wintertime atmospheric variability. Although the cold SST anomaly associated with the Oyashio Current is not a heat source from the sea surface, the cold SST anomaly is important in stabilizing the lower atmosphere and increasing the amount of oceanic low-level cloud, especially in summertime (Klein & Hartmann, 1993; Norris & Klein, 2000). Thus, the climatological mean distribution of abundant low-level cloud spreads over the cold SST region, consisting of the NP and California off-coastal region. Moreover, the position of the Oyashio front around 42°N corresponds to the transition latitude of dominant cloud types for Sc and St-maritime fog on the southern and northern flanks of the front, respectively (Norris et al., 1998; Norris, 2000). Rather than the KE front, the cold SST anomaly derived from the cold Oyashio Current and OE is the key factor controlling low-level cloud properties in summertime.

Sub-seasonal variability of the low-level cloud is also modulated by the SST frontal characteristics through the horizontal air-temperature advection process near sea surface. Strong horizontal gradient of SST associated with the front can enhance the horizontal advection by enhancing the horizontal gradient of air-temperature around the front. It is one of important factors to control the low-level cloud properties through a modulation of the atmospheric boundary layer properties, such as turbulent mixing and thermodynamic conditions (Brueck et al., 2015; Klein, 1997; Miyamoto et al., 2018; Norris & Iacobellis, 2005; Xu et al., 2005; Zelinka et al., 2018). For example, warm advection over cold SST is a key driver for advected fog formation because the warm and humid advected air can be saturated due to the cooling by the SST (Koračin et al., 2014). In contrast, cold advection over warm SST induces the destabilization driven by turbulent heat flux from sea surface, exerting the decoupling of the marine boundary layer and the production of stratocumulus (Wood, 2012). Therefore, we speculate not only local SST anomaly but also horizontal distribution of the SST anomaly (i.e. SST frontal characteristics) can modulate the low-level cloud variability through the warm/cold advection process. The impact of SST front on the synoptic variability of low-level cloud properties is still unclear, and the mechanism needs further investigation.

In the present chapter, we pose the following two questions to reveal the mechanism. (1) How does the SST front affect the synoptic variability of the low-level clouds, especially when there are

northerly and southerly winds across the front? (2) Does the temperature advection strengthened by the SST front have a potential to modulate the low-level cloud properties, particularly the marine fog properties? We use numerical simulation with different boundary conditions because the difficulty in revealing the impacts of summertime SST and the SST front based on the observation arises from the positive feedback between the low-level cloud and SST (Norris & Leovy, 1994). We expect that the differences between two atmospheric simulations under the SST field with and without SST frontal characteristics should clarify the impact of the SST front on the low-level cloud. To evaluate the accuracy of the model output of low-level cloud, we examined the sensitivity of low-level cloud to different planetary boundary layer (PBL) schemes.

The structure of this chapter is as follows. Details of the model settings and experimental design are given in Section 3.2. We discuss the active role of the SST front in modulating low-level cloud properties in Section 3.3, and we show the results of the WRF model outputs related to the differences between the two experiments. Composite analysis results based on the meridional wind across the SST front are also shown to investigate how the effect of the SST front depends on meridional wind direction and speed. In Section 3.4, we provide a summary and discuss the new mechanism of the effect of the SST front on low-level cloud, especially maritime fog.

3.2 Data and Methods

3.2.1 Atmospheric Regional Weather Research and Forecasting Model

To investigate the response of oceanic low-level cloud properties to the SST front, we use the Weather Research and Forecasting model (WRF), version 4.0 (Skamarock et al., 2008, 2019), which is a nonhydrostatic atmospheric model. The WRF has been used in numerous studies to investigate the effect of oceans on regional atmospheric circulation (Kilpatrick et al., 2014, 2016), precipitation systems (Tanimoto et al., 2011; Xu et al., 2010), and cloud (Y. Kawai et al. 2015; Jiang et al. 2019). In this chapter, we use the WRF model to investigate the response of low-level cloud to the presence of an SST front.

The target regions in the WRF numerical experiments are shown in Fig. 3.1. The domain includes the two SST fronts associated with the OE located around 42°N. We set the two nested domains with horizontal resolutions of 30 and 10 km in the outer and inner domains (D01 and D02), respectively, with 57 sigma levels from the surface to 20 km. The calculation timesteps in D01 and D02 are 60 and 20 s, respectively. Nudging is done for only the outer domain to constrain the characteristics of the large-scale atmospheric circulation. The numerical simulation was carried out for 63 days from June 30 to September 1, 2016. However, we analyze the 2-month results for July to August, 2016 with 1-hourly output, considering the spin-up problem. We choose the following set of the schemes: the Mellor–Yamada–Nakanishi–Niino (MYNN) level-3 PBL scheme (Nakanishi &

Niino, 2006, 2009), the Kain-Fritsch cumulus parameterization scheme (Kain, 2004), the Thompson microphysical scheme (Thompson et al., 2008), and the rapid radiative transfer model and Dudhia schemes for longwave and shortwave radiation, respectively (Dudhia, 1989; Mlawer et al., 1997).

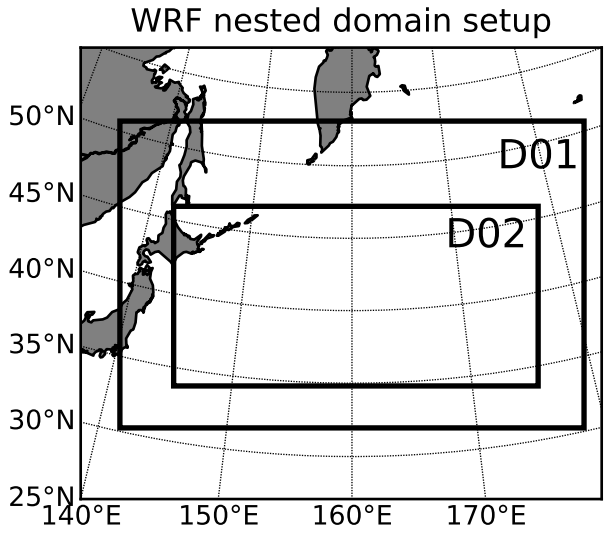

Figure 3.1. Domains of outer (D01) and inner (D02) regions for WRF experiments.

3.2.2 Experimental design

To examine the impact of the SST front on low-level cloud properties, we run two experiments with and without a strong horizontal SST gradient. The bottom boundary condition is fixed by the satellite-based SST obtained from the Optimum Interpolation Sea Surface Temperature (OISST) product, but the SST is updated once a day. The lateral boundary is given by the 6-hourly ERA-Interim dataset with 37 pressure levels. Figure 3.2 shows the horizontal distribution of period-mean SST in the two experiments. The control experiment (CTL experiment) is run with the original SST (shaded in Fig. 3.2) for 2 months during the target period, which includes the effect of the SST front on the atmospheric field. The other experiment is run with a spatially smoothed SST (SMO experiment), which is calculated by a spatial box-car filter (contours in Fig. 3.2). Spatial smoothing is applied over 9 pixels with the center as the target pixel and repeated 200 times for all pixels. Thus, the smoothed SST has a weaker horizontal gradient of SST; for example, the smoothed SST on the northern (cold) flank of the SST front is higher than that in the CTL experiment and vice versa (shown later in Fig. 3.4b). Lateral boundary conditions and physical scheme settings other than the bottom boundary conditions are the same in the two experiments. Thus, calculating the difference in CTL and SMO experiments allows us to determine the effect of SST and SST frontal characteristics on low-level cloud properties. However, in addition to the effect of local SST on low-level cloud, the large-scale atmospheric circulation changes associated with the SST front are included in the difference in the low-level cloud properties between the CTL and SMO experiments. However, atmospheric dynamical

response to SST front was ignored in the present study.

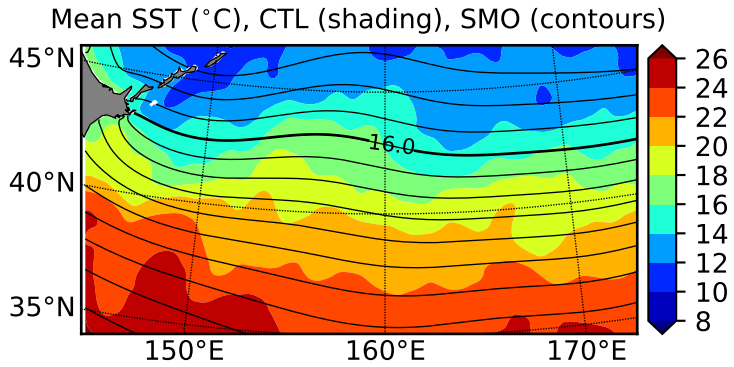

Figure 3.2. Horizontal distribution of period-mean SST in the CTL (shading) and SMO experiments (contours; contour interval: 1 °C; thick contour: 16 °C). SST in the CTL experiment is obtained from the OISST dataset.

3.2.3 Comparison of low-level cloud in the WRF model output with the observational dataset

We compare the period-mean fields of liquid water path (LWP) in the CTL experiment with a Moderate Resolution Imaging Spectroradiometer (MODIS) observational dataset to evaluate the low-level cloud properties in the WRF model output. The LWP of the WRF output is calculated by vertical integration of the cloud water content from the cloud bottom height to the top height. Cloud base and top height are defined as the lowest and highest altitude of continuous cloudy pixels, which are identified using the cloud fraction (CF) variable. In addition, LWP is calculated for only low-level cloud with a top pressure greater than 680 hPa.

First, we describe the MODIS observational datasets and the method for estimating the LWP distribution based on MODIS data. The latest release dataset (version 6) of level-2 product from MODIS from July to August 2016 is used. The variable compared is the LWP of low-level cloud with a top pressure below 680 hPa, consistent with the ISCCP classification. MODIS can estimate the LWP from visible reflectance with 5 km resolution in the swath; thus, LWP can be obtained only during the daytime at 1330 UTC. We re-grid the LWP in the level-2 swath into the WRF grid, and then we average it over the entire period. The period-mean LWP in the CTL run is also calculated at 1300 UTC under the same criteria for the cloud top pressure of low-level cloud. Figure 3.3a and b show the horizontal distribution of LWP from MODIS and the CTL run in the WRF simulation, respectively. We also plot the two SST front positions associated with the OE (IJ1 & IJ2) where the difference in SST between the CTL and SMO experiments is zero (shown in Fig. 3.4b). In the MODIS observation and WRF output, the LWPs on the northern flank of the SST fronts are larger than those on the southern flank. In general, a low SST is favorable for low-level cloud formation (Norris & Klein, 2000), so it is

consistent with the relationship between low-level cloud and SST in the summertime NP. Compared with the WRF output, the meridional contrast of LWP across the front is unclear in the observational dataset. Figure 3.3c shows a scatter plot of period-mean LWP from the MODIS observation and WRF output in each grid, with a correlation coefficient is 0.78. In addition, when the LWP in the WRF output is larger (smaller) than about 70 g/m^2, LWP in the WRF output tends to be larger (smaller) than in the MODIS observation. Although low-level cloud appears to be more sensitive to the SST front in the WRF output, WRF well simulates the low-level cloud properties compared with MODIS observational results.

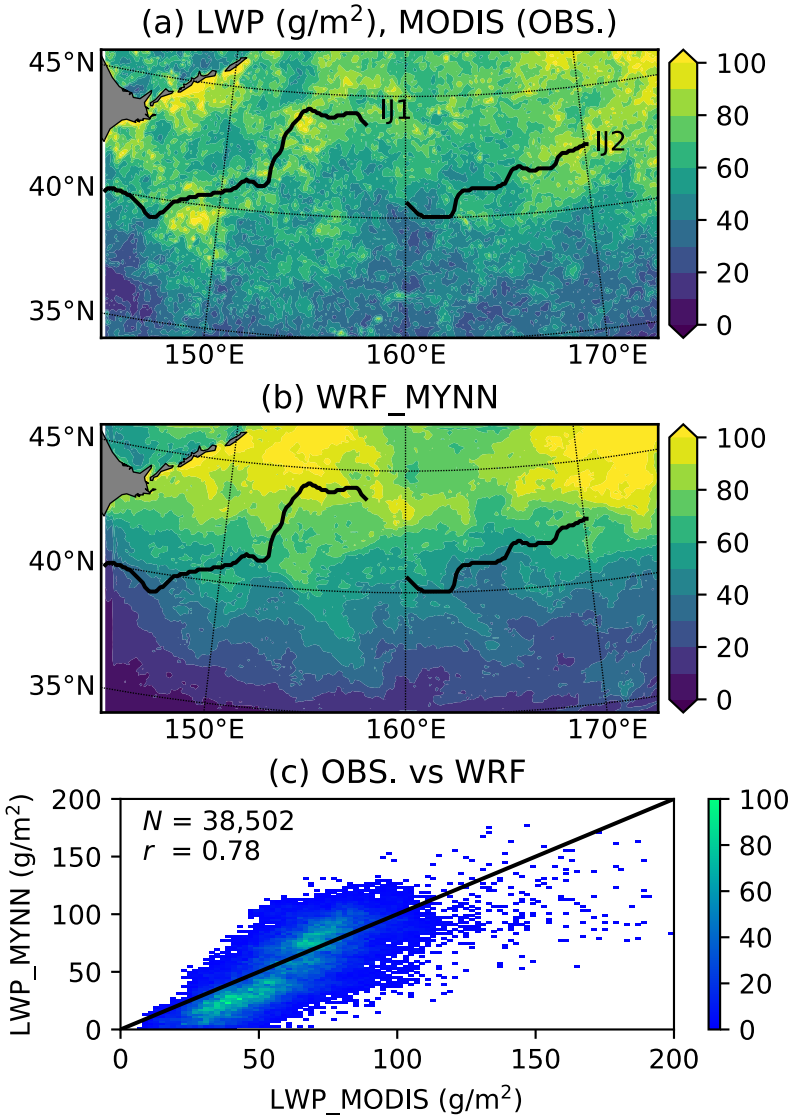

Figure 3.3. **(a)** Horizontal distribution of period-mean LWP of low-level cloud (cloud top pressure > 680 hPa) obtained from MODIS observations. **(b)** Same as (a), but for LWP in the CTL experiment with the MYNN PBL scheme. Black lines show the positions of IJ1 (left) and IJ2 (right) in (a) and (b). **(c)** Scatter plot of LWP from MODIS (x-axis) and WRF CTL experiment (y-axis). Sample number (N = 38,502) and correlation coefficient (r = 0.78) are shown in the upper left of (c).

Low-level cloud properties in the simulations are sensitive to the PBL scheme rather than the cloud microphysics scheme (Otkin & Greenwald, 2008). Thus, we test the sensitivity of period-mean LWP to the Yonsei University (YSU) (Hong et al., 2006), Mellor–Yamada–Janjic (MYJ) (Janjić, 1994), and MYNN (Nakanishi & Niino, 2006; 2009) PBL schemes. Detailed description about the sensitivity of LWP to PBL schemes is described in Appendix 3A, showing that the horizontal LWP distribution is so sensitive to the PBL scheme. The LWP distribution calculated with the MYNN scheme and the WRF simulation resembles that obtained from the MODIS observations. However, the LWPs calculated with the YSU and MYJ schemes are much larger than the results with the MYNN scheme and observational data (Fig. 3.A.1). Thus, we use the MYNN scheme in the following analysis.

3.3 Results

3.3.1 Impacts of SST front on the mean state of low-level cloud

Local SST anomalies affect the monthly mean states of LWP and CF of the low-level cloud through modulation of atmospheric stability and entrainment of dry-air from free troposphere (Bretherton et al., 2013; Klein & Hartmann, 1993; Norris et al., 1998; Norris & Leovy, 1994). First, we check the impact of the SST front on the mean state of the low-level cloud by calculating the difference in LWP between the CTL and SMO experiments for the entire period. Hereinafter, the differences in the cloud properties (= CTL − SMO) are indicated by Δ or referred to as "anomalies". Figure 3.4 shows the horizontal distribution of the period-mean anomalies of LWP and SST (Figs. 3.4a and b, respectively). There are two SST fronts associated with the OE in the target domain (black lines in Fig. 3.4); IJ1 (145–157°E) and IJ2 (160–170°E), characterized as dipole pattern of positive and negative SST anomalies on the northern and southern flanks, respectively (Fig. 3.4b). Along with the proposed mechanism of SST modulation for low-level cloud properties (Bretherton et al., 2013; Norris & Leovy, 1994; Terai et al., 2016, 2019), ΔLWP on the northern (southern) flank of the IJ2 front is positive (negative) with negative (positive) ΔSST, whereas ΔLWP on both flanks of the IJ1 front is negative (Fig. 3.4a). The region around the IJ1 front is located near the Japan islands; thus, we expect a more complex process to change low-level cloud and atmospheric circulation patterns owing to the effects of land. Hereinafter, we focus on the response of low-level cloud to the SST front around only the IJ2 front rather than the IJ1 front, to simplify the discussion of the cloud-SST relationship by removing the effect of land.

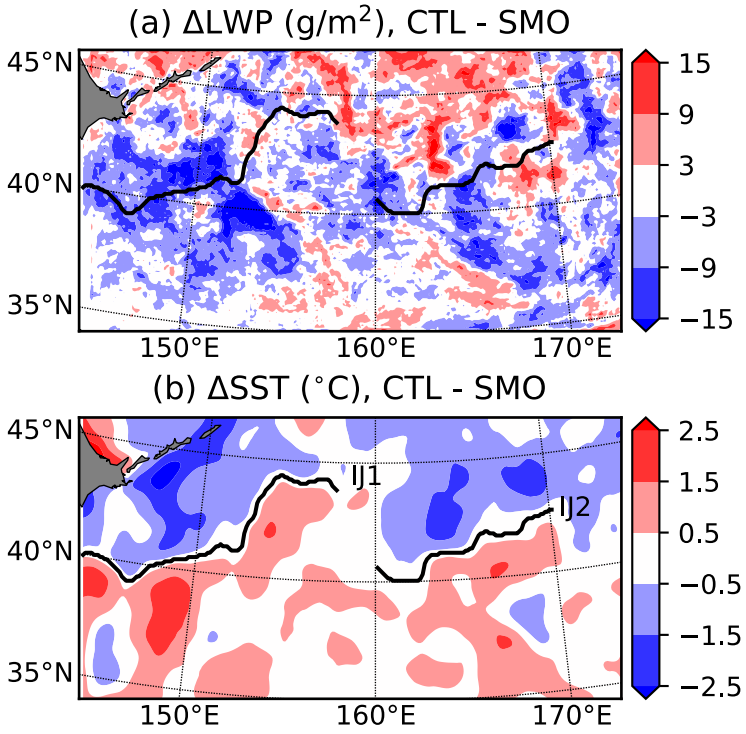

Figure 3.4. (a) Horizontal distribution of the difference in mean LWP (unit: g/m^2) of low-level cloud between CTL and SMO experiments. Black lines show the positions of IJ1 (left) and IJ2 (right). Definitions of the positions are described in Section 2.3. (b) Same as (a), but for SST (unit: °C).

Next, we examined the vertical structure of the low-level cloud around the IJ2 SST front to reveal the different responses of each cloud type; marine fog, St, or Sc. Figure 3.5 shows the period-mean vertical cross sections of cloud water mixing ratio (Q_c) around the IJ2 SST front and its response to the SST front (ΔQ_c), and the x-axis is the distance from the SST front, which is calculated as the minimum distance from each pixel point in the WRF simulation to the position of the IJ2 SST front. From the sea surface to an altitude of 0.5 km on the northern flank of SST front ($x > 0$ km), the mean of Q_c has a maximum value which is larger than 0.035 g/kg (Fig. 3.5a). This peak corresponds to the marine fog because its cloud base height reaches the surface. The Q_c of marine fog increases by 20%-40% due to the low SST anomaly between CTL and SMO experiments (Fig. 3.5b). Abundant marine fog appears in the NP (>40°N) owing to climatological-mean warm and moist advection from low latitudes (vectors in Fig. 3.5a) over low SSTs inducing high lower atmospheric stability (H. Kawai et al., 2016; Koshiro et al., 2017; Koshiro & Shiotani, 2014). Another Q_c peak also appears at an altitude of around 1.0 km on the northern flank (Fig. 3.5a), corresponding to St or Sc (St-Sc). Response of Q_c in this cloud type on the northern flank is negative and opposite to the marine fog response (Fig. 3.5b). Here, we also classified the altitude as "marine fog region ($0 <$ altitude [z] < 0.5 km; red line)" and "St-Sc region ($0.5 < z < 1$ km; blue line)". The Q_c of marine fog increases (decreases) on the northern (southern) flank of the front, whereas Q_c of St-Sc decreases over both flanks (Fig. 3.6). The response

to the SST front depends on cloud type, and the marine fog is more sensitive to the presence of the SST front than the St-Sc. Hereinafter, we mainly focus on the response of the marine fog to the SST front.

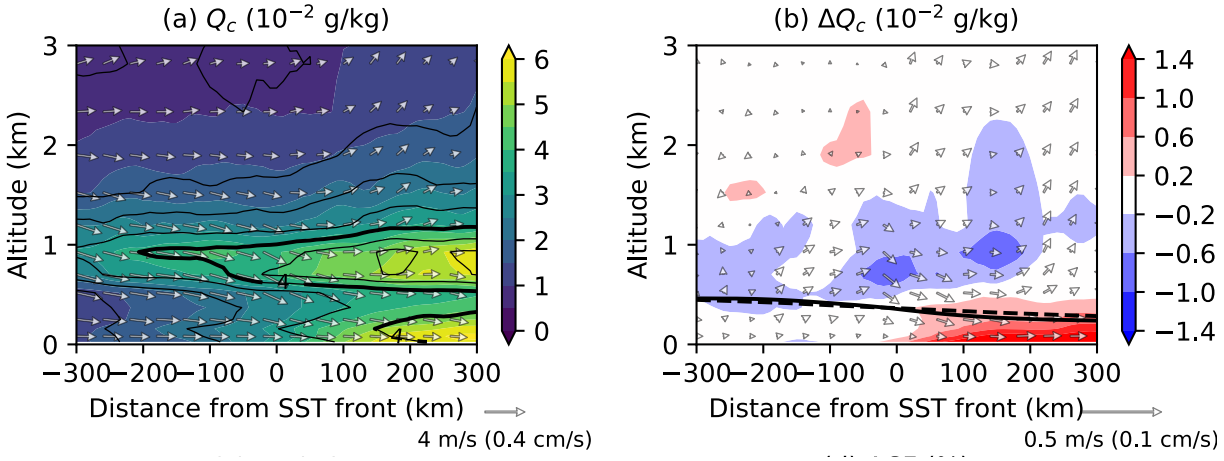

Figure 3.5. (a) Vertical cross section of the period-mean Q_c [$\times 10^{-2}$ g/kg] in CTL (shaded) and SMO (contours; CI = 0.5 $\times 10^{-2}$ g/kg, thick contour is 4×10^{-2} g/kg) experiments around IJ2. *x*-axis is distance from IJ2 front (unit: km), *y*-axis is altitude (unit: km). **(b)** Cross section of the difference in Q_c between CTL and SMO experiments. Solid and dotted lines show period-mean boundary layer height in CTL and SMO experiments, respectively.

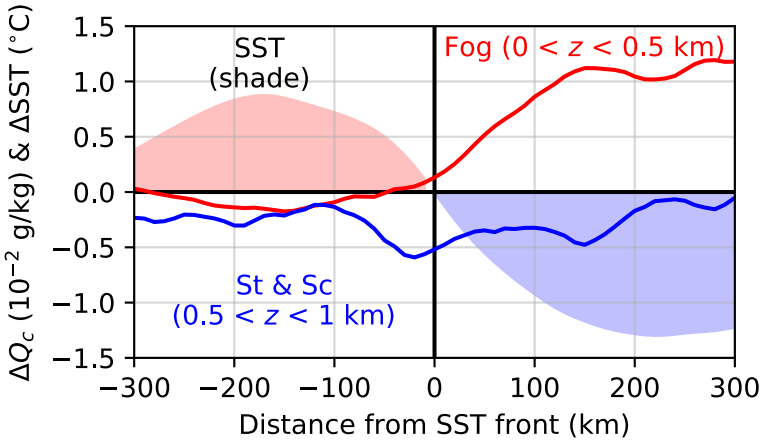

Figure 3.6. Mean meridional distribution of the difference in vertical mean Q_c of the fog region ($0 < z < 0.5$ km) and St-Sc region ($0.5 < z < 1$ km; red line) for IJ2 (160–170°E; blue line) between the CTL and SMO experiments as a function of distance from the position of IJ2 (left *y*-axis; g/kg). The difference in SST is also shown in shaded plot.

3.3.2 Impacts of SST front on the synoptic variability of low-level cloud properties

Temperature advection near the sea surface is a key factor for controlling low-level cloud properties through the modulation of the atmospheric boundary layer and turbulent heat flux from the ocean to the atmosphere (e.g. Klein 1997). In general, warm (cold) advection exerts stable (unstable) conditions near the sea surface, promoting the formation of the marine fog (Sc) (e.g. Wood 2012; Koračin et al. 2014). In summertime in the western NP, the mean meridional wind field is southerly (Fig. 3.5a) and contains warm and moist air, mainly controlled by the large-scale, high-pressure system called the North Pacific Subtropical High. As a result, marine fog in the northern flank of the SST front frequently appears, as shown in Fig 3.5a. However, the temperature advection with meridional wind across the SST frontal changes on a day-to-day timescale, which is induced by synoptic disturbances. Because low-level cloud types and the formation mechanism are different with warm and cold temperature advection, we hypothesize that the impacts of the SST front on the low-level cloud properties in summertime (i.e. difference between CTL and SMO experiments) are different for northerly and southerly winds. To further investigate the mechanism of the low-level cloud response to the SST front, we conduct composite analysis based on meridional wind 10 m from the sea surface (v_{10}) just over the SST front position, that is, northerly (v_{10} < -2 m/s) vs southerly (v_{10} > +2 m/s), for Q_c and thermodynamic conditions. Environmental thermodynamic conditions are investigated because these cloud types and their response to the SST front depend strongly on warm/cold advection-induced atmospheric boundary layer properties. Figure 3.7 shows a histogram of v_{10} just over the SST front position for the entire target period and indicates that the mean meridional wind is southerly. There are 35,493 and 47,679 northerly and southerly composite cases, respectively.

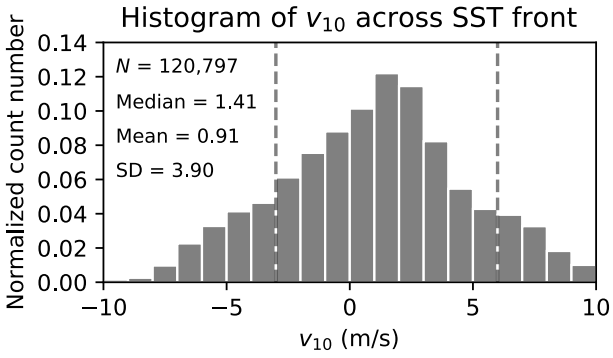

Figure 3.7. Normalized histogram of the meridional wind at 10 m (v_{10}; unit: m/s) across the IJ2 SST front position. Note that positive (negative) value of v_{10} indicates southerly (northerly) across the SST front. Only the v_{10} range between the vertical dashed lines is used in Figs. 3.12, 3.13, and 3.14 (from -3 to +6 m/s). SD: standard deviation.

i. Southerly case

Figure 3.8a and b show the vertical cross sections of the mean Q_c for the southerly case superimposed with meridional and vertical wind fields. The cross section of Q_c on the northern flank is similar to the mean state of the entire period (Fig. 3.5a), which has a Q_c peak near the surface (i.e., marine fog) and one around 1 km (i.e., St-Sc), although St-Sc Q_c around the latter peak is slightly smaller (Fig. 3.8a). Vertical velocity for the southerly case is smaller around the IJ2 front compared with the northerly case, in which the speed increases toward the sea surface (Fig. 3.8a). Consistent with Norris et al. (1998) and Norris & Klein (2000), southerly wind with warm and moist air increases marine fog formation. The cold SST anomaly on the northern flank of SST front increases ΔQ_c for marine fog but not for St-Sc (Fig. 3.8b). In contrast, no large response of ΔQ_c on the southern flank of the SST front is observed.

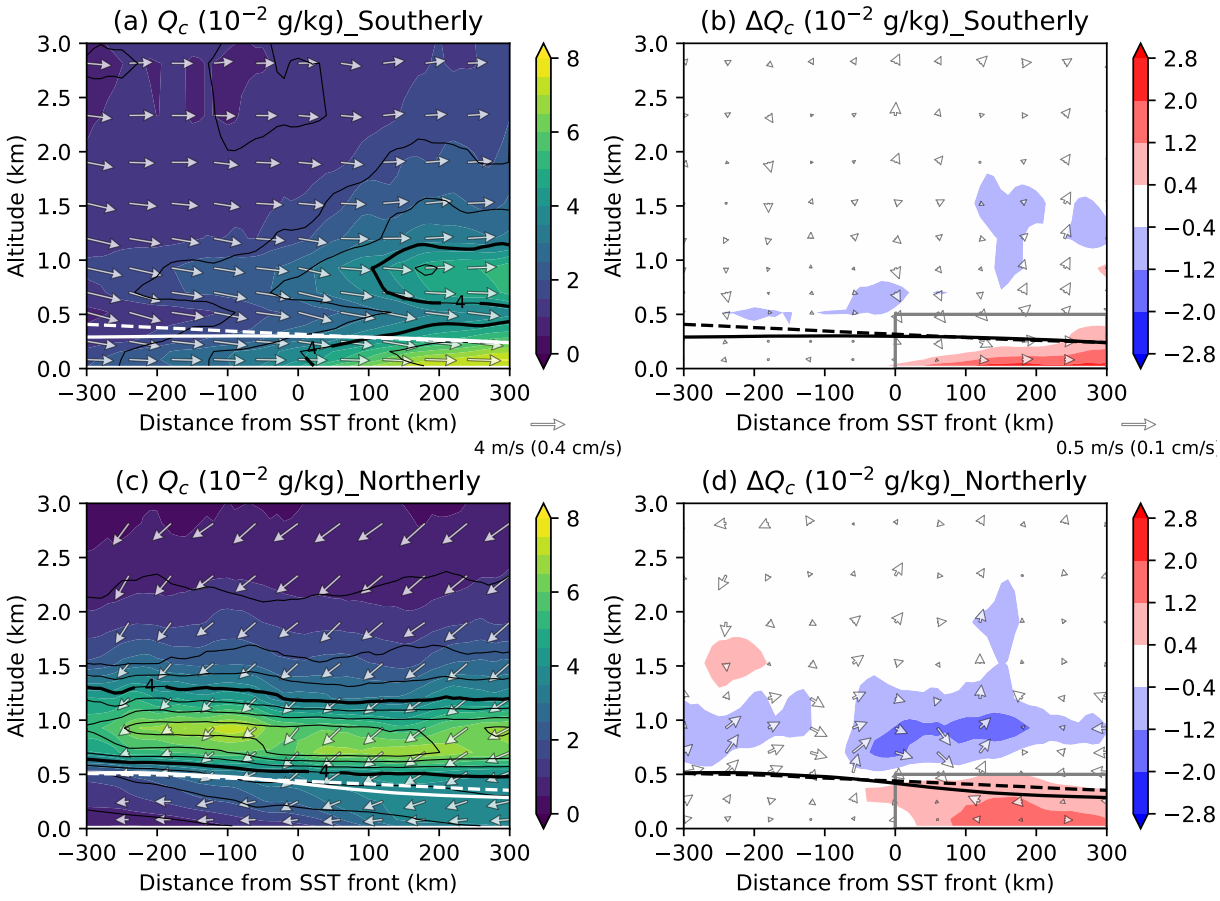

Figure 3.8. Same as Fig. 3.5a and b, but for the **(a), (b)** southerly (v_{10} > 2 m/s) and **(c), (d)** northerly (v_{10} < -2 m/s) wind cases based on meridional wind at 10 m (v_{10}) across the IJ2 front position. White and black lines show the boundary layer height in the CTL (solid) and SMO (dashed) experiments. Gray box shown in (b) and (d) indicates the marine fog region in the northern flank of the SST front, used in Fig. 3.11 and 3.14.

Figure 3.9 shows the vertical cross sections of the difference in thermodynamic variables between the CTL and SMO experiments in the southerly wind case. The SST front modulates the thermodynamic state of lower troposphere, especially near the sea surface on the northern flank, resulting in a colder potential temperature (θ, Fig. 3.9a), lower water vapor mixing ratio (Q_v, Fig. 3.9c), and lower turbulent kinetic energy (TKE, Fig. 3.9e) in the CTL experiment than in the SMO experiment. These cold temperature and dry anomalies are derived from the cold SST anomaly on the northern flank. Owing to the high SST anomaly on the southern flank, the thermodynamic variable anomalies have opposite signs to those on the northern flank. Relative humidity (RH) is an important parameter that indicates how readily water vapor can be converted to cloud water droplets rather than absolute amount of water vapor, as measured by specific humidity or Q_v. The changes in RH near the sea surface on the northern flank are almost zero. Further analysis was conducted for decomposition of RH changes by temperature and Q_v because RH is a function of the two variables. We decomposed the RH change into that caused by temperature and Q_v, following the method of (Babić et al., 2018). Fig. 3.9 d and f are the results of the decomposition, showing that two contributions cancel each other out because the positive and negative contributions to RH from decreasing T and decreasing Q_v, respectively. This result implies that the low-temperature anomaly due to the cooling by SST could increase RH on the northern flank near the sea surface because saturated water vapor pressure decreases with temperature, which has a potential to enhance the marine fog formation (Fig. 3.9d).

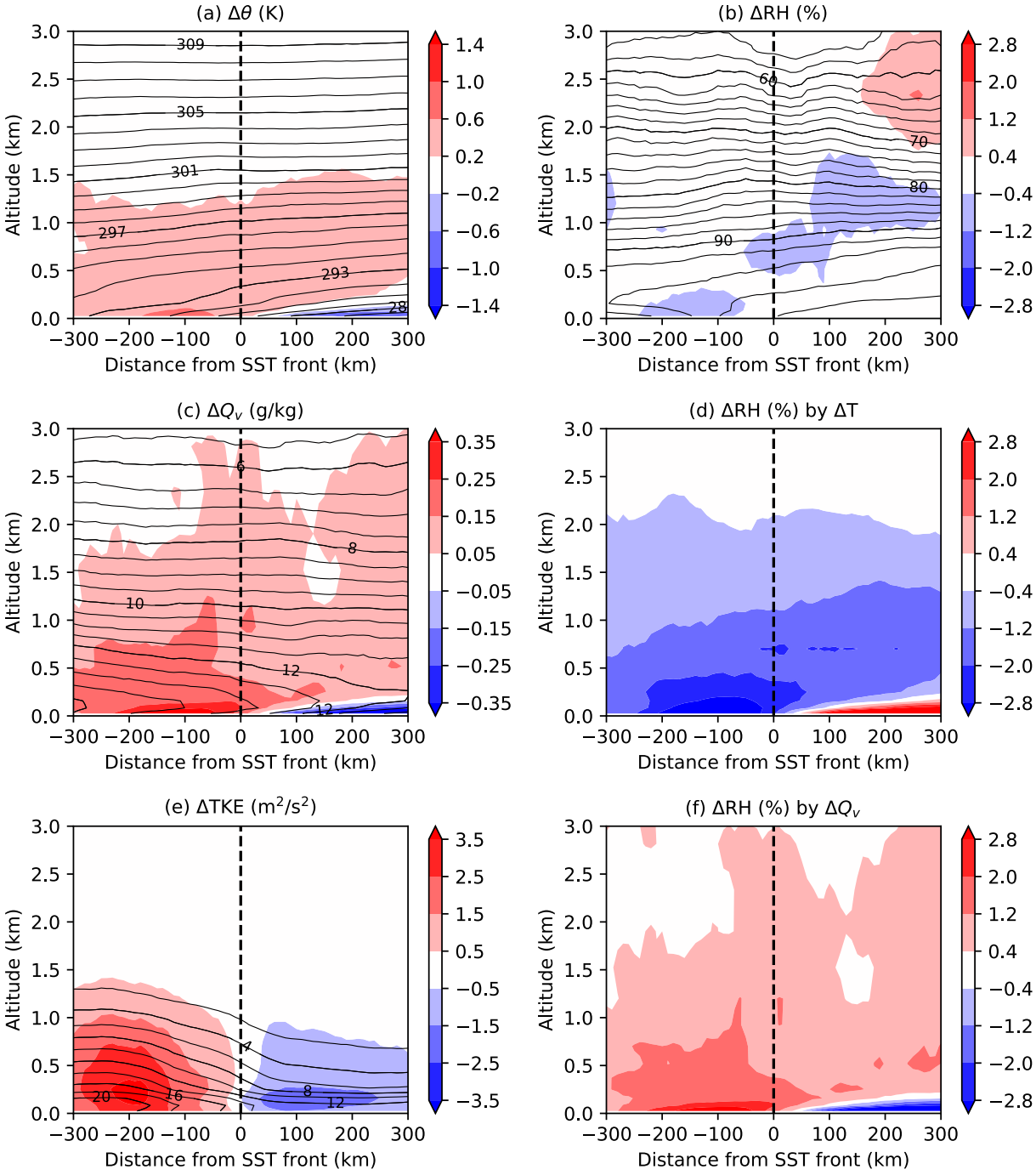

Figure 3.9. Same as Fig. 3.8b, but vertical cross section of the mean state in the CTL experiment (contour) and the difference between CTL and SMO experiments of **(a)** θ (CI = 1 K), **(b)** RH (CI = 2%), **(c)** Q_v (CI = 0.5 g/kg), **(e)** TKE calculated by the PBL scheme (CI = 2 m^2/s^2) for the southerly wind case. **(d), (f)** Same as (b), but for relative contribution to total ΔRH by temperature (ΔT) and Q_v (ΔQ_v), respectively. Vertical dashed line indicates the position of the IJ2 front.

ii. Northerly case

The mean states of the vertical structure of low-level cloud are different for the northerly case compared with the southerly case. The mean Q_c near the sea surface related to marine fog is substantially smaller on both flanks of the front (Fig. 3.8c) due to the destabilization process near the sea surface induced by the cold air advection. Instead of a smaller amount of the marine fog, mean Q_c related to St-Sc has a maximum peak around 1 km on both flanks (Fig. 3.8c). Unlike the meridional contrast of Q_c for marine fog across the SST front for the southerly wind (Fig. 3.8a), the meridional contrast of St-Sc is unclear. The amount of St-Sc cloud is increased by near-surface destabilization, shown by the larger mean TKE for the northerly wind than for the southerly wind (Fig. 3.9e vs 3.10e), consistent with previous studies (Wood, 2012). These results also indicate that the WRF model can reproduce the low-level cloud and sensitivity of low-level cloud to warm/cold advection well. The spatial pattern of ΔQ_c for the northerly case is similar to that for the southerly wind (Fig. 3.8b, d); however, ΔQ_c of St-Sc over the SST front is negative (Fig. 3.8d). For both the northerly and southerly winds, ΔQ_c of marine fog on the northern flank is positive, but ΔQ_c for the northerly wind is more positive. The difference in the response of ΔQ_c to the SST front is also corresponded with that of ΔRH (Fig. 3.8d vs 3.10b). Compared with the southerly wind, ΔRH near the sea surface on the northern flank is more positive due to lower temperature anomalies (Fig. 3.10d). The reason why the difference in cooling process within the atmospheric boundary layer is derived from the advected cold air mass with northerly wind from the poleward direction. The detailed process is discussed in the next subsection.

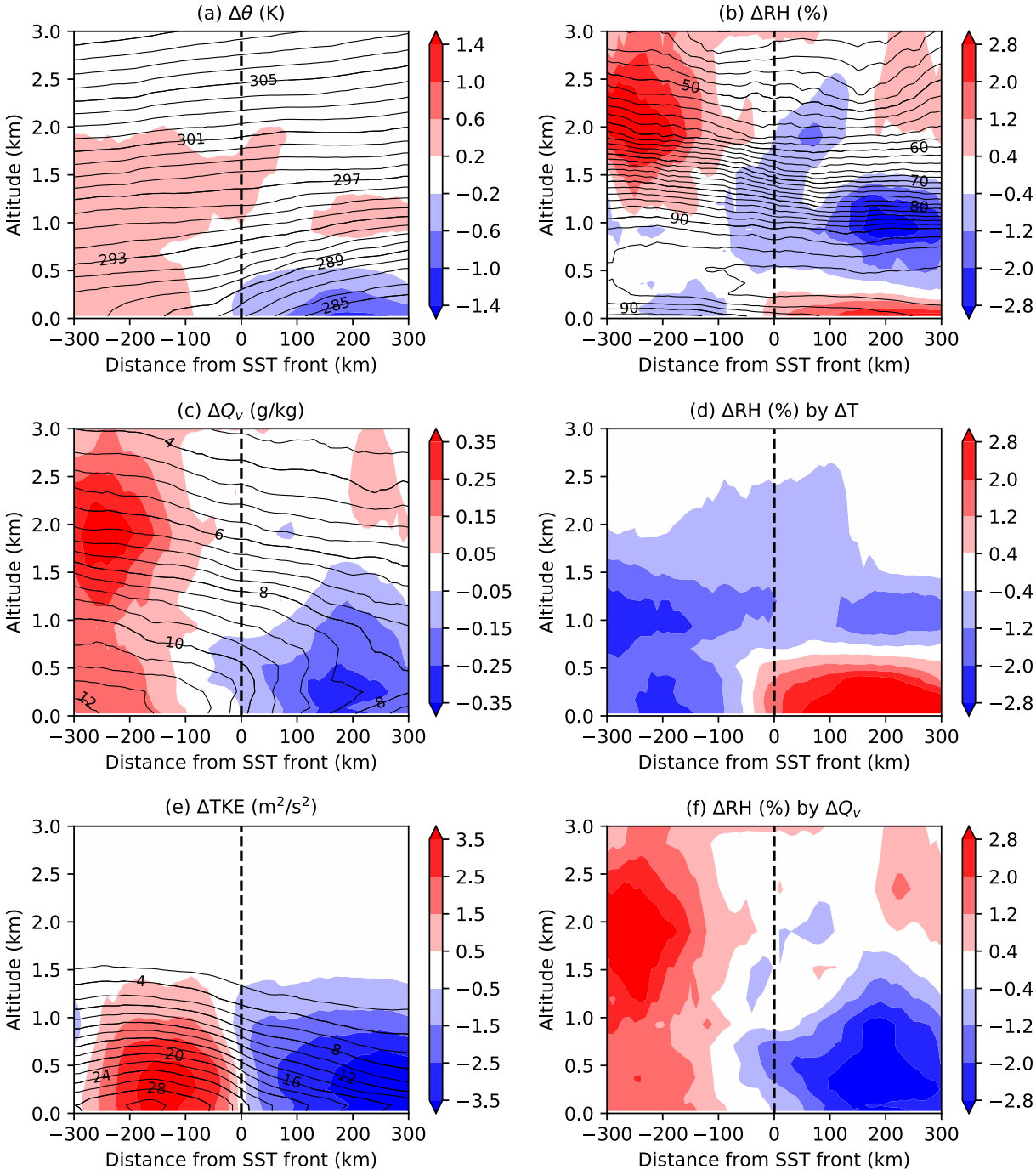

Figure 3.10. Same as Fig. 3.9, but for the northerly wind case (v_{10} < -2 m/s).

3.3.3 Mechanisms of the impact of SST front on marine fog with northerly or southerly; SST anomaly effect vs SST frontal effect

The composite results for northerly and southerly cases suggested that impact of the SST front on the low-level cloud properties (i.e. ΔQ_c), particularly for the marine fog on the northern flank, depend on meridional wind across the front (Fig. 3.8). ΔRH in the marine fog region on the northern flank also depends on the meridional wind, which is a key factor for the marine fog formation and strongly modulated by ΔT (Figs., 3.9b, 3.9d, 3.10b, 3.10d). As proposed mechanism of the Q_c response to the SST front with a diagnostic thermodynamic field, namely, a temperature and RH field, the Q_c of marine fog is strongly affected by local SST anomalies and has a clear meridional contrast across the SST front. Most previous studies focus on the effect of only a local SST anomaly; for example, a cold SST anomaly can create a more stable temperature profile (Klein & Hartmann, 1993), suppress the entrainment of dry air from free troposphere to the boundary layer (Bretherton et al., 2013), and enhance the low-level cloud formation. Hereinafter, we refer to the effect of a local SST anomaly on the marine fog properties as the *SST anomaly effect*. The horizontal advection process, however, is also important to control the thermodynamic and low-level cloud fields from the Euler perspective, which is amplified by the SST frontal characteristics. For example, warm temperature advection flowing into the northern flank can be strengthened by not only negative SST anomaly on the northern flank but also the positive one on the southern flank, that is, the strong horizontal gradient of air temperature associated with the SST front. The advected warm air into the northern flank of the front reduces the RH and low-level cloud amount on the northern flank due to the increasing saturated water vapor pressure. We refer to this effect on the marine fog related to the horizontal advection process as the *SST frontal effect*, which is modulated by the horizontal gradient of SST and the meridional wind across the front. There are two candidates as the SST frontal effect suppressing the marine fog formation on the northern flank; (1) advection of negative Qc anomaly caused by positive SST anomaly on the southern flank and (2) advection of warm air temperature anomaly from the warm to cold flanks that increases saturated water vapor pressure and suppresses the fog formation. To separate the effects, we performed budget analysis of the *Qc* of the marine fog, more sophisticated composite analysis based on meridional wind across the front, and temperature budget analysis in the marine fog region on the northern flank.

i. Budget analysis of cloud water mixing ratio in the marine fog region

First, we investigated the budget term of the cloud water mixing ratio of the marine fog on the northern flank to clarify the contributions of the advected process of the Q_c anomaly to the total tendency of Q_c anomaly. In the microphysical scheme used in the WRF numerical simulation, mixing ratio of each water phase is calculated as follows (Skamarock et al., 2008)

$$\frac{\partial Q_m}{\partial t} + (\nabla \cdot V q_m) = F_{Q_m}, \tag{3.1}$$

where q_m is the mixing ratios for water vapor, cloud, rain, ice, and etc. (mass per mass of dry air), F_{Q_m} is a diabatic term arising from the microphysics scheme. Q_m and V are the coupled variables of mixing ratio and wind, respectively, which are the product of the mass per unit area within the column (μ_d), representing the air mass-weighted variables. In the Thompson microphysical scheme, the diabatic term is composed of condensation, evaporation, accretion, and collection. Although we ignore the four individual components of the diabatic term in this paper, we can discuss the relative importance of local and advective processes for low-level cloud formation by comparison using the advective term ($-\nabla \cdot V Q_c$) and overall diabatic term (F_{Q_c}). To evaluate the relative contribution of the advection and diabatic terms for *Qc* tendency of marine fog near the sea surface on the northern flank, we calculate the difference in period-mean each term in the target region (gray rectangles in Fig. 3.8b, d) between the CTL and SMO experiments for the northerly and southerly winds (Fig. 3.11). The difference indicates how much each budget term is modulated by the SST front. In the target region, ΔQ_c is positive (Fig. 3.8b, d) for both cases, meaning that marine fog formation is increased by the presence of SST front. This result is consistent with the positive anomaly of total tendency of Q_c in the CTL experiments (black bars in Fig. 3.11). The positive difference is larger for the northerly wind than for the southerly wind, associated with the larger RH near the sea surface induced by decreasing the saturated water vapor pressure (Figs. 3.9b, 3.10b). The diabatic terms in both cases are positive, whereas the advection terms are negative, meaning that the diabatic term plays a major role in increasing the amount of marine fog compared with the advection term. In other words, the increase in Q_c of marine fog is mainly controlled by local cloud microphysical processes rather than directly by the advection of Q_c. The increase in the marine fog formation near the sea surface by the cloud microphysical processes may alter the condensation process due to the decreasing saturated water vapor pressure and less turbulent mixing induced by low air-temperature and SST anomalies (Figs. 3.9d, 3.10d, Bretherton et al. 2013).

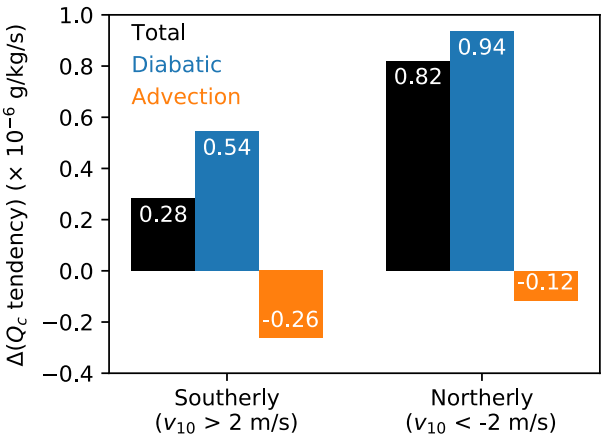

Figure 3.11. Difference between the Q_c budget terms on the northern flank near sea surface ($0 < x < 300$ km, $0 < z < 0.5$ km) in the CTL and SMO experiments with a northerly (left) or southerly (right) across the front. "Total" is overall change in Q_c, "Diabatic" is the change in Q_c in the microphysical scheme, and "Advection" is the change in Q_c caused by horizontal and vertical advection. Unit: $\times 10^{-6}$ g/kg/s.

ii. Roles of horizontal temperature advection in modulating marine fog around the front

Cold air-temperature anomaly near sea surface on the northern flank is one of key parameters to enhance the marine fog formation (i.e. positive ΔQ_c) through decreasing saturated water vapor pressure. Local SST anomaly can induce the cold air-temperature anomaly just above it by less heating from the sea surface. Additionally, the cooling process is significantly modulated by other factors, such as the horizontal advection, vertical advection, diabatic cooling with an updraft, and radiative cooling. As in the previous subsection, ΔQ_c of the marine fog and ΔRH near the sea surface depend on the meridional wind direction across the front. Thus, we hypothesize that the meridional wind across the front is also important for modulating the air-temperature anomaly via air-mass advection across the front, in addition to the direct heating or cooling by the SST anomaly. To test the hypothesis, we investigated the dependences of ΔQ_c and ΔRH on the meridional wind across the front by composite analysis in greater detail based on the v_{10} across the front. Figure 3.12 shows the meridional distribution of the vertical mean Q_c in the marine fog region ($0 < z < 0.5$ km) and its response to the SST front as a function of v_{10} over the SST front position. The meridional distribution of Q_c is calculated by the composite mean in a certain wind speed bin (bin size of v_{10} is 1 m/s) from -3 to +6 m/s. A large Q_c and positive ΔQ_c appear on the cold (northern) flank of the SST front ($y > 0$ km) for both northerly and southerly cases (Fig. 3.12a, b). However, near the SST front position ($-100 < y < 100$ km), ΔQ_c changes from positive to negative as the meridional wind direction changes from northerly to southerly. On the southern flank, mean Q_c is less than that on the northern flank and ΔQ_c is negative or almost zero, which is consistent with previous composite analysis results (Fig. 3.8). The results suggest that ΔQ_c of the marine fog near the SST front depends on the meridional wind across the front, and thus ΔQ_c on the northern flank with southerly is smaller than that with northerly.

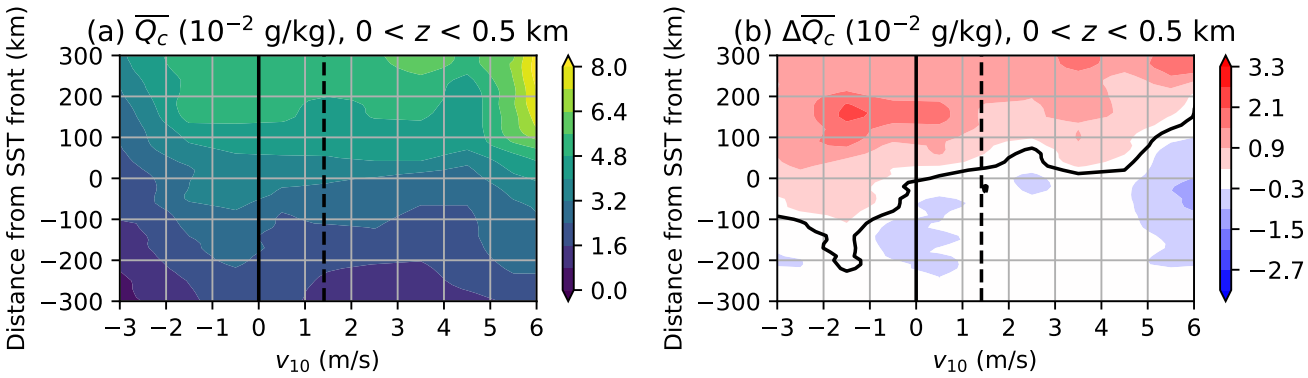

Figure 3.12. Dependence of **(a)** mean meridional distribution of Q_c and **(b)** ΔQ_c between two experiments at heights of 0–0.5 km with a meridional wind at 10 m (v_{10}) across the IJ2 front. *x*-axis is v_{10} and *y*-axis is distance from the position of the IJ2 SST front. Negative (positive) v_{10} indicates the northerly (southerly) wind. Mean meridional Q_c distribution is calculated for a certain wind speed with a bin size of v_{10} of 1 m/s. Vertical solid and dashed lines indicate a meridional wind speed of 0 and the period median wind speed (v_{10} = 1.41 m/s).

Figure 13 shows the dependence of the meridional distribution of ΔRH on v_{10} across the front, showing that positive ΔQ_c and ΔRH correspond well (Figs. 3.12b, 3.13a) and ΔRH is mainly controlled by the temperature anomaly (Figs. 3.13b vs 3.13c). In the CTL experiment, Q_c of marine fog increases with an increase in warm advection with moist air over cold SSTs on the northern flank of the SST front (Fig. 3.12a), which is consistent with the climatological explanation for the evolution of marine fog (Koshiro & Shiotani, 2014; Norris & Klein, 2000). However, the response of marine fog Q_c to the SST front is not explained by the mechanism described above; positive ΔQ_c of marine fog on the northern flank is suppressed by an increase in southerly wind speed (positive $v_{10} > 0$; increased warm advection), especially near the SST front (-100 km < y < 100 km). As mentioned before, the formation of marine fog is strongly related to the increased local cloud formation rate via microphysical processes (Fig. 3.11). For the enhanced formation of the marine fog, RH is an important factor in the condensation of cloud liquid water, and positive ΔRH near the sea surface is amplified by decreasing saturated water vapor pressure due to the low air-temperature anomaly with low SST (Fig. 3.9b, d). In addition to the local cooling by the SST, the low temperature anomaly is also modulated by warm (cold) advection brought by southerly (northerly) across the front (Fig. 3.13b). Therefore, the competition between the local cooling effect by SST and warm (cold) advection is crucial in modulating ΔQ_c and ΔRH on the northern flank when the southerly (northerly) case.

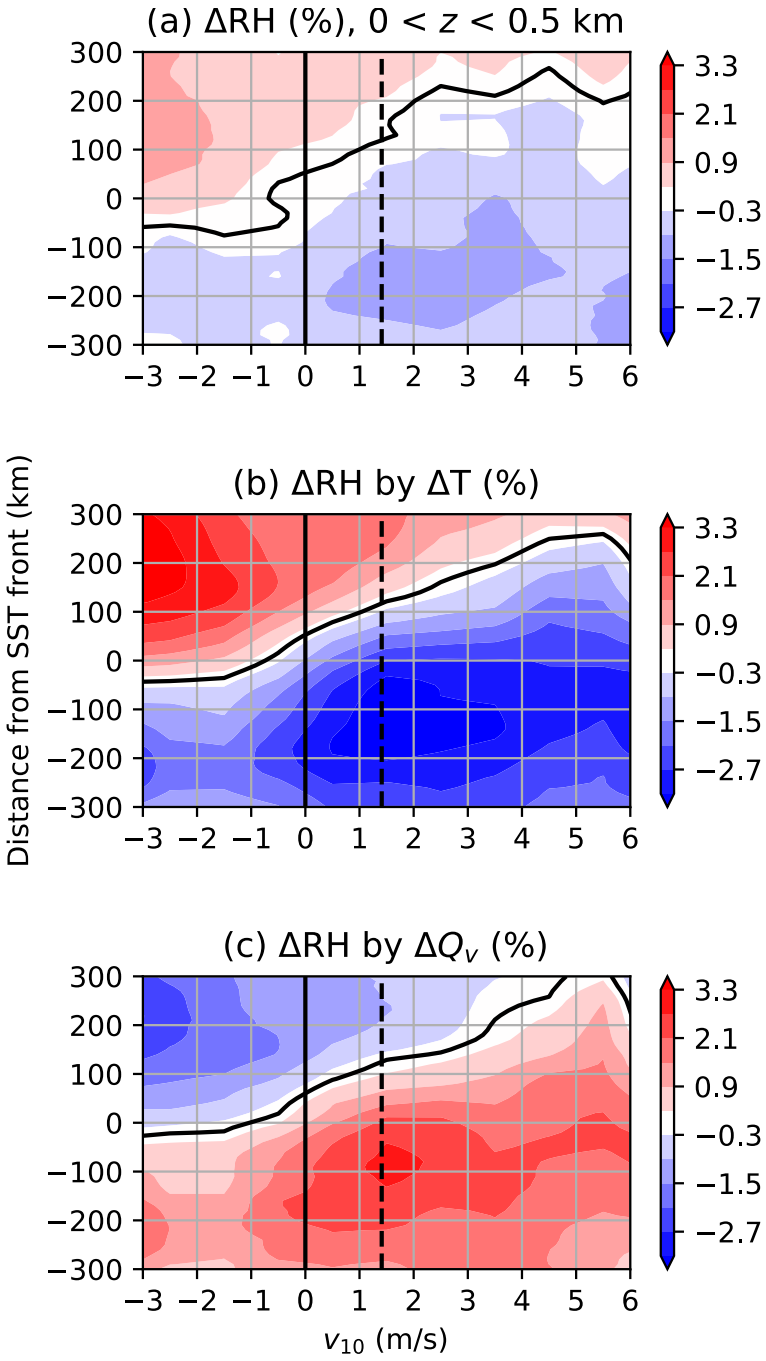

Figure 3.13. Same as Fig. 3.12b, but for **(a)** vertical mean RH difference at heights of 0–0.5 km, relative contribution to the RH difference by **(b)** temperature and **(c)** specific humidity. Unit: %.

Finally, we conducted temperature budget analysis to further investigate how the cooling and warming processes within the marine fog region are modulated by the presence of the SST front. Thus, we calculated the difference in each budget term between CTL and SMO experiments. Similar to the budget of cloud water mixing ratio, a tendency of the potential temperature in the WRF simulation is calculated as follows (Skamarock et al., 2008)

$$\frac{\partial \Theta}{\partial t} + (\nabla \cdot V\theta) = F_{\Theta} \quad (3.2),$$

where Θ is the coupled variables of θ, F_{Θ} is the diabatic terms arising from the physical schemes. Figure 3.14 shows the period-mean difference of each term of the temperature budget in the marine fog region on the northern flank of the SST front and its dependence on the meridional wind across the front; horizontal and vertical advection term (ADV) and the diabatic terms from the PBL, cumulus parameterization, cloud microphysical, and radiation schemes (referred to as PBL, CU, MPHYS, RAD, respectively). Note that meridional advection is a dominant term in ADV term rather than zonal and vertical advection. Positive anomaly of the total temperature tendency appears when the southerly case ($v_{10} > 0$) and vice versa when northerly case ($v_{10} < 0$), which is mainly controlled by ADV term. It suggests that southerly wind with warm advection is a dominant factor to modulate the positive temperature anomaly in the marine fog region in the CTL experiment (i.e. SST frontal effect), which suppresses the marine fog formation. The advection is enhanced by the strengthen of the horizontal gradient of air-temperature due to the SST front presence. In contrast, PBL term enhanced by the SST front is opposite to the ADV term. Negative anomaly of PBL term indicates the cooling for the marine fog region by local SST and enhances the marine fog formation (i.e. SST anomaly effect). In addition, ADV term is more sensitive to v_{10} than PBL term, indicating that the dependence of the marine fog response to the SST front on v_{10} is mainly modulated by the SST frontal effect. The results indicate the importance of both the local cooling process from the sea surface and the horizontal temperature advection process enhanced for modulating the synoptic variability of the maritime fog in summertime around the SST front.

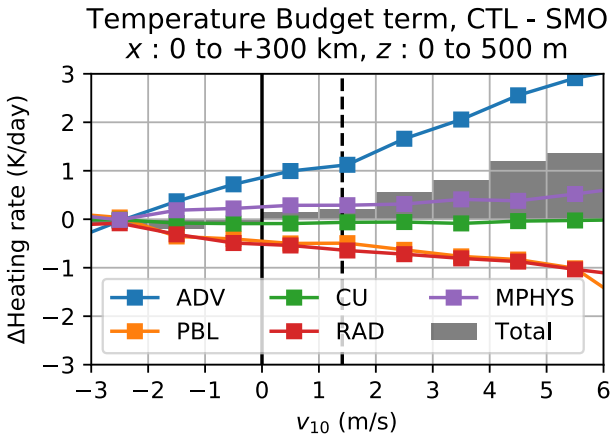

Figure 3.14. Difference in each term of the temperature budget at heights of 0–0.5 km on the northern flank of the SST front (0 to +300 km) between the CTL and SMO experiments as a function of meridional wind at 10 m (v_{10}) across the IJ2 front. x-axis is v_{10}. Mean heating rate is calculated in each bin of v_{10} with the bin size of v_{10} of 1 m/s. Vertical solid and dashed lines are a meridional wind speed of 0 and the period median wind speed (v_{10} = 1.41 m/s).

3.4 Discussion and Summary

We revealed the active role of the SST front in the Oyashio Extension in modulating low-level cloud properties during summertime based on WRF numerical simulations. We conducted two experiments with different SST boundary conditions; the one with 0.25° daily SST data from July to August 2016 and the other with spatially smoothed SST which does not have the SST frontal characteristics in the same period. Marine fog and St-Sc clouds frequently appear around the Oyashio Extension SST front in summertime, and they are significantly modulated by the SST front. Marine fog is more sensitive than St-Sc to the presence of the SST front; there are positive Q_c and CF anomalies on the northern flank of the SST front with a local negative SST anomaly. Two competing physical processes modulate the marine fog properties and their response to the SST front. First, a local negative SST anomaly on the northern flank can modulate the positive RH anomaly caused by the decreasing saturated water vapor pressure near the sea surface, which is favorable for forming marine fog. On the other hand, a local positive SST anomaly on the southern flank suppresses the marine fog formation. We called this local effect the SST anomaly effect, which is traditionally know (Bretherton et al., 2013; Norris & Leovy, 1994). Second, horizontal warm temperature advection from the warm to cold flanks (i.e. southern to northern flanks) near the sea surface, which is strengthened by the horizontal gradient of air temperature due to the SST front presence, can suppress the marine fog formation on the northern flank. The effect of warm advection on the northern flank is the opposite of that of the SST anomaly effect. We called this advective effect the SST frontal effect. The advective effect depends on not only the meridional gradient of the air temperature but also the meridional wind across the front, and thus the magnitude of the effect is controlled by cross frontal wind associated with the synoptic disturbances.

These results suggest that the SST front in the Oyashio Extension can modulate not only the mean-state but also the synoptic variability of the marine fog. We concluded that the overall effect of the SST front on low-level cloud is determined by the local SST anomalies, meridional wind across the front position, and the horizontal gradient of SST anomalies.

In the present chapter, we focused on only the response of low-level cloud properties to the SST frontal characteristics. However, low-level cloud has a strong cooling effect on the sea surface due to its high albedo and warm cloud top temperature (Hartmann & Short, 1980), implying the positive feedback loop between low-level cloud and SST (Norris & Leovy, 1994). The WRF numerical simulation shows that the increases (decreases) in Q_c and CF of marine fog are caused by decreases (increases) in the SST anomaly on the northern (southern) flank of the SST front. Thus, there is likely to be positive feedback between SST frontal characteristics and marine fog distribution. The SST front should be strengthened by the meridional distribution of the responses of the marine fog amount, once the SST front is strengthened by oceanic dynamics on a longer timescale than synoptic timescale we focused on. However, the overall responses of Q_c for St-Sc and LWP for low-level cloud do not correspond to the SST anomalies in the front, compared with the response of the marine fog properties. Therefore, we can expect that the total cloud radiative effect around the SST front does not have clear meridional contrast and there is weak positive feedback between low-level cloud and the SST front strength.

Generally, SST frontal characteristics related to the variability of the Kuroshio and Oyashio Extensions are modulated by oceanic subsurface variability, such as the current path and current speed (Isoguchi et al., 2006; Qiu et al., 2017), which have dominant timescales of their variabilities that are interannual or decadal. Therefore, our results imply the decadal modulation of the synoptic variability of low-level cloud by SST front properties in the mid-latitudes. It is also possible to obtain observational evidence of our WRF simulation results from long-term records of SST front properties. To understand air-sea (cloud-SST) coupling in the mid-latitude ocean in terms of the interactions across different timescales, we should investigate the detailed relationship between the synoptic variability of low-level cloud and the inter-annual variability of SST. In addition, the results from the present chapter about the active role of the ocean will be used in climate projection studies and model evaluations for atmospheric boundary layer and cloud properties within it in the summertime mid-latitudes.

Appendix 3A: Sensitivity of low-level cloud properties to PBL schemes

MYNN level-3 scheme was used as the PBL scheme in the present chapter. Here we described the sensitivity of low-level cloud properties to different PBL schemes for detail and showed the results of period-mean LWP with MYJ and YSU scheme under the same condition for other physical schemes, respectively (Fig. 3.A.1). They showed that LWPs with MYJ and YSU scheme have significantly large positive biases compared with MODIS observation (Fig. 3.A.1 b, d) in the northern flank of SST front where marine fog frequently appears. While the MYNN level-3 scheme tends to overestimate LWP in the same region, the biases in MYJ and YSU schemes are larger (compared with Fig. 3.3b, c). Additionally, too many marine fogs appear near sea surface in the southern flank of SST front where dominant type of cloud is St and Sc (not shown). The critical difference between the MYNN level-3 and MYJ/YSU schemes might be derived from expressions of stability and mixing length scale. Because the mixing length scale in the MYNN level-3 scheme was based on the results of large eddy simulations rather than on observations (Cohen et al., 2015), the scheme can reproduce well statistically stable boundary layer and radiation fog development (Nakanishi & Niino, 2006). That is why MYNN level-3 scheme can depict the marine fog properties within the stable boundary layer in the northern flank of OE SST front relatively well and we choose it as the PBL scheme in the present chapter.

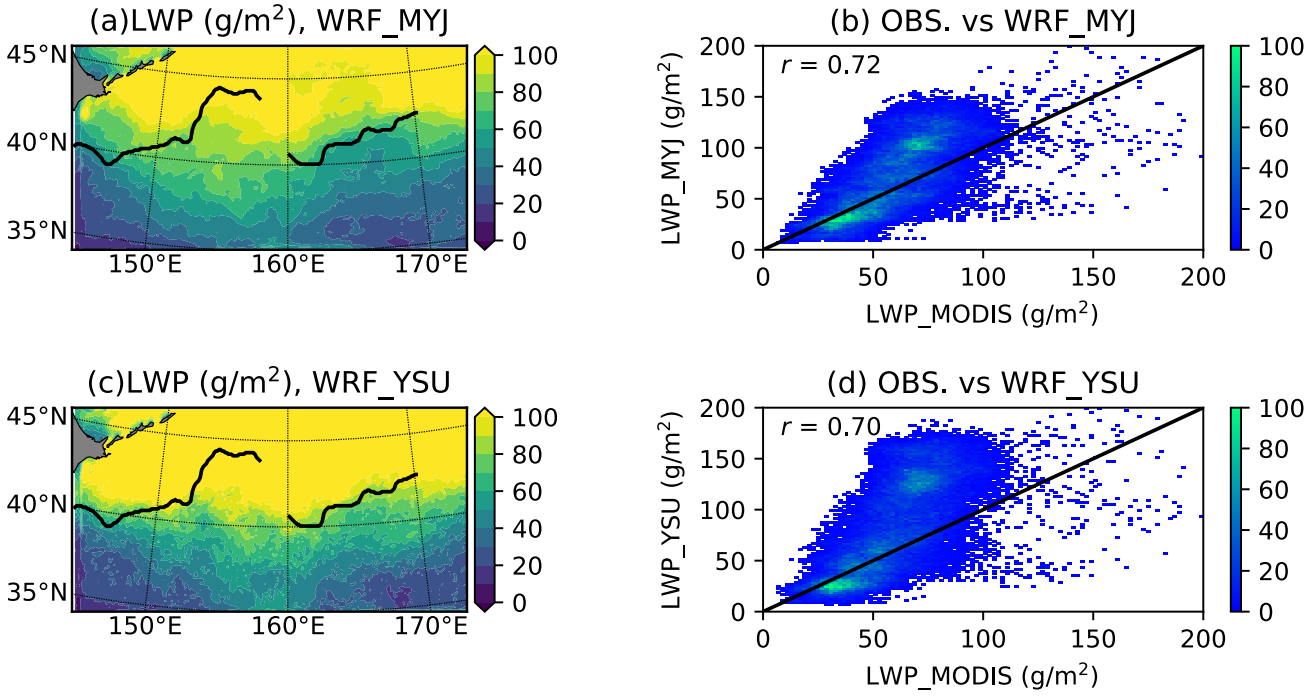

Fig. 3.A.1 Same as Fig. 3.3b, c, but for **a, b** and **c, d** for MYJ scheme and YSU scheme, respectively.

Chapter 4

Observed Low-Level Cloud Response to Inter-Annual Variation of the Strength of Oyashio Extension SST Front in Summertime

4.1 Introduction

Marine boundary layer (MBL) clouds (e.g., fog, stratus, and stratocumulus) interact strongly with sea surface temperature (SST) via two-way physical processes between them. MBL clouds tend to occur near the sea surface in the lower troposphere, whose top height is generally lower than 3 km in altitude, and are referred to as low-level clouds. Due to their high albedo and warm cloud top temperature, they reflect large amounts of shortwave (SW) radiation from the sun back to space, and therefore have a strong cooling effect on the surface of the land and ocean (Hartmann and Short 1980). On the other hand, low-level cloud properties are modulated by SST anomalies through marine atmospheric boundary layer processes. For example, low-level cloud cover (LCC) increases with decreasing SST due to the suppression of the entrainment of dry air from the free troposphere in the boundary layer (Bretherton et al. 2013; Qu et al. 2015; Kawai et al. 2017). Thus, more humidity can be trapped within the boundary layer if this entrainment is weakened, and LCC increases with decreasing SST itself. As a result, a positive feedback loop exists between variations in both LCC and SST in the North Pacific (NP), especially in summertime (Norris and Leovy 1994).

In the boreal summer (June, July, and August [JJA]) climatology, the LCC and cloud optical thickness (COT) are large over the NP poleward from 40°N and over the south-east of the NP near the Californian coast where the SST is low (contours in Fig. 4.1a, shaded area and contours in Fig. 4.1b) due to the positive feedback loop described above. In particular, LCC and COT in the NP drastically increase poleward of the SST frontal region around 40°N where the horizontal gradient of SST (∇SST) is larger than 1 °C/100 km (shaded area in Fig. 4.1a). Although a clear correlation has been observed between low-level cloud properties and SST on inter-annual timescales (e.g., Norris and Leovy 1994), their causal relationship is still under debate; this is due to the complex processes in low-level cloud

evolution, timescale dependences of the variabilities of both low-level cloud and SST (i.e., synoptic, intra-seasonal, and inter-annual), and the difficulty in distinguishing the two-way process within the LCC–SST feedback loop based on casual observational data analysis.

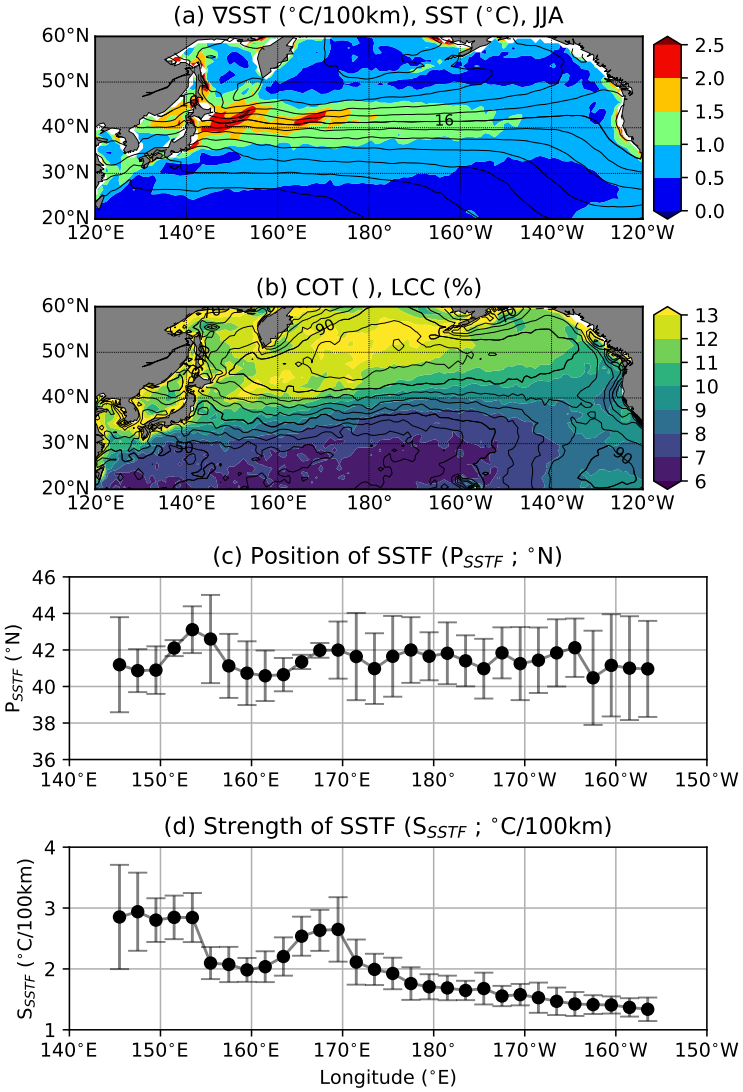

Fig. 4.1. Selected climatological conditions in the North Pacific in summertime (June, July, and August [JJA]) from 2003 to 2016. **(a)** Sea surface temperature (SST; contours, unit: °C, contour interval [CI]: 2K) and its horizontal gradient (∇SST; colored areas, unit: °C/100 km) from the optimum interpolation sea surface temperature. **(b)** Cloud optical thickness (COT) of low-level cloud (colored areas, unit: none) and low-level cloud cover (LCC) from a Moderate Resolution Imaging Spectroradiometer (contours, unit: %, CI: 5%). Climatological SST front properties in JJA: **(c)** position of the SST front (P_{SSTF}, unit: °N) and **(d)** strength of the SST front (S_{SSTF}, unit: °C/100 km). Error bars in **(c)** and **(d)** indicate the inter-annual variability.

Previous studies have generally found that the mid-latitude ocean plays a passive role in the air-sea interaction process, meaning that SST tends to be forced by the atmospheric variability. In particular, in the summertime mid-latitudes, the mixed-layer depth is so shallow that the SST is strongly forced by surface heat flux variability (e.g., Tanimoto et al. 2003, Cronin et al. 2013). Although the studies generally recognize the passive role of the ocean, more recent studies have revealed the active role of the ocean around the western boundary current regions (i.e., the Kuroshio Extension and Gulf Stream), meaning that SST can force the atmospheric variability, based on the analysis of high-resolution satellite data and coupled ocean–atmosphere models (e.g., Kwon et al. 2010). For example, the characteristics of oceanic fronts, especially in wintertime, have substantial effects on the overlying atmospheric storm tracks, the sea-level pressure field, and the vertical structure of convective cloud (Nakamura et al. 2008, Tokinaga et al. 2009, Tanimoto et al. 2009), providing critical baroclinicity or meridional contrast of the atmospheric boundary layer and anchoring the path of storm track activity. Most studies have focused on wintertime, but some have investigated the summertime imprint of the SST front on the atmospheric boundary layer (Tanimoto et al. 2009; Tokinaga et al. 2009; Kawai et al. 2015) and large-scale circulation (Frankignoul et al. 2011; Okajima et al. 2014). Tokinaga et al. (2009) showed seasonal differences in the impact of the Kuroshio Extension on the vertical development of clouds using both satellite observations from the International Satellite Cloud Climatology Project and ship-based measurements as a climatological mean, revealing the enhancement of marine fog over the cold flank of the Kuroshio Extension SST front. Kawai et al. (2015) conducted concurrent in situ observations around the Kuroshio Extension regions using three research vessels, showing a higher base of low-level cloud in the southern flank of the SST front due to strong turbulent mixing over the warmer water. However, they only focused on the mean state of the summertime cloud properties, paying much less attention to their inter-annual variability (Kwon et al. 2010; Frankignoul et al. 2011; Smirnov et al. 2015). Oceanic dynamics have the potential to drive both the climatological mean state and the inter-annual variation of low-level clouds in summertime through ocean-induced SST anomalies. Recently, Hosoda et al. (2016) investigated the inter-annual variation of the summertime oceanic subsurface temperature in the western, central, and eastern NP based on Argo float observations. They observed a large temperature variability both in the near-surface and in the subsurface up to 600 m depth in the western NP, that is affected by western boundary currents (i.e., the Kuroshio and Oyashio Currents). The findings of Hosoda et al. (2016) also imply the importance of oceanic dynamics for summertime SST despite the strong atmospheric forcing: this motivates us to investigate not only SST but also subsurface oceanic temperature simultaneously in order to reveal the active role of the ocean. We hypothesized that inter-annual variation of SST and the SST front (SSTF) driven by oceanic dynamics has an impact on the local properties of low-level cloud despite the strong summertime atmospheric forcing in the western NP.

There are two challenges that must be overcome to reveal the impact of oceanic dynamics on

the summertime marine boundary layer and low-level cloud based on observational data analysis. First, the oceanic forcing to SST is hard to retrieve because the summertime SST is highly sensitive to surface heat flux due to the shallow mixed-layer depth. In this chapter, to consider oceanic dynamics associated with the western boundary currents, the vertical structure of subsurface temperature determined by Argo float observations was used to diagnose the variability in the Kuroshio or Oyashio Extension. Additionally, we focused on the "frontal" characteristics of SST because the SSTF is a prominent structure that is mainly formed by the western boundary currents (i.e. the oceanic dynamics). For example, the SSTF in the western NP is formed in the confluence region of the Kuroshio and Oyashio Extensions (Nakamura and Kazmin 2003; Kazmin 2016). Second, low-level cloud properties are driven not only by SST but also other meteorological factors, such as estimated inversion strength (EIS), horizontal air-temperature advection (T_{adv}), and subsidence at the cloud top (e.g., Klein et al. 2017). Previous studies investigated the contribution from the various controlling factors listed above to assess the response of low-level cloud to global warming (Qu et al. 2015; Zhai et al. 2015; Myers and Norris 2016; Brient and Schneider 2016; Terai et al. 2016; McCoy et al. 2017; Miyamoto et al. 2018). The scientific consensus is that the formation of a large amount of low-level cloud is favored by strong temperature inversions at the top of cloud (Wood and Bretherton 2006), cool SST (Norris and Leovy 1994; Bretherton et al. 2013), weak subsidence (Myers and Norris 2013), and enhanced cold-air advection near the sea surface (Norris and Iacobellis 2005). In particular, the contributions of the inversion strength and SST to the variability of LCC caused by global warming are dominant cloud-controlling factors (Myers and Norris 2016), suggesting that the properties of oceanic low-level cloud are closely linked with sea surface conditions and the stability of the atmospheric boundary layer. Thus, in the present chapter, we attempted to quantify the contributions of different controlling factors separately using the multi-linear regression analysis method that was employed in the studies referenced above. The objective of the present chapter was to reveal the impact of the inter-annual variation of summertime SSTF properties on low-level cloud properties—that is, the response of low-level cloud properties to the strength of the SSTF—based on an observational dataset.

This chapter is organized as follows. In Section 4.2, the observational datasets and methods that were used to investigate the properties of the SSTF are described. The properties of the SSTF are also defined. In Section 4.3, we describe the inter-annual variation of the strength of the SSTF and related variability in ocean subsurface temperature (T_{sub}) in the western NP, suggesting that variation in the SSTF is driven by oceanic dynamics. Section 4.4 describes our investigation into the response of low-level cloud properties to the inter-annual variation of the SSTF. We quantify the contribution of SST to the modulation of low-level cloud properties compared with other controlling factors for low-level cloud using a multi-linear regression model. Section 4.5 summarizes and discusses our findings.

4.2 Data and Methods

4.2.1 Data

In this chapter, we used monthly mean datasets of low-level cloud properties, surface heat flux, ocean subsurface temperature, and meteorological parameters to investigate the impact of the ocean-driven SSTF around the Oyashio Extension on low-level clouds on inter-annual timescales. The period from 2003 to 2016 was analyzed because of the availability of the datasets. All variables were spatially interpolated into the coarsest common grid of 1° for the low-level cloud products. Details of each observational dataset are described below.

i. Cloud properties and surface heat flux

To estimate the LCC and the COT of low-level cloud, we used the L3 gridded cloud product (MYD08 M3) from the latest Moderate Resolution Imaging Spectroradiometer (MODIS) release (version 6) from the MODIS instruments on board the Aqua satellite platforms (Platnick 2015) with a horizontal resolution of 1°. Due to the difficulty in estimating the true LCC from passive sensors, the cloud cover was calculated under the random overlapping assumption. Comparison of the cloud cover obtained from the radar and lidar observations with active sensors indicated that the random overlap assumption was reasonable over the mid-latitude oceanic regions compared with other assumptions (Li et al. 2015). Thus, the true LCC was estimated as follows:

$$LCC\ [\,\%\,] = \frac{f_L}{1 - f_M - f_H}, \tag{4.1}$$

where f_L, f_M, and f_H are the fractions of the scene covered by low-level (680 hPa ≤ cloud top pressure [CTP] < 1000 hPa), mid-level (440 hPa ≤ CTP < 680 hPa), and high-level (CTP < 440 hPa) cloud types, respectively. The cloud cover of each of these types was calculated using the histogram of CTP at each grid point within 1 month. Additionally, the COT for low-level cloud was calculated using the CTP-COT histograms in each grid with a criterion that CTP is greater than 680 hPa, which is the "conditional-mean" COT of low-level cloud.

Two observational heat flux datasets (SW radiation, longwave [LW] radiation, sensible heat [SH], and latent heat [LH]) at sea surface were used in this chapter. To estimate monthly mean radiative fluxes (SW and LW), we used the Clouds and the Earth's Radiant Energy System (CERES) Energy Balanced and Filled (EBAF) product Edition 4.0 (Kato et al. 2018). The variables were calculated using a radiative transfer model initialized using satellite-based cloud and aerosol data and meteorological assimilation data obtained from reanalysis. The variables were also constrained by the observed top-of-atmosphere radiative fluxes. The CERES product was also used to obtain the cloud radiative effect (CRE) for SW and LW at the top-of-atmosphere and sea surface, which is defined as

the difference between the all-sky radiative flux and clear-sky radiative flux using the radiative transfer model. In the following analysis, we analyzed the SWCRE as one of low-level cloud properties because SWCRE variability depends on the LCC and COT of low-level cloud rather than those of high-level cloud (not shown). The results for LWCRE are also not shown here because its response and variability are smaller than those of SWCRE by one order of magnitude. Global ocean-surface heat flux products were obtained from the monthly mean turbulent fluxes dataset of the Objectively Analyzed air-sea Heat Fluxes (OAFlux) project of the Woods Hole Oceanographic Institution (Yu et al. 2008). The OAFlux products are constructed not from a single data source, but from an optimal blending of satellite retrievals and three atmospheric reanalysis datasets. The horizontal resolutions of the CERES and OAFlux products are 1° in longitude and latitude.

ii. Oceanic properties

The objectively analyzed monthly mean SST of the National Oceanic and Atmospheric Administration (NOAA) Optimum Interpolation version 2 (OISST; Reynolds et al. 2002) was used as the SST dataset. Monthly mean SST was calculated by averaging from the interpolated daily dataset with a horizontal resolution of 0.25°. To assess the interannual variability of oceanic subsurface structures associated with the strength of the SST front, we used a monthly mean three-dimensional temperature dataset based on Argo profiling float observations (Argo 2000). The Roemmich–Gilson (RG) Argo Climatology dataset provided by the Scripps Institution of Oceanography (Roemmich and Gilson 2009) was used. The horizontal resolution of the RG product is 1°, and the vertical resolution varies with depth (e.g., 25 m resolution from a depth of 10 to 200 m), and analysis was conducted using a two-dimensional optimal interpolation method on pressure surfaces for temperature and salinity. To calculate the mixed layer depth (MLD), we used the Monthly Isopycnal/Mixed-layer Ocean Climatology (MIMOC; Schmidtko et al. 2013) dataset estimated mostly by Argo float observation, supplemented by ship observations and conductivity-temperature-depth profile data.

iii. Meteorological properties

To estimate the variability of the meteorological field associated with the inter-annual variations of low-level cloud and SSTF, we used ERA-Interim reanalysis data (Dee et al. 2011) with a horizontal resolution of 0.75° and 37 vertical levels. Monthly mean data of air temperature at 700 and 1000 hPa, horizontal wind at 1000 hPa, and sea-level pressure were used to calculate the EIS and T_{adv} as a proxy for LCC controlling factors. EIS was calculated following the method of Wood and Bretherton (2006), showing the inversion strength at the top of planetary boundary layer given the air temperature at 700 hPa and at the sea surface. T_{adv} was calculated by:

$$T_{adv}[K/day] = -u_{1000\ hPa}\frac{\partial SST}{\partial x} - v_{1000\ hPa}\frac{\partial SST}{\partial y}, \quad (4.2)$$

where $u_{1000hPa}$ and $v_{1000hPa}$ are the zonal and meridional wind speeds at 1000 hPa, respectively. Instead of SST and wind at 1000 hPa, the temperature at 1000 hPa and wind at 10 m could be used, respectively. However, the computed temperature advections were not significantly different and did not depend on the variables used (Zelinka et al. 2018). Additionally, the vertical pressure velocity and relative humidity at 700 hPa (ω_{700} and RH_{700}, respectively) were also used to investigate whether these parameters are controlling factors for the low-level cloud properties.

4.2.2 Methods

The position of the SSTF (P_{SSTF}) was defined as the latitude where the horizontal gradient of the SST has a maximum value for each month and each longitude bin of 1° width. To extract the properties of the SSTF associated with the Oyashio Extension (Isoguchi et al. 2006), we searched for the P_{SSTF} in the latitude range of 35–45°N. The strength of the SST front (S_{SSTF}) was defined as the maximum horizontal gradient of the SST. Mathematically, S_{SSTF} can be expressed as:

$$S_{SSTF}(x,t)\ [\,℃/100\ km\,] = \left[\max\left(\nabla \mathrm{SST}\ (x,y,t)\right)\right]_{x,t}, \quad (4.3)$$

where x, y, and t are the longitude, latitude, and time, respectively; and $[\ ]_{x,t}$ denotes searching for the maximum value of the horizontal gradient of the SST for the longitude bin (x) and time (t). As an example, we plotted the climatological P_{SSTF} and S_{SSTF} in JJA (Fig. 4.1c and d).

To confirm that the SSTF properties, in particular S_{SSTF}, are determined by oceanic forcing rather than atmospheric forcing (i.e., the impact of SST/SSTF on the atmosphere), we investigated the frontogenesis/frontolysis process (i.e., strengthen/weaken in S_{SSTF}) in the western NP using the following frontogenesis equation (Tozuka and Cronin 2014; Ohishi et al. 2017; Tozuka et al. 2017):

$$\frac{\partial}{\partial t}\left(\frac{\partial \mathrm{SST}}{\partial y}\right) = \frac{\partial}{\partial y}\left(\frac{Q}{\rho_0 C_p H_{mix}}\right) + \frac{\partial}{\partial y}(oceanic), \quad (4.4)$$

where Q is the net sea-surface heat flux, ρ_0 is the typical sea water density, C_p is the specific heat at a constant pressure, H_{mix} is the MLD derived from the MIMOC dataset, *oceanic* is the SST tendency term derived from the oceanic dynamics (i.e., other than the surface heat flux term; horizontal advection, vertical mixing, etc.). The $\frac{\partial}{\partial y}(oceanic)$ term in Equation 4.4 is calculated as the residual of the equation. This equation was based on a simplified mixed-layer temperature budget (Moisan and Niiler 1998) and assumes that SST is equivalent to the temperature of the mixed layer. In the SSTF region in the western NP, the horizontal gradient of SST is dominated by the meridional component

rather than the zonal component. Thus, we only considered the meridional component of the SST gradient in Eq. 4.4, and investigated the variation of S_{SSTF} and the underlying physical process that modulate it using the above frontogenesis equation.

4.3 Mechanism of SSTF variations in the summertime western NP

4.3.1. Climatology of SSTF properties in summertime (JJA) from 2003 to 2016

Figures 4.1c and d show the climatological zonal distributions of P_{SSTF} and S_{SSTF} in the summertime (JJA) NP and their standard deviations (SD) of the inter-annual variability. The figure shows some zonal differences in SSTF properties between the parts to the west and east of 170°E, which are respectively called the western NP (WNP) and central NP (CNP) hereafter. The zonal differences in the climatological P_{SSTF} are found to be not as large as those for S_{SSTF}; however, the SD of the P_{SSTF} was much smaller in the WNP than in the CNP (Fig. 4.1c), implying the stable and unstable SSTF in the WNP and CNP, respectively. Second, the climatological S_{SSTF} is stronger in the WNP than in the CNP (i.e., 2–3°C/100 km in the WNP, < 2°C/100 km in the CNP; Fig. 4.1d). Additionally, there are two peaks for S_{SSTF} at around 150 and 170°E, respectively. These correspond to the Oyashio Extension SSTFs trapped by bottom topography, called the Isoguchi Jet (IJ) 1 and IJ2 regions (Isoguchi et al. 2006). Qiu et al. (2017) suggested that these SSTFs vary independently on decadal timescales, and other studies showed their close relationship with the variability of the Kuroshio Extension (e.g., Sugimoto et al. 2014), which is one of the strongest warm western boundary currents in the world and has a deep vertical structure with a thickness of about 600 m (Qiu 2001). Additionally, observational studies have examined the relative contributions of atmospheric forcing (i.e., surface heat flux) and oceanic forcing (i.e., subsurface temperature advection, vertical mixing across the base of mixed layer, etc.) to the SST tendency in summertime; for example, oceanic forcing has been shown to be dominant in the WNP (Wu and Kinter 2010; Hosoda et al. 2016). Figure 4.2 displays a longitude–depth cross-section of the SD of T_{sub} in JJA along the SST frontal region (35–45°N) estimated from the RG product. Here, the large temperature variability in the WNP reaches to a deeper depth of 400 m than that in the CNP of 100 m, suggesting that the oceanic forcing and the surface heat flux forcing are dominant cause of the temperature variability in the WNP and CNP, respectively (Hosoda et al. 2016). In this chapter, we set our target region in WNP as the IJ2 region from 160°E to 170°E because the summertime SSTF in this region is likely driven by oceanic dynamics rather than atmospheric forcing.

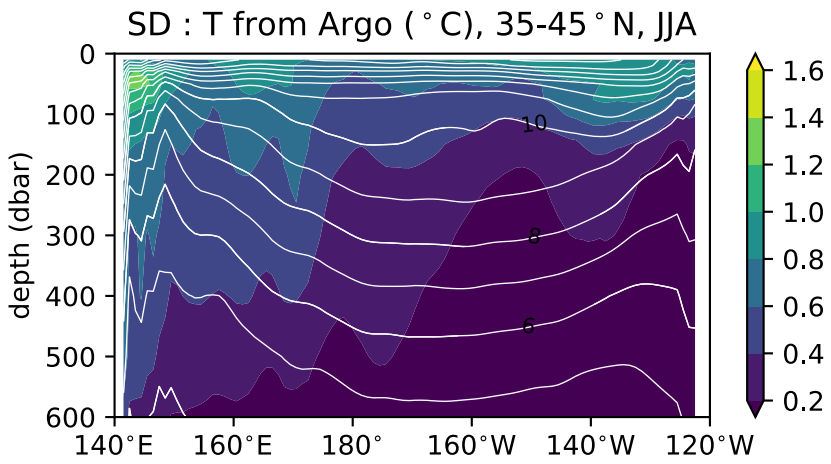

Fig. 4.2. The standard deviation (SD) of the inter-annual variation of subsurface temperature obtained from Argo observation at latitudes of 35–45°N for June, July, and August (JJA) in 2003–2016 (colored areas, unit: °C). The climatological mean of subsurface temperature is also plotted (contours, unit: °C, CI: 1°C).

4.3.2. Inter-annual variations of the SST fronts and subsurface temperature

The time series of the SSTF properties for all months and only JJA-mean state in the IJ2 region are shown in Figure 4.3. The inter-annual variation of the SSTF properties in the IJ2 region was relatively small (SD of P_{SSTF}: 0.57°N for all months and 0.41°N for JJA only), and cannot be resolved by the coarse grid of the low-level cloud dataset (i.e. horizontal resolution of 1°). The seasonal variation of P_{SSTF} was unclear. In contrast, S_{SSTF} in the IJ2 region had a clear seasonality and low-frequency variation; S_{SSTF} had minimum and maximum values in summertime and wintertime, respectively (not shown), consistent with the results of previous studies (Kazmin 2016; Tozuka et al. 2017 2018). Interestingly, clear inter-annual variation of S_{SSTF} was also observed in the summertime-mean state, e.g., a negative anomaly from 2005 to 2008 and a positive anomaly from 2009 to 2011 (Fig. 4.2b). This kind of low-frequency variation of the Oyashio Extension SSTF is possibly driven by oceanic forcing (Frankignoul et al. 2011; Sugimoto et al. 2014; Qiu et al. 2017). In the following analysis, we focus on only the inter-annual variation of S_{SSTF} and the local response of low-level cloud to this parameter, rather than the P_{SSTF}.

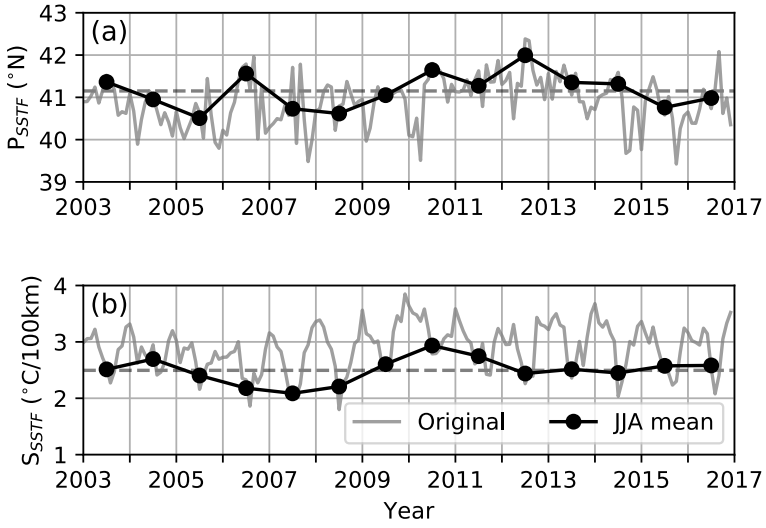

Fig. 4.3. Time series of mean **(a)** position of the sea surface temperature front (P_{SSTF}) and **(b)** strength of the sea surface temperature front (S_{SSTF}) in the Isoguchi Jet 2 region (160–170°E). Thin and thick lines indicate the original time series and June, July, and August (JJA)-mean values, respectively. Horizontal dashed lines show the climatological mean values of JJA-mean sea surface temperature front properties.

Figure 4.4 displays the regressions of SST and T_{sub} onto the summertime S_{SSTF} in the IJ2 region (160–170°E; Fig. 4.4a and c) and a part of the CNP (155–165°W; Fig. 4.4b and d), indicating the oceanic state at the sea surface and in the subsurface when S_{SSTF} is increased by one standard deviation (1σ=0.23°C/100 km). In Fig. 4.4, the x-axis is modified to relative latitude from the JJA-mean P_{SSTF} in each part of the SSTF region. As expected, the response of SST to the strengthen of S_{SSTF} (ΔSST) was positive (warmer) and negative (colder) in the southern and northern flank of the SSTF, respectively. Although the spatial patterns of ΔSST were similar in the IJ2 region and the CNP, the spatial patterns of the response to T_{sub} (ΔT_{sub}) were notably different in these two regions. In the IJ2 region, the meridional contrast of ΔT_{sub} across the position of SSTF was found both at the near sea surface and in the deeper part (Fig. 4.4c). Additionally, a warm ΔT_{sub} appeared from the sea surface to a depth of 600 m in the southern flank around –10° (Fig. 4.4c), corresponding to the warm ΔSST at the same latitude (Fig. 4.4a) and the relative position of Kuroshio Extension. In contrast, the significant meridional contrast of ΔT_{sub} in the CNP appears only near the sea surface (depth < 50 m), implying that changes in SST tend to be strongly controlled by the surface heat flux forcing (Hosoda et al. 2016). In other words, the meridional contrast of ΔT_{sub} in the deeper part of the IJ2 region presents the observational evidence for the ocean-induced SST and SSTF properties even in the summertime.

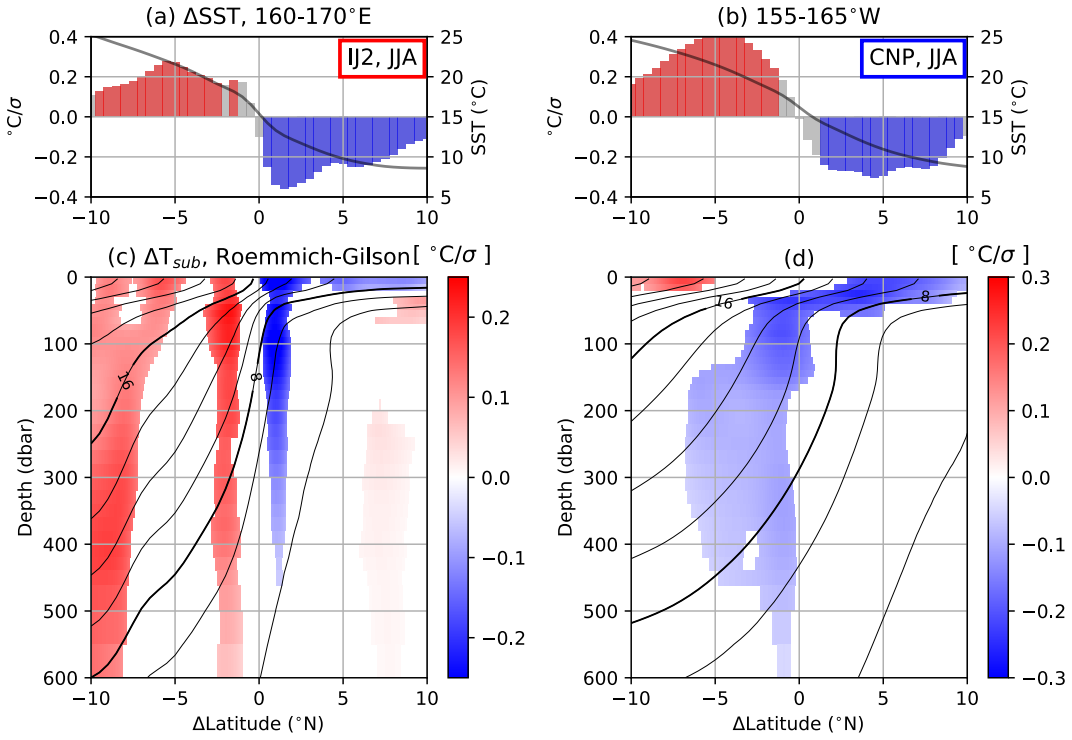

Fig. 4.4. (a) Meridional distribution of the response of the sea surface temperature (SST) to the increase of the strength of the sea surface temperature front by one standard deviation (bar corresponding with the left y-axis) and the climatological mean value of the SST (line corresponding with the right y-axis) in the Isoguchi Jet 2 region. The x-axis is the shifted latitude based on the position of the sea surface temperature front (P_{SSTF}). **(c)** Latitude–depth cross-section of the response of the subsurface temperature (T_{sub}) in the Isoguchi Jet 2 region obtained from the Roemmich–Gilson product of Argo float observation from 2004 to 2016. Responses within the 95% confidence interval are displayed in color. Contour lines are climatological values of subsurface temperature (CI: 2°C). **(b)** and **(d)** are the same as **(a)** and **(c)**, respectively, but for the central North Pacific (CNP; 155–165°W).

Figure 4.5 shows the spatial distribution of summertime ΔSST regressed onto S_{SSTF} of the IJ2 region. As shown in Fig. 4.4a, a warm (cold) ΔSST appears in the southern (northern) flank of the SSTF when S_{SSTF} is increased (Fig. 4.5). Additionally, the ΔSSTs spread widely away from the IJ2 region. For example, warm ΔSSTs appear from 140°E to 170°E, which is along the path of the Kuroshio Extension. On the other side, cold ΔSSTs appear in the northern flank of the IJ2 SSTF with a zonal expansion along the path of the Oyashio Extension. These spatial characteristics imply that the ΔSSTs and the strengthening process of S_{SSTF} in the summertime IJ2 region are closely related to the Kuroshio and Oyashio Extensions, respectively.

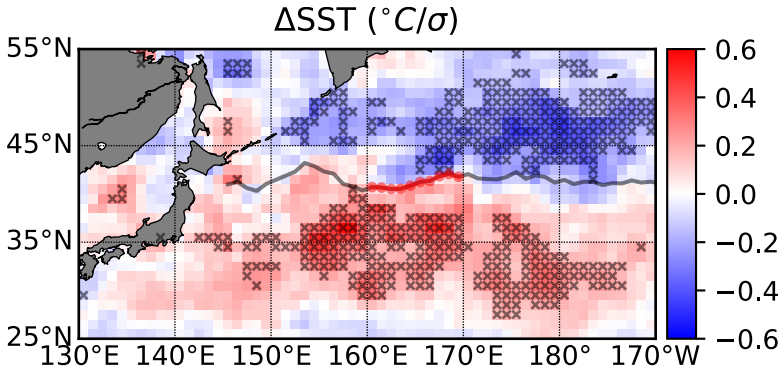

Fig. 4.5. The responses of the sea surface temperature (SST) (°C) at each grid point to the increased strength of the sea surface temperature front in the Isoguchi Jet 2 region (at 160–170°E) by one standard deviation. The black line (red points) shows the climatological mean position of the sea surface temperature front (in the Isoguchi Jet 2 region). Grid boxes with a black cross indicate responses within the 90% confidence interval.

4.3.3. Mechanisms of frontogenesis in the IJ2 region; atmospheric forcing vs oceanic forcing

We investigated how the properties of the summertime SSTF were determined based on the frontogenesis equation (Eq. 4.4). Figure 4.6 shows the seasonal evolution of each term in the frontogenesis equation from May to September. Note that, in Fig. 4.6, a positive (negative) rate indicates frontogenesis (frontolysis) and the meridional gradient of SST (∂SST/∂y) is always negative in the IJ2 region. As described above, S_{SSTF} in the IJ2 region is the smallest in summertime and strongest in wintertime (e.g., Tozuka et al. 2018). Frontolysis occurs in JJA due to the surface net heat flux (HF) term (red line), which weakens the S_{SSTF} (Fig. 4.6). In contrast, the oceanic term (OCN; blue line) always induces frontogenesis in the IJ2 region. The results shown in Fig. 4.6 imply that the HF term is a dominant factor modulating summertime frontolysis in the climatological seasonal cycle.

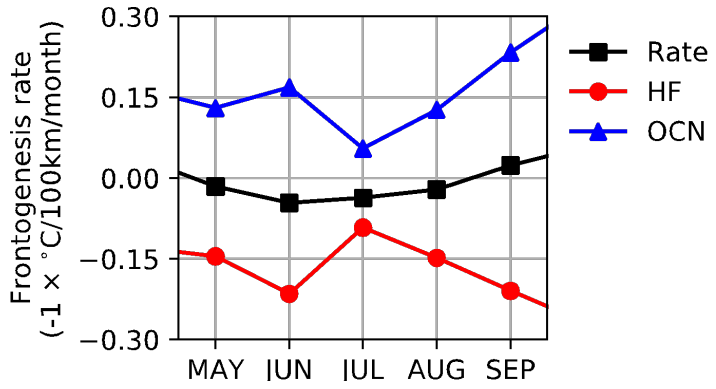

Fig. 4.6. The seasonal variation from May to September of each term of the frontogenesis equation in the Isoguchi Jet 2 region, calculated according to Tozuka et al. (2014). The surface heat flux term calculated based on the meridional gradient of net heat flux (HF; red line), the oceanic term (OCN; solid line), and the total frontogenesis rate (Rate; black line) are plotted. A positive (negative) value indicates frontogenesis (frontolysis), meaning that the strength of the sea surface temperature front is increased (decreased) by the frontogenesis (frontolysis) process in each month.

Figure 4.7a displays the mean meridional distribution of ∂SST/∂y and that of the mean meridional gradient of heat flux (∂Q/∂y) in the IJ2 region. The minimum ∂SST/∂y and maximum ∂Q/∂y occur close to the position of the SSTF. Note that a positive ∂Q/∂y means more heat release or less heat input in the south of SSTF as compared to that in the north; frontolysis process. To further investigate the relationship between the HF term and S_{SSTF} on inter-annual timescales, Fig. 4.7b displays a scatter plot of ∂SST/∂y vs ∂Q/∂y on the SSTF in JJA from 2003 to 2016, indicating the relationship between the strength of the SSTF (~∂SST/∂y) and the frontolysis by surface heat flux forcing (~∂Q/∂y) on inter-annual timescales. Note that the meridional gradient of MLD has a negligible effect on the frontolysis in summertime (not shown). A significant negative correlation can be seen between ∂SST/∂y and ∂Q/∂y, suggesting that more frontolysis (i.e., positive values of ∂Q/∂y) occurs when the SSTF is strengthened (i.e., negative values of ∂SST/∂y). This indicates that a frontolysis does not decrease S_{SSTF}, but that an increased S_{SSTF} induces more frontolysis by modulating the heat release from the sea surface, reflecting the active role of the ocean in the modulation of surface heat flux. The zonal distribution of the correlation coefficients in Fig. 4.8 is similar to that shown in Fig. 4.7b, and the correlation coefficients with each component of heat flux are also displayed. The correlation between ∂Q/∂y and ∂SST/∂y was significantly negative in both the IJ2 region and in the western part from the date line, where the climatological mean S_{SSTF} is greater than 1.5°C/100 km (Fig. 4.1a). Furthermore, the correlation coefficient between SH and LH is also significantly negative, indicating that S_{SSTF} is effectively damped by the turbulent flux due to the SST anomaly itself. Unlike the western part including the IJ2 region, there was no significant correlation between ∂Q/∂y and ∂SST/∂y in the CNP; the eastern part from the date line. The relationship between HF and SST (or ∂Q/∂y and ∂SST/∂y) that acts to damp the SST (SSTF) has been recognized as an active role in SST (Tanimoto et al. 2003),

which has been confirmed in the western part from the date line. Thus, we can assume that, in the IJ2 region, the inter-annual variation of S_{SSTF} is mainly driven by the oceanic forcing, rather than the heat flux forcing. Hereinafter, we regarded the regressions of low-level cloud properties onto S_{SSTF} as the impact of ocean-driven SST on the low-level cloud.

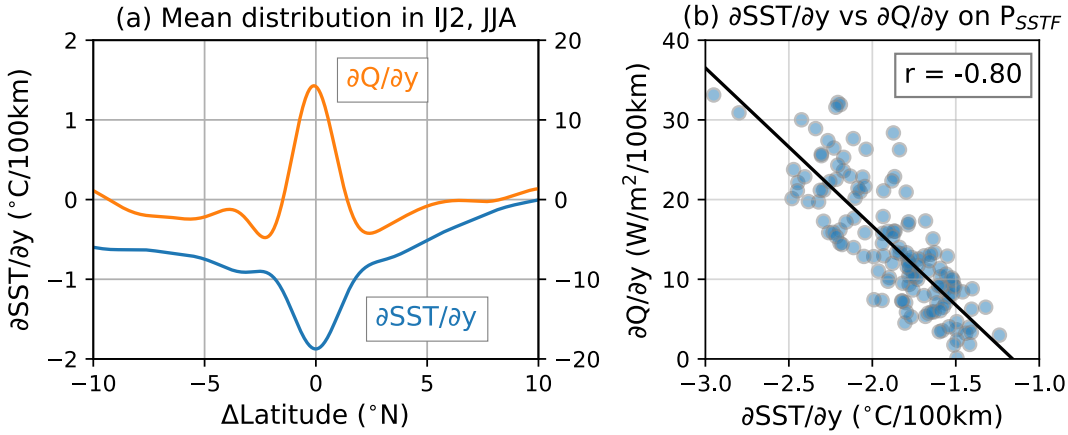

Fig. 4.7. **(a)** Mean meridional distribution of the meridional gradient of the sea surface temperature (∂SST/∂y; unit: °C/100 km; left y-axis) and that of net heat flux (∂Q/∂y; unit: W/m^2/100 km; right y-axis) close to the position of the sea surface temperature front (P_{SSTF}) in the Isoguchi Jet 2 (IJ2) region in June, July, and August (JJA). Downward heat flux is defined as positive; thus, a positive ∂Q/∂y indicates that a small heat input (or large heat release) occurs in the south of the IJ2 region, suggesting frontolysis. **(b)** Scatter plots of ∂SST/∂y vs ∂Q/∂y from 2003 to 2016 in JJA. The correlation coefficient between ∂SST/∂y and ∂Q/∂y is displayed in the upper right.

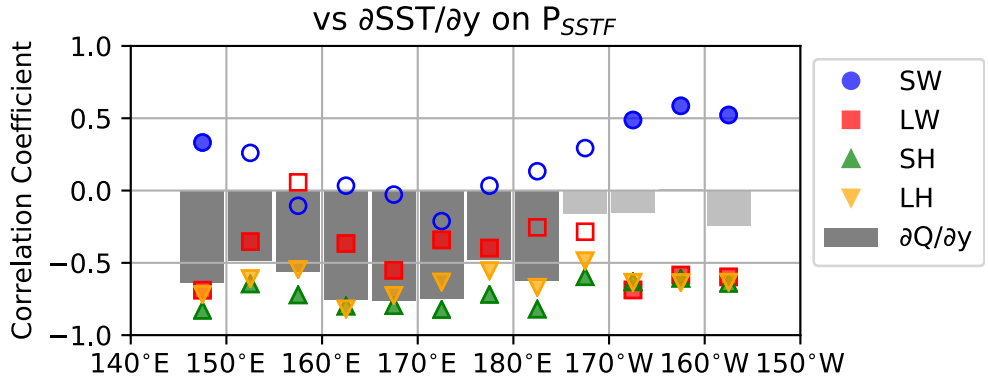

Fig. 4.8. Correlation coefficients between ∂SST/∂y and the meridional gradients of each flux term (shortwave [SW] radiation: blue, longwave [LW] radiation: red, sensible heat [SH]: green, and latent heat [LH]: orange) and the correlation coefficients between ∂SST/∂y and the meridional gradient of net heat flux (∂Q/∂y) (gray bars) close to the position of the sea surface temperature front (P_{SSTF}) in the Isoguchi Jet 2 region in June, July, and August (JJA). Correlation coefficients were calculated for every 5° longitudinal bin from 145°E eastward. For all colored markers and gray bars, the correlation coefficients are within the 99% confidence interval.

4.4 Response of summertime low-level cloud properties to S_{SSTF} in the IJ2 region

SST frontal characteristics (i.e., S_{SSTF} and P_{SSTF}) have been recognized as the ocean-induced factors modulating atmospheric conditions in the mid-latitudes, including the storm tracks (Nakamura et al. 2004; Ogawa et al. 2012) and vertical cloud distributions (Tanimoto et al. 2009; Tokinaga et al. 2009; Liu et al. 2014; Kawai et al. 2015). In the previous section, we confirmed that the inter-annual variation of the summertime S_{SSTF} in the IJ2 region is likely driven by oceanic forcing from the Kuroshio and Oyashio Extensions. In this section, we estimate the response of low-level cloud properties to the increased S_{SSTF} in the IJ2 region. To do this, we calculated the linear regression coefficient of each cloud variable and the controlling factor at every grid point to the inter-annual variation of the mean S_{SSTF} in the IJ2 region. We recorded the meridional distributions of the responses of low-level cloud properties (i.e., LCC, COT of low-level cloud, and SWCRE at the sea surface) to the S_{SSTF} index in JJA (Fig. 4.9). We found two distinct patterns in these responses, particularly for SWCRE, in the southern and northern flanks of the SSTF, respectively. In the southern flank, ΔSWCRE was positive over the warm ΔSST (Fig. 4.9a), mainly due to the negative ΔLCC (Fig. 4.9b). The regression of ΔCOT to S_{SSTF} in the southern flank was not significant (Fig. 4.9c). In the northern flank, ΔSWCRE was negative over the cold ΔSST (Fig. 4.9a), mainly due to the positive ΔCOT (Fig. 4.9c), rather than the ΔLCC. The opposite was apparent for the negative ΔLCC in the northern flank; however, the ΔLCC in this region showed lower statistical significance. Similar results are displayed in Fig. 4.10, except for their horizontal distributions. A common feature of all three low-level cloud properties is that the responses to S_{SSTF} appear in a wide region not confined to around the IJ2 region. This spatial feature is similar to the results for SST (Fig. 4.5) associated with the western boundary currents, that is, the paths of Kuroshio and Oyashio Extensions. The response of ΔLCC to ΔSST associated with the increased S_{SSTF} in the southern flank of the SSTF is similar to the observations of previous studies described in Section 4.1 (Norris and Leovy 1994; Norris et al. 1998; Bretherton et al. 2013). Similar to the response of LCC to SST, COT can also be modulated by changes in the entrainment process of dry air from the free troposphere into the boundary layer associated with an SST anomaly; COT increases with decreasing SST (Terai et al. 2016 2019), which is consistent with the positive ΔCOT in the northern flank of the SSTF observed in the present chapter (Figs. 4.9c and 4.10c).

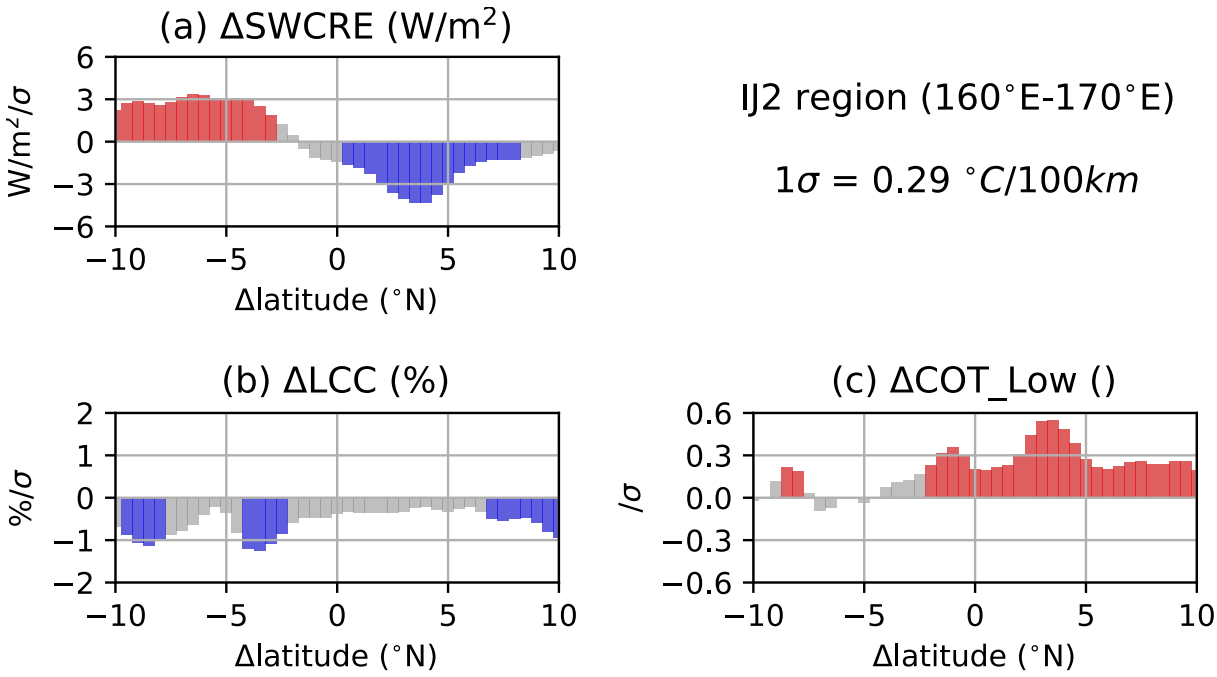

Fig. 4.9. As in Fig. 4.4 (a), but for **(a)** the shortwave cloud radiative effect (SWCRE) (unit: W/m^2), **(b)** cloud optical thickness (COT; unit: none), and **(c)** low-level cloud cover (LCC; unit: %). The standard deviation of the strength of the sea surface temperature front is shown in the upper right.

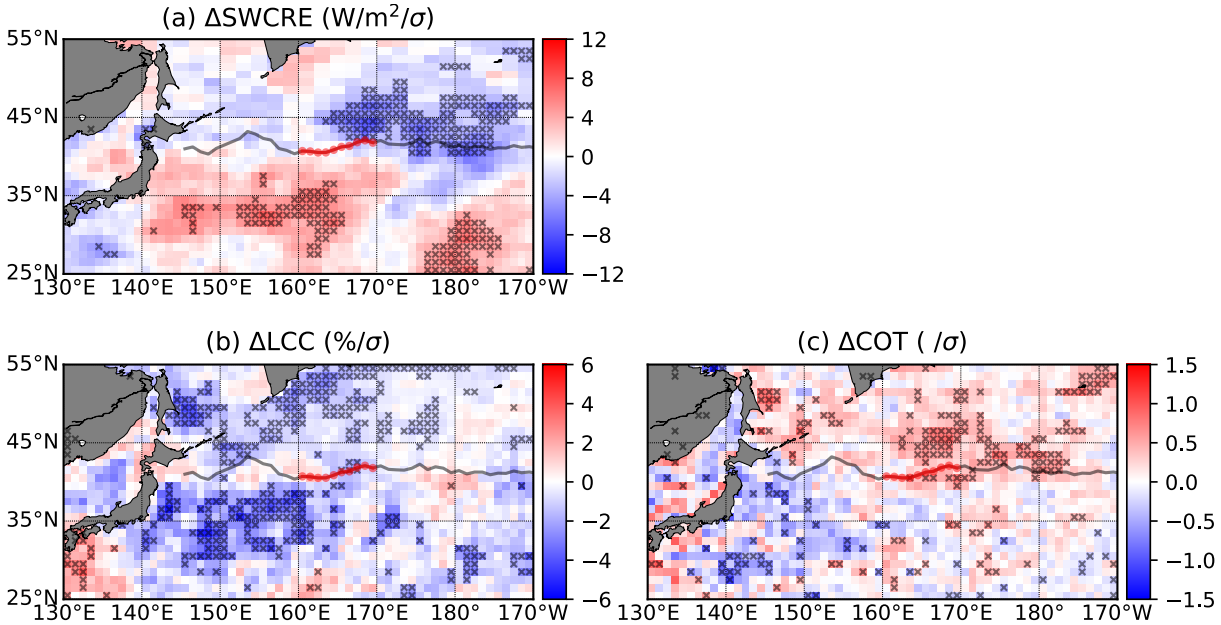

Fig. 4.10. As in Fig. 4.5, but for **(a)** the shortwave cloud radiative effect (SWCRE; unit: W/m^2), **(b)** low-level cloud cover (LCC; unit: %), and **(c)** cloud optical thickness (COT; unit: none).

As reported in many previous studies, low-level cloud properties are modulated by not only the local SST but also other atmospheric variables as summarized in Klein et al. (2017). Figure 4.11 shows the responses of four other LCC controlling factors—namely EIS, T_{adv}, RH_{700}, and ω_{700}—to S_{SSTF}; all of these four factors have been widely used in previous studies. When S_{SSTF} is increased, ΔEIS is negative in the southern flank of the SSTF, and the opposite in the northern flank (Fig. 4.11a). Negative ΔEIS caused by a positive ΔSST indicates unstable conditions in the lower troposphere, which is unfavorable for the formation of low-level cloud (Klein and Hartmann 1993; Wood and Bretherton 2006; Kawai et al. 2017). Although the low-level cloud tends to form with cold T_{adv} through a destabilization process in the atmospheric boundary layer (Wood 2012), ΔT_{adv} was observed to be negative in the southern flank of the SSTF where ΔLCC is negative (Figs. 4.10b and 4.11b). For other atmospheric factors that control LCC, ΔRH_{700} was negative (positive) in the southern (northern) flank (Fig. 4.11c) and $\Delta\omega_{700}$ was positive in the southern flank (Fig. 4.11d) indicating strong subsidence or weak updraft. Strong subsidence and a dry free-troposphere are also unfavorable conditions for low-level cloud formation (Bretherton et al. 2013; Myers and Norris 2013 2015). In conclusion, almost all of the LCC controlling factors except for T_{adv} responded simultaneously to the inter-annual variation of S_{SSTF} and acted to change the low-level cloud properties toward the same sign around the IJ2 SSTF region.

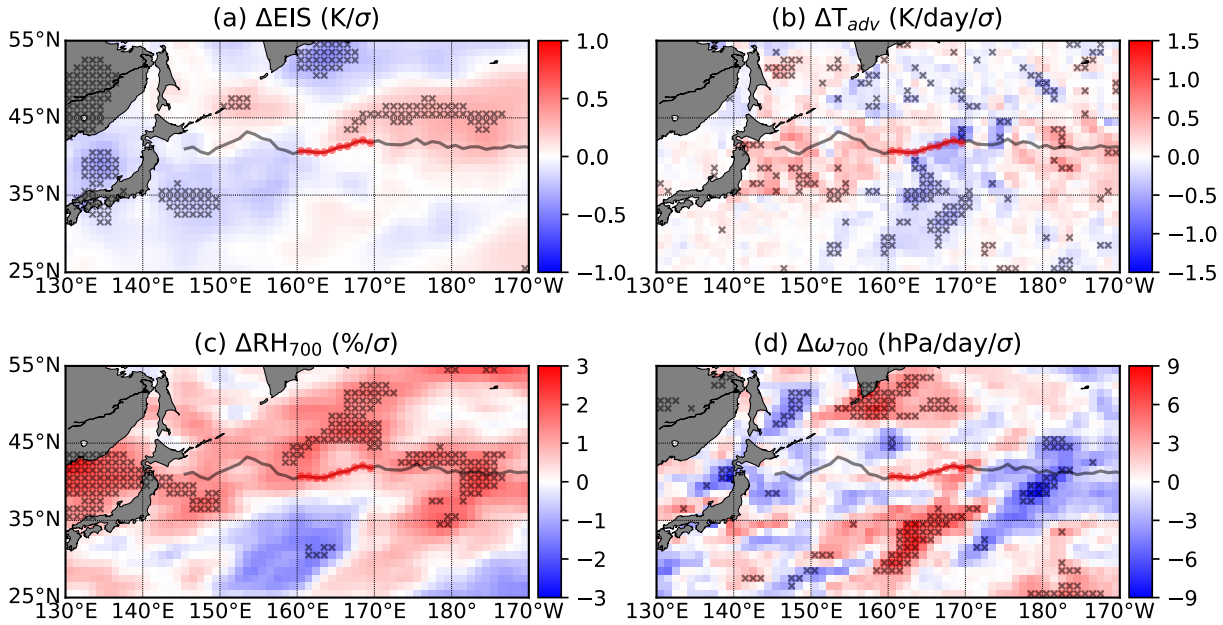

Fig. 4.11. As in Fig. 4.5, but for **(a)** estimated inversion strength (EIS) (unit: K), **(b)** horizontal air-temperature advection (T_{adv}) (unit: K/day), **(c)** relative humidity at 700 hPa (RH_{700}; unit: %), and (d) vertical pressure velocity at 700 hPa (ω_{700}; unit: hPa/day).

To quantify the relative contributions of the controlling factors to the properties of low-level cloud (Figs. 4.9 and 4.10), a multi-linear regression (MLR) analysis was conducted. The response of low-level cloud properties (referred to as C; i.e. LCC, COT, or SWCRE) to the increased S_{SSTF} is expressed as follows:

$$\Delta C = \frac{\partial C}{\partial S_{SSTF}} = \sum_i \frac{\partial C}{\partial x_i} \frac{\partial x_i}{\partial S_{SSTF}}, \quad (4.5)$$

where x_i is a controlling factor, namely, SST, EIS, T_{adv}, RH_{700}, or ω_{700}. The partial derivatives of the low-level cloud properties were calculated using a multi-linear regression approach similar to that used in previous studies (summarized in Klein et al. 2017). To construct the MLR model to estimate the response of low-level cloud to the five LCC controlling factors, we used the anomalies of all cloud parameters and predictors from each seasonal mean value in JJA at each grid point in the western NP region (130–170°W, 30–55°N). Due to multicollinearity between the SST and EIS, this model possibly underestimates the contributions from the SST and EIS. Then, from original EIS variability, we subtracted EIS regressed onto SST before calculating the slopes in the MLR model. Except for the removal of the multicollinearity between the SST and the EIS, this process is similar to the procedures used in previous studies focused on the amount of low-level cloud in subtropical regions (e.g., Klein et al. 2017). Table 4.1 shows the regression slopes calculated using the MLR model for LCC, COT, and SWCRE. The signs of the slopes are consistent with the physical mechanisms confirmed in previous observational and numerical simulation studies (e.g., Klein et al. 2017). For example, the negative slopes of LCC and COT to SST suggest that, when SST is low, low-level cloud appears more frequently and becomes more dense due to the suppression of the entrainment process of dry air from the free troposphere into the moist boundary layer (Bretherton et al. 2013; Qu et al. 2015). The variances of the three MLR models to the actual response of each low-level cloud variable are 67% for LCC, 40% for COT, and 80% for SWCRE. We also calculated the confidence interval from 5% to 95% of each slope, but the interval for each slope was smaller than the slope value itself by one order of magnitude.

Table 4.1 Calculated regression slopes for each cloud variable for each predictor in the multi-linear regression model of LCC, COT, and SWCRE

	$\partial C/\partial SST$	$\partial C/\partial EIS$	$\partial C/\partial T_{adv}$	$\partial C/\partial RH_{700}$	$\partial C/\partial \omega_{700}$
LCC	–3.67	3.89	–1.48	0.40	–0.05
COT	–0.46	–0.26	–0.10	0.02	–0.01
SWCRE	7.45	–2.85	1.67	–0.68	0.37

LCC: low-level cloud cover, COT: cloud optical thickness. SWCRE: shortwave cloud radiative effect

We recorded comparisons between the responses of low-level cloud to S_{SSTF} calculated directly by linear regression ("Actual") and those estimated using the MLR model ("Total") for LCC in the southern flank, COT in the northern flank, and SWCRE in both the northern and southern flanks of the IJ2 SSTF (Fig. 4.12). The figure also shows the contributions of each controlling factor calculated based on the slopes of each low-level cloud variable output by the MLR model (Table 4.1). These contributions show that SST is a primary controlling factor for all cloud responses. The ratio of the actual responses to the SST contribution was 82% for ΔLCC, 34% for ΔCOT, and 86% and 52% for ΔSWCRE in the southern and northern flanks of the IJ2 SSTF. Chapter 2 suggested that T_{adv} is likely to be a main driver of the LCC variability in the WNP on the intra-seasonal timescales (about 20–100 days), however, in the present chapter, we observed SST to be a main driver of LCC and T_{adv} a secondary contributor on inter-annual timescales. Additionally, The previous chapter also suggest that SST and EIS are followers of LCC variation on intra-seasonal timescales. This implies that the SST has the potential to actively modulate the LCC variation on inter-annual timescales, rather than on intra-seasonal timescales. We conclude that, even in the summertime IJ2 region, S_{SSTF} variation related to the Oyashio Extension can actively control the monthly-mean anomaly of LCC, COT, and SWCRE via, not the local atmospheric state, but rather via direct SST anomalies induced by a change in the western boundary currents. Figure 4.13 displays the meridional distribution of the actual response of low-level cloud properties to the increased S_{SSTF} and the responses estimated using the MLR model, showing similar results to those obtained in Fig. 4.12. However, in Fig. 4.13, the MLR model could not adequately capture the spatial characteristics of low-level cloud responses on a small spatial scale (i.e., a frontal scale at a Δlatitude of around 0°). This demonstrates the difficulty in depicting the direct impact of the increased S_{SSTF} on low-level cloud properties.

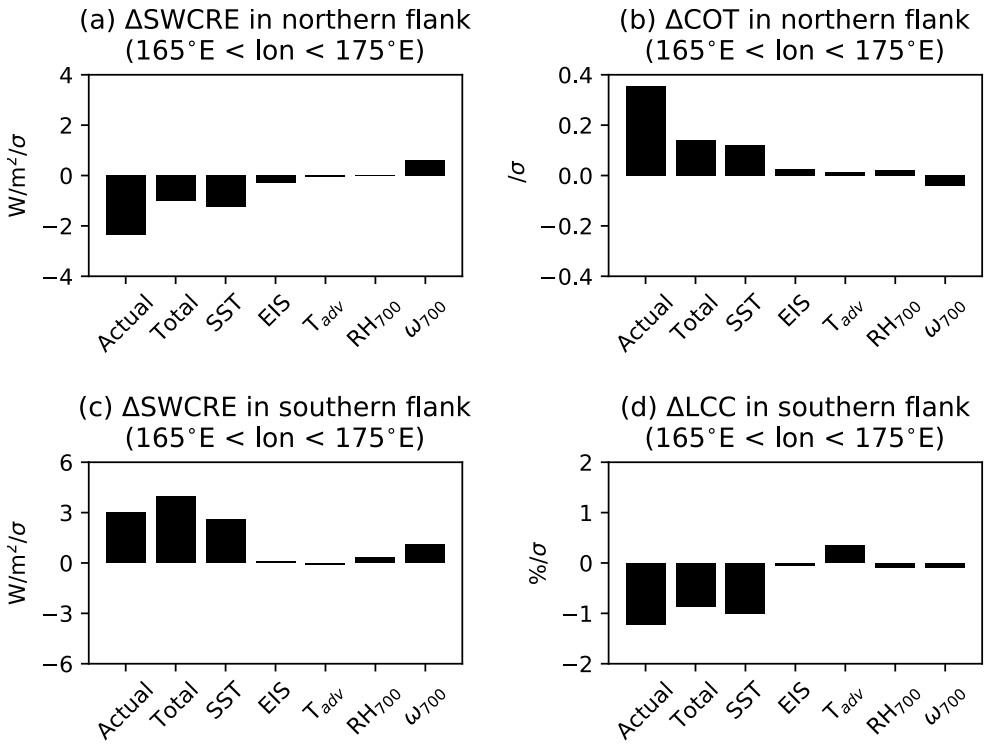

Fig. 4.12. Area-mean responses of **(a)** the shortwave cloud radiative effect (SWCRE) in the northern flank, **(b)** cloud optical thickness (COT) in the northern flank, **(c)** SWCRE in the southern flank, and **(d)** low-level cloud cover (LCC) in the southern flank of the Isoguchi Jet 2 sea surface temperature front to the increased strength of the sea surface temperature front. The actual response of each low-level cloud variable ("Actual"), the total response of each low-level cloud variable estimated using the multi-linear regression model (Total), and the contributions of each of the local LCC controlling factors (sea surface temperature [SST], estimated inversion strength [EIS], horizontal air-temperature advection [T_{adv}], relative humidity at 700 hPa [RH700], and vertical pressure velocity at 700 hPa [ω_{700}]) are also plotted.

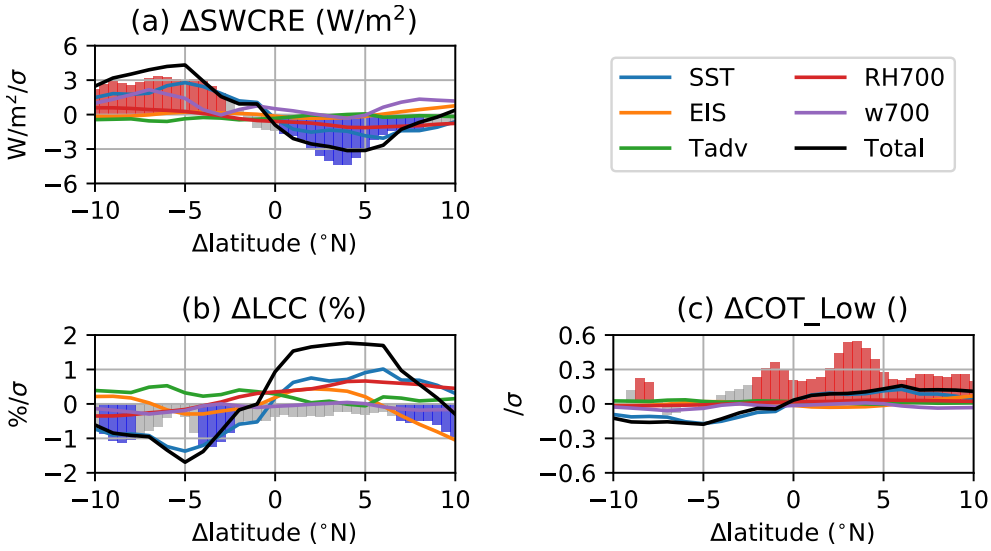

Fig. 4.13. As in Fig. 4.9, but for the total response estimated using the multi-linear regression model (Total), and the contributions of each controlling factor of the local low-level cloud cover (sea surface temperature [SST], estimated inversion strength [EIS], horizontal air-temperature advection [T_{adv}], relative humidity at 700 hPa [RH700], and vertical pressure velocity at 700 hPa [ω_{700}]) are also plotted.

4.5 Discussion and Summary

This chapter investigated the response of the properties of summertime low-level cloud to the properties of the SSTF (i.e., the strength of SST front; S_{SSTF}) associated with the Oyashio Extension in the WNP on inter-annual timescales, using satellite observational data, an atmospheric reanalysis dataset, and Argo float observations. The mechanisms responsible for the inter-annual variation of S_{SSTF} was investigated in detail before calculating the low-level cloud response to this variable. The results indicate that there is a strong contribution from the western boundary currents (i.e., the Kuroshio Extension) to changes in the properties of the SSTF in the summertime WNP, and that atmospheric forcing is the dominant contributing factor across a wide area of the CNP. The response of low-level cloud to the ocean-induced variation in the S_{SSTF} showed that positive (negative) SWCRE with less LCC (more COT) in the southern (northern) flank of the SSTF can be induced by a warm (cold) SST anomalies when S_{SSTF} is increased. Furthermore, the low-level cloud responses to the S_{SSTF} were examined using a multi-linear regression model to quantify the contributions from SST and other atmospheric factors (e.g., EIS and T_{adv}). The results of this model suggest that the local SST anomaly is a primary factor controlling the LCC, COT, and SWCRE responses to the S_{SSTF} in summertime. However, other atmospheric controlling factors make only minor contributions.

Although the variation in the S_{SSTF} might be related to oceanic forcing, the SST anomaly also seems to be forced by the SWCRE of low-level cloud due to the positive feedback loop between the SST and low-level cloud (Norris and Leovy 1994). Using the HF term in the mixed-layer temperature budget equation (Moisan and Niiler 1998), we estimated how SST can be forced by ΔSWCRE; the ratio of the estimated ΔSST to the actual ΔSST shown in Fig. 4.14. As shown in Figs. 4.9a and 4.10a, positive (negative) ΔSWCRE appears in the southern (northern) flank of the SSTF, which induces warming (cooling) of the SST when the S_{SSTF} is high. Thermodynamically, the meridional distribution of ΔSWCRE induced by ΔSST can enhance S_{SSTF} within a positive feedback loop. However, we found no significant correlation between S_{SSTF} in the meridional direction and the meridional gradient of the SW directly over the SSTF (the IJ2 region in Fig. 4.8). This implies that there is no robust observational evidence for the feedback between S_{SSTF} and the SWCRE induced by low-level cloud on the frontal spatial scales (< 300 km). However, far away from the SSTF in both flanks of the IJ2 SSTF (around 35°N or 45°N), ΔSWCRE-induced ΔSST can explain about half of the actual ΔSST. The area-mean ratios of the SST response in the northern and southern flanks of the IJ2 SSTF are 51% and 47%, respectively (Fig. 4.14b). In other words, the large-scale characteristics of the SST can be modulated by the radiative effect of low-level cloud, but the primary driver for frontal ΔSST might be oceanic forcing associated with the western boundary currents. This represents further evidence of the active role of the SST anomaly in modulating low-level cloud without the contribution from surface heat flux.

In the present chapter, we used the monthly mean datasets to assess the interaction between the low-level cloud and oceanic properties in the mid-latitude oceanic frontal zone. However, the timescale of the dominant mode of low-level cloud variability is shorter than inter-annual (de Szoeke et al. 2016), and therefore cannot be resolved using the monthly mean datasets. In particular, atmospheric synoptic disturbances in the mid-latitude NP strongly affect the variability of low-level clouds (Norris and Iacobellis 2005; Chapter 2), which means investigation cannot be properly carried out using the observational datasets nor represented well in general circulation models. The timescale of SST variability is longer than that of clouds due to the large heat capacity of the oceans. This difference in timescale complicates the understanding of the air–sea interactions. In chapter 3, the sensitivity of low-level cloud properties to the increased SSTF was investigated via Weather Research and Forecasting numerical simulation. That previous chapter also suggests the impact of SSTF on low-level cloud strongly depends on the synoptic-scale wind changes across the SSTF. To fully understand air–sea interaction, including cloud and its CRE, further analyses using high temporal and spatial resolution cloud datasets are required.

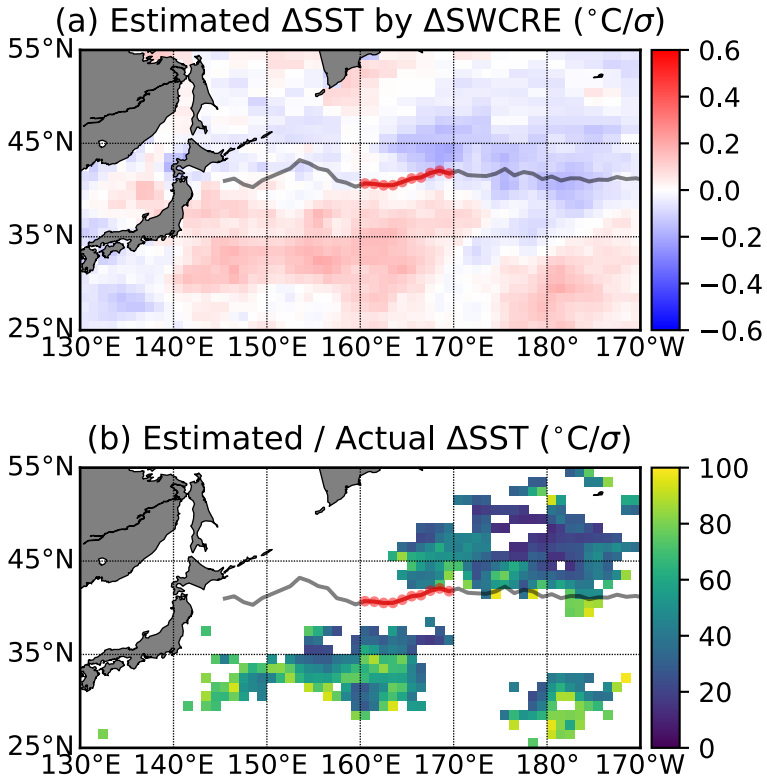

Fig. 4.14. Horizontal map of **(a)** estimated sea surface temperature (SST) response modulated by the shortwave cloud radiative effect (SWCRE) response shown in Fig. 4.10c, using the mixed-layer temperature equation for the increased strength of the sea surface temperature, **(b)** the ratio of the estimated SST response to the actual response (shown in Fig. 4.5) (unit: %). Only positive ratios are shown. The area-mean ratio of the SST response in the northern (southern) flank of the Isoguchi Jet 2 SST front (165–175°E) is 51% (47%).

Chapter 5

General Conclusion and Future Prospects

This study investigated the two-way physical processes within the feedback loop between oceanic low-level cloud properties and sea surface temperature (SST) in summertime North Pacific (NP), in terms of three timescales; 1) synoptic, 2) intra-seasonal, and 3) inter-annual. The entire goal of the present study was to seek a key driver of the feedback loop on each timescale and to reveal the physical mechanisms behind the feedback. We summarized the results in Chapter 2, 3, and 4 in following three paragraphs.

In Chapter 2, we investigated the phase relationship between low-level cloud cover (LCC) and SST in order to reveal the roles of atmosphere and ocean in intra-seasonal timescale, based on satellite data analysis in the western North Pacific (NP) in summertime. To answer the scientific question; "Which is a primarily trigger of the feedback loop on intra-seasonal timescale; LCC or SST in summertime?", we described the detailed processes of evolution of LCC based on phase composite analysis particularly focused on the relative humidity (RH), and evolution of SST based on mixed layer temperature budget analysis. We obtained three main results through the above investigations. First, intra-seasonal variability of LCC leads to SST, and that of horizontal dry-cold advection is a trigger for increasing LCC and decreasing SST on this timescale in summertime western NP. Second, the increasing LCC corresponds to the positive RH anomaly in the boundary layer induced by decreasing saturated water vapor pressure due to anomalous cold temperatures brought by the advection, and vice versa. Third, anomalous dry-cold advection is important for cooling of SST, not only via enhanced latent heat release but also via decreasing downward shortwave radiation at the sea surface according to a positive LCC anomaly due to the cold advection anomaly. We pointed out the intra-seasonal variability of large-scale atmospheric circulation is important to connect the LCC-SST relationship and leading mode in the feedback loop is LCC, rather than SST. We further investigated the regionality of the physical linkage among LCC, SST, and T_{adv} described above, suggesting that the robust linkage appears in two specific regions; 1) southern flank of SST frontal zone in central and western NP and 2) eastern NP, where dominant cloud type is stratocumulus. The method to determine the detailed phase relationship between LCC and its controlling factor in this chapter is proposed as a useful approach to understand their causality; i.e. local processes of both low-level cloud evolution

and interaction with SST.

In Chapter 3, we examined the mechanism of oceanic modulation process of low-level cloud properties based on the WRF numerical simulation since it is difficult to extract the active role of SST based on only observational data analysis (cf. Chapter 2). The timescales focused on in this chapter are synoptic timescale. Key scientific question is "Does the SST front play an active role in modulating the synoptic variability of the low-level cloud properties in summertime? If so, what is the mechanism?". We ran two numerical experiments forced by different SST conditions with and without SST frontal characteristics associated with Oyashio Extension, where horizontal gradient of SST is the strongest in the NP induced by oceanic dynamics within the western boundary current. The differences in experiments, therefore, can reveal the impact of SST front on the atmosphere and low-level cloud, implying the two mechanisms about physical modulation process of marine fog via SST changes. The one process is similar with previously proposed mechanism associated with SST forcing to low-level cloud (e.g. Bretherton et al., 2013); local cold SST anomaly in the northern flank of SST font can modulate positive anomaly of relative humidity (RH) near sea surface due to the SST cooling, which is favorable condition for the marine fog formation (SST anomaly effect). Another process is that horizontal temperature advection from warm to cold flanks of the SST front near sea surface can suppress the marine fog formation in the northern flank via modulation of RH anomaly near SST front (SST frontal effect). They imply that the importance of not only local SST anomaly but also SST frontal characteristics are important for determining seasonal mean state and synoptic variability of low-level cloud in summertime. In other word, not only 1D vertical process associated with SSTA but also 2D horizontal process associated with SST frontal characteristics are important to modulate the fog formation. Additionally, it suggests the interaction process beyond the different timescales, that is, the modulation of relatively long-term variation of the SST front for the short-term variation of low-level cloud properties associated with synoptic disturbances via cross-frontal wind variability.

In Chapter 4, we tried to investigate the active role of summertime Oyashio Extension SST front variation in modulating low-level cloud properties (cloud cover [LCC], cloud optical thickness [COT], and shortwave cloud radiative effect [SWCRE]) on inter-annual timescale, based on various observational datasets from 2003 to 2016. Key scientific question is "Can we obtain the observational evidence of the active role of SST? How much variation of the low-level cloud properties on inter-annual timescale can be attributed to the SST effect in the real world?". While the difficulty of distinguishing the two-way process in the feedback loop on relatively shorter timescale by data analysis, we avoid this timescale problem by focusing on the inter-annual timescale variability of SST front driven by the oceanic dynamics associated with the western boundary currents. We firstly paid attention to the mechanism of summertime SSTF variability itself. Strength of the SST front (S_{SSTF}) defined as maximum horizontal gradient of SST has clear inter-annual variations. Regression analysis for subsurface temperature and frontogenesis equation analysis indicated that inter-annual variation of the summertime S_{SSTF} in the western north Pacific are strongly related with Kuroshio and Oyashio

Extension variabilities. Low-level cloud response to the ocean-induced SST front variation shows that positive (negative) SW CRE with less LCC (more cloud optical thickness [COT]) in the southern (northern) flank of SSTF can be induced by warm (cold) SST anomaly when S_{SSTF} is strengthened. The SST contribution to modulating the low-level cloud is the largest in the low-level cloud controlling factors (i.e. estimated inversion strength, air-temperature advection) by more than 40 %. It also implies the importance of modulating the entrainment process of dry-air from the free troposphere induced by SST anomaly. The present study based on combined datasets showed an observational evidence for active role of summertime frontal SST anomaly induced by western boundary current in SST-LCC feedback process on inter-annual timescale. Combined with the result in Chapter 3, the results in the present studies are robust and new observational evidences about the active role of ocean for mean-state and variability of low-level clouds in summertime.

As the detailed introduction and discussion in Chapters 1 and 4, summertime SST is previously recognized as passive role by atmospheric forcing, due to the so thin mixed layer depth that SST is sensitive to surface heat flux (e.g. Tanimoto et al., 2003). Contrast with the general recognition of passive role of ocean in summertime, our results in Chapter 3 and 4 indicated the active role of SST to low-level cloud properties associated with the western boundary currents variability, such as the Kuroshio and Oyashio currents. SST in central area of NP, however, tends to be forced by surface heat flux variability due to the changes of wind speed, humidity, air-temperature near sea surface, and SW radiation associated with the atmospheric and cloud variabilities in summertime, compared with the specific western boundary current regions (Chapter 3, 4). Although we focused on only the western NP regions, other western boundary currents lie in Atlantic and Indian Ocean, such as Gulf stream in North Atlantic, Brazil-Malvinas current in South Atlantic, and Agulhas current in south Indian Ocean. Characteristics of SST front and large-scale atmospheric circulation are different in all western boundary current region; thus, advanced understanding of coupling among the cloud, SST, and the atmospheric circulation might be brought by the comparison with the different regions. Additionally, recent studies indicated changes in the properties of western boundary currents (e.g. position and strength) with recent global warming, for example Oyashio Extension SST front shifted to poleward exerted by the changes in wind stress field (Wu et al., 2018). Similar analysis to Wu et al. (2018) for the other SST frontal regions may lead to further understanding of climate response to the global warming in mid-latitude. The contribution of feedback mechanism between low-level cloud and SST, associated with summertime high-pressure system in each ocean basin also remain unclear (e.g. Wei et al., 2018). Therefore, the active role of SST or SST front in low-level cloud properties proposed in this study can also contribute to identify the cloud changes with global warming due to the changes in oceanic dynamics and atmospheric dynamics.

Previous studies investigated the physical process between low-level cloud and the five controlling factors to construct multi-linear regression model for the prediction of low-level cloud changes with global warming (Klein et al., 2017); SST, estimated inversion strength (EIS), air-

temperature advection (T_{adv}), RH in the free troposphere (RH_{700}), and subsidence in the free troposphere (w_{700}). Especially, SST and EIS are recognized as the important LCC controlling factors on longer timescale (e.g. inter-annual or decadal timescales and climate change with global warming) (Chapter 4; Myers & Norris, 2016). For example, the contributions of SST and EIS to LCC changes with global warming are larger than that of other controlling factors, while they are almost cancelled out each other. In contrast, the importance of T_{adv} becomes more and more on shorter timescale (Chapter 2; Kubar et al., 2012; Miyamoto et al., 2018). The present study revealed the two-way physical processes between low-level cloud and SST on various timescale and implied the different interaction process across the different timescale (i.e. synoptic/intra-seasonal and inter-annual timescales). The future study can extend the further investigation for more longer timescale than those we focused on, that is, the decadal variability which is characterized as Pacific Decadal Oscillation (PDO; Mantua et al., 1997; Newman et al., 2016), Atlantic Multidecadal Oscillation (AMO; Kerr, 2000), Inter-decadal Pacific Oscillation (IPO; Power et al., 1999). Three decadal modes listed above are thought to be closely related with the oceanic and air-sea coupling processes rather than the internal atmospheric process. Therefore, the three analyzing method proposed in this thesis can be applied to the decadal variability, in order to understand the mechanisms behind these long-term variabilities and the importance of the oceanic process modulating cloud and the large-scale atmospheric circulation. Recent studies suggested the importance of cloud-SST feedback to amplify these inter-annual or decadal oscillations by coupled atmosphere-ocean models (Middlemas et al., 2019a, b; Radel et al., 2016). For example, inter-annual oscillation of SST anomaly in the subtropics can be amplified significantly by cloud radiative effect, revealed by the coupled numerical experiments with and without cloud-SST interaction. It implied the further understanding of the coupling process between cloud and SST on inter-annual and decadal timescales based on observations are needed to reduce the uncertainty of the long-term SST variability. Finally, based on the results about oceanic modulation of synoptic cloud variation, we also imply that the accurate representation of the interaction process among cloud, SST, the atmospheric circulation in the model can help to improve future prediction of not only climate but also weather disturbances such as extreme event.

References

Argo. (2000). Argo float data and metadata from Global Data Assembly Centre (Argo GDAC). SEANOE. https://doi.org/10.17882/42182

Babić, K., Adler, B., Kalthoff, N., Andersen, H., Dione, C., Lohou, F., et al. (2018). The observed diurnal cycle of nocturnal low-level stratus clouds over southern West Africa: a case study. *Atmospheric Chemistry and Physics Discussions*, 1–29. https://doi.org/10.5194/acp-2018-776

Bony, S., & Dufrense, J.-L. (2005). Marine boundary layer clouds at the heart of tropical cloud feedback uncertainties in climate models. *Geophysical Research Letters*, ***32*****(20)**, L20806. https://doi.org/10.1029/2005GL023851

Bretherton, C. S., Blossey, P. N., & Jones, C. R. (2013). Mechanisms of marine low cloud sensitivity to idealized climate perturbations: A single-LES exploration extending the CGILS cases. *Journal of Advances in Modeling Earth Systems*. https://doi.org/10.1002/jame.20019

Brient, F., & Bony, S. (2013). Interpretation of the positive low-cloud feedback predicted by a climate model under global warming. *Climate Dynamics*, ***40*****(9–10)**, 2415–2431. https://doi.org/10.1007/s00382-011-1279-7

Chelton, D. B. (2005). The Impact of SST Specification on ECMWF Surface Wind Stress Fields in the Eastern Tropical Pacific. *Journal of Climate*, ***18*****(4)**, 530–550. https://doi.org/10.1175/JCLI-3275.1

Cohen, A. E., Cavallo, S. M., Coniglio, M. C., & Brooks, H. E. (2015). A review of planetary boundary layer parameterization schemes and their sensitivity in simulating southeastern U.S. cold season severe weather environments. *Weather and Forecasting*, ***30*****(3)**, 591–612. https://doi.org/10.1175/WAF-D-14-00105.1

Cronin, M. F., Bond, N. A., Thomas Farrar, J., Ichikawa, H., Jayne, S. R., Kawai, Y., et al. (2013). Formation and erosion of the seasonal thermocline in the Kuroshio Extension Recirculation Gyre. *Deep Sea Research Part II: Topical Studies in Oceanography*, ***85***, 62–74. https://doi.org/10.1016/j.dsr2.2012.07.018

Dee, D. P., Uppala, S. M., Simmons, A. J., Berrisford, P., Poli, P., Kobayashi, S., et al. (2011). The ERA-Interim reanalysis: Configuration and performance of the data assimilation system. *Quarterly Journal of the Royal Meteorological Society*. https://doi.org/10.1002/qj.828

de Szoeke, S. P., Verlinden, K. L., Yuter, S. E., & Mechem, D. B. (2016). The time scales of variability of marine low clouds. *Journal of Climate*, ***29*****(18)**, 6463–6481. https://doi.org/10.1175/JCLI-D-15-0460.1

Dudhia, J. (1989). Numerical Study of Convection Observed during the Winter Monsoon Experiment Using a Mesoscale Two-Dimensional Model. *Journal of the Atmospheric Sciences*, ***46*****(20)**, 3077–3107. https://doi.org/10.1175/1520-0469(1989)046<3077:NSOCOD>2.0.CO;2

Ek, M. B., & Mahrt, L. (1994). Daytime Evolution of Relative Humidity at the Boundary Layer Top. *Monthly Weather Review*, ***122*****(12)**, 2709–2721. https://doi.org/10.1175/1520-0450

Frankignoul, C., & Hasselmann, K. (1977). Stochastic climate models, Part II Application to sea-surface temperature anomalies and thermocline variability. *Tellus*, ***29*****(4)**, 289–305. https://doi.org/10.1111/j.2153-3490.1977.tb00740.x

Frankignoul, C., & Reynolds, R. W. (1983). Testing a Dynamical Model for Mid-Latitude Sea Surface Temperature Anomalies. *Journal of Physical Oceanography*, ***13*****(7)**, 1131–1145. https://doi.org/10.1175/1520-0485(1983)013<1131:TADMFM>2.0.CO;2

Frankignoul, C. (1985). Sea surface temperature anomalies, planetary waves, and air-sea feedback in the middle latitudes. *Reviews of Geophysics*, ***23*****(4)**, 357. https://doi.org/10.1029/RG023i004p00357

Frankignoul, C., Sennéchael, N., Kwon, Y.-O., & Alexander, M. A. (2011). Influence of the Meridional Shifts of the Kuroshio and the Oyashio Extensions on the Atmospheric Circulation. *Journal of Climate*, ***24*****(3)**, 762–777. https://doi.org/10.1175/2010JCLI3731.1

Gelaro, R., McCarty, W., Suárez, M. J., Todling, R., Molod, A., Takacs, L., et al. (2017). The modern-era retrospective analysis for research and applications, version 2 (MERRA-2). *Journal of Climate*, ***30*****(14)**, 5419–5454. https://doi.org/10.1175/JCLI-D-16-0758.1

Harrison, E. F., Minnis, P., Barkstrom, B. R., Ramanathan, V., Cess, R. D., & Gibson, G. G. (1990). Seasonal variation of cloud radiative forcing derived from the Earth Radiation Budget Experiment. *Journal of Geophysical Research*, ***95*****(D11)**. https://doi.org/10.1029/jd095id11p18687

Hartmann, D. L., & Short, D. A. (1980). On the Use of Earth Radiation Budget Statistics for Studies of Clouds and Climate. *Journal of the Atmospheric Sciences*, ***37*****(6)**, 1233–1250. https://doi.org/10.1175/1520-0469(1980)037<1233:OTUOER>2.0.CO;2

Hong, S.-Y., Noh, Y., & Dudhia, J. (2006). A New Vertical Diffusion Package with an Explicit Treatment of Entrainment Processes. *Monthly Weather Review*, ***134*****(9)**, 2318–2341. https://doi.org/10.1175/MWR3199.1

Hosoda, S., Ohira, T., & Nakamura, T. (2008). *A monthly mean dataset of global oceanic temperature* (Vol. **8**).

Hosoda, S., Nonaka, M., Sasai, Y., & Sasaki, H. (2016). Early summertime interannual variability in

surface and subsurface temperature in the North Pacific. In *"Hot Spots" in the Climate System* (pp. 91–107). Tokyo: Springer Japan. https://doi.org/10.1007/978-4-431-56053-1_6

Isoguchi, O., Kawamura, H., & Oka, E. (2006). Quasi-stationary jets transporting surface warm waters across the transition zone between the subtropical and the subarctic gyres in the North Pacific. *Journal of Geophysical Research*, ***111*(C10)**, C10003. https://doi.org/10.1029/2005JC003402

Janjić, Z. I. (1994). The Step-Mountain Eta Coordinate Model: Further Developments of the Convection, Viscous Sublayer, and Turbulence Closure Schemes. *Monthly Weather Review*, ***122*(5)**, 927–945. https://doi.org/10.1175/1520-0493(1994)122<0927:TSMECM>2.0.CO;2

Jiang, Y., Zhang, S., Xie, S., Chen, Y., & Liu, H. (2019). Effects of a Cold Ocean Eddy on Local Atmospheric Boundary Layer Near the Kuroshio Extension: In Situ Observations and Model Experiments. *Journal of Geophysical Research: Atmospheres*, 2018JD029382. https://doi.org/10.1029/2018JD029382

Johnson, G. C., Schmidtko, S., & Lyman, J. M. (2012). Relative contributions of temperature and salinity to seasonal mixed layer density changes and horizontal density gradients. *Journal of Geophysical Research: Oceans*, ***117*(C4)**, n/a-n/a. https://doi.org/10.1029/2011JC007651

Kain, J. S. (2004). The Kain–Fritsch Convective Parameterization: An Update. *Journal of Applied Meteorology*, ***43*(1)**, 170–181. https://doi.org/10.1175/1520-0450(2004)043<0170:TKCPAU>2.0.CO;2

Kato, S., Rose, F. G., Rutan, D. A., Thorsen, T. J., Loeb, N. G., Doelling, D. R., et al. (2018). Surface Irradiances of Edition 4.0 Clouds and the Earth's Radiant Energy System (CERES) Energy Balanced and Filled (EBAF) Data Product. *Journal of Climate*, ***31*(11)**, 4501–4527. https://doi.org/10.1175/JCLI-D-17-0523.1

Kawai, H., Koshiro, T., Endo, H., Arakawa, O., & Hagihara, Y. (2016). Changes in marine fog in a warmer climate. *Atmospheric Science Letters*, ***17*(10)**, 548–555. https://doi.org/10.1002/asl.691

Kawai, H., Koshiro, T., & Webb, M. J. (2017). Interpretation of factors controlling low cloud cover and low cloud feedback using a unified predictive index. *Journal of Climate*, ***30*(22)**, 9119–9131. https://doi.org/10.1175/JCLI-D-16-0825.1

Kawai, Y., Miyama, T., Iizuka, S., Manda, A., Yoshioka, M. K., Katagiri, S., et al. (2015). Marine atmospheric boundary layer and low-level cloud responses to the Kuroshio Extension front in the early summer of 2012: three-vessel simultaneous observations and numerical simulations. *Journal of Oceanography*, ***71*(5)**, 511–526. https://doi.org/10.1007/s10872-014-0266-0

Kawamura, R., Murakami, T., & Wang, B. (1996). Tropical and Mid-latitude 45-Day Perturbations

over the Western Pacific During the Northern Summer. *Journal of the Meteorological Society of Japan. Ser. II*, ***74*(6)**, 867–890. https://doi.org/10.2151/jmsj1965.74.6_867

Kazmin, A. S. (2016). The Frontal System at the Boundary of the East China Sea : Its Variability and Response to Large-Scale Atmospheric Forcing, ***56*(4)**, 509–513. https://doi.org/10.1134/S000143701604007X

Kerr, R. A. (2000). A North Atlantic Climate Pacemaker for the Centuries. *Science*, ***288*(5473)**, 1984–1985. https://doi.org/10.1126/science.288.5473.1984

Kida, S., Mitsudera, H., Aoki, S., Guo, X., Ito, S. I., Kobashi, F., et al. (2016). Oceanic fronts and jets around Japan: A review. *Hot Spots in the Climate System: New Developments in the Extratropical Ocean-Atmosphere Interaction Research*, 1–30. https://doi.org/10.1007/978-4-431-56053-1_1

Kilpatrick, T., Schneider, N., & Qiu, B. (2014). Boundary Layer Convergence Induced by Strong Winds across a Midlatitude SST Front*. *Journal of Climate*, ***27*(4)**, 1698–1718. https://doi.org/10.1175/JCLI-D-13-00101.1

Kilpatrick, T., Schneider, N., & Qiu, B. (2016). Atmospheric Response to a Midlatitude SST Front: Alongfront Winds. *Journal of the Atmospheric Sciences*, ***73*(9)**, 3489–3509. https://doi.org/10.1175/JAS-D-15-0312.1

Klein, S. A., & Hartmann, D. L. (1993). The Seasonal Cycle of Low Stratiform Clouds. *Journal of Climate*, ***6*(8)**, 1587–1606. https://doi.org/10.1175/1520-0442(1993)006<1587:TSCOLS>2.0.CO;2

Klein, S. A. (1997). Synoptic Variability of Low-Cloud Properties and Meteorological Parameters in the Subtropical Trade Wind Boundary Layer. *Journal of Climate*, ***10*(8)**, 2018–2039. https://doi.org/10.1175/1520-0442(1997)010<2018:SVOLCP>2.0.CO;2

Klein, S. A., Hall, A., Norris, J. R., & Pincus, R. (2017). Low-Cloud Feedbacks from Cloud-Controlling Factors: A Review. *Surveys in Geophysics*, ***38*(6)**, 1307–1329. https://doi.org/10.1007/s10712-017-9433-3

Kobayashi, S., Ota, Y., Harada, Y., Ebita, A., Moriya, M., Onoda, H., et al. (2015). The JRA-55 reanalysis: General specifications and basic characteristics. *Journal of the Meteorological Society of Japan*, ***93*(1)**, 5–48. https://doi.org/10.2151/jmsj.2015-001

Koračin, D., Dorman, C. E., Lewis, J. M., Hudson, J. G., Wilcox, E. M., & Torregrosa, A. (2014). Marine fog: A review. *Atmospheric Research*, ***143***, 142–175. https://doi.org/10.1016/j.atmosres.2013.12.012

Koshiro, T., & Shiotani, M. (2014). Relationship between Low Stratiform Cloud Amount and

Estimated Inversion Strength in the Lower Troposphere over the Global Ocean in Terms of Cloud Types. *Journal of the Meteorological Society of Japan. Ser. II*, ***92*****(1)**, 107–120. https://doi.org/10.2151/jmsj.2014-107

Koshiro, T., Yukimoto, S., & Shiotani, M. (2017). Interannual variability in low stratiform cloud amount over the summertime north pacific in terms of cloud types. *Journal of Climate*, ***30*****(16)**, 6107–6121. https://doi.org/10.1175/JCLI-D-16-0898.1

Kubar, T. L., Waliser, D. E., Li, J. L., & Jiang, X. (2012). On the annual cycle, variability, and correlations of oceanic low-topped clouds with large-scale circulation using aqua MODIS and ERA-interim. *Journal of Climate*, ***25*****(18)**, 6152–6174. https://doi.org/10.1175/JCLI-D-11-00478.1

Kuwano-Yoshida, A., & Minobe, S. (2017). Storm-track response to SST fronts in the Northwestern Pacific Region in an AGCM. *Journal of Climate*, ***30*****(3)**, 1081–1102. https://doi.org/10.1175/JCLI-D-16-0331.1

Kwon, Y. O., Alexander, M. A., Bond, N. A., Frankignoul, C., Nakamura, H., Qiu, B., & Thompson, L. A. (2010). Role of the gulf Stream and Kuroshio-Oyashio systems in large-scale atmosphere-ocean interaction: A review. *Journal of Climate*. https://doi.org/10.1175/2010JCLI3343.1

Li, J., Huang, J., Stamnes, K., Wang, T., Lv, Q., & Jin, H. (2015). A global survey of cloud overlap based on CALIPSO and CloudSat measurements. *Atmospheric Chemistry and Physics*, ***15*****(1)**, 519–536. https://doi.org/10.5194/acp-15-519-2015

Liu, J. W., Xie, S. P., Norris, J. R., & Zhang, S. P. (2014). Low-level cloud response to the gulf stream front in winter using CALIPSO. *Journal of Climate*. https://doi.org/10.1175/JCLI-D-13-00469.1

Mantua, N. J., Hare, S. R., Zhang, Y., Wallace, J. M., & Francis, R. C. (1997). A Pacific Interdecadal Climate Oscillation with Impacts on Salmon Production. *Bulletin of the American Meteorological Society*, ***78*****(6)**, 1069–1079. https://doi.org/10.1175/1520-0477(1997)078<1069:APICOW>2.0.CO;2

Mauger, G. S., & Norris, J. R. (2010). Assessing the impact of meteorological history on subtropical cloud fraction. *Journal of Climate*. https://doi.org/10.1175/2010JCLI3272.1

McCoy, D. T., Eastman, R., Hartmann, D. L., & Wood, R. (2017). The Change in Low Cloud Cover in a Warmed Climate Inferred from AIRS, MODIS, and ERA-Interim. *Journal of Climate*, ***30*****(10)**, 3609–3620. https://doi.org/10.1175/JCLI-D-15-0734.1

Middlemas, E. A., Clement, A. C., Medeiros, B., & Kirtman, B. (2019). Cloud Radiative Feedbacks and El Niño–Southern Oscillation. *Journal of Climate*, ***32*****(15)**, 4661–4680.

https://doi.org/10.1175/JCLI-D-18-0842.1

Middlemas, E. A., Clement, A. C., & Medeiros, B. (2019). Contributions of atmospheric and oceanic feedbacks to subtropical northeastern sea surface temperature variability. *Climate Dynamics*, ***53*****(11)**, 6877–6890. https://doi.org/10.1007/s00382-019-04964-1

Minobe, S., Kuwano-Yoshida, A., Komori, N., Xie, S. P., & Small, R. J. (2008). Influence of the Gulf Stream on the troposphere. *Nature*, ***452*****(7184)**, 206–209. https://doi.org/10.1038/nature06690

Minobe, S., Miyashita, M., Kuwano-Yoshida, A., Tokinaga, H., & Xie, S.-P. (2010). Atmospheric Response to the Gulf Stream: Seasonal Variations*. *Journal of Climate*, ***23*****(13)**, 3699–3719. https://doi.org/10.1175/2010JCLI3359.1

Miyamoto, A., Nakamura, H., & Miyasaka, T. (2018). Influence of the Subtropical High and Storm Track on Low-Cloud Fraction and Its Seasonality over the South Indian Ocean. *Journal of Climate*, ***31*****(10)**, 4017–4039. https://doi.org/10.1175/JCLI-D-17-0229.1

Mlawer, E. J., Taubman, S. J., Brown, P. D., Iacono, M. J., & Clough, S. A. (1997). Radiative transfer for inhomogeneous atmospheres: RRTM, a validated correlated-k model for the longwave. *Journal of Geophysical Research: Atmospheres*, ***102*****(D14)**, 16663–16682. https://doi.org/10.1029/97JD00237

Moisan, J. R., & Niiler, P. P. (1998). The Seasonal Heat Budget of the North Pacific: Net Heat Flux and Heat Storage Rates (1950–1990). *Journal of Physical Oceanography*, ***28*****(3)**, 401–421. https://doi.org/10.1175/1520-0485(1998)028<0401:TSHBOT>2.0.CO;2

Mori, M., & Watanabe, M. (2008). The Growth and Triggering Mechanisms of the PNA: A MJO-PNA Coherence. *Journal of the Meteorological Society of Japan*, ***86*****(1)**, 213–236. https://doi.org/10.2151/jmsj.86.213

Morioka, Y., Tozuka, T., & Yamagata, T. (2010). Climate variability in the southern Indian Ocean as revealed by self-organizing maps. *Climate Dynamics*, ***35*****(6)**, 1075–1088. https://doi.org/10.1007/s00382-010-0843-x

Myers, T. A., & Norris, J. R. (2013). Observational Evidence That Enhanced Subsidence Reduces Subtropical Marine Boundary Layer Cloudiness. *Journal of Climate*, ***26*****(19)**, 7507–7524. https://doi.org/10.1175/JCLI-D-12-00736.1

Myers, T. A., & Norris, J. R. (2015). On the relationships between subtropical clouds and meteorology in observations and CMIP3 and CMIP5 models. *Journal of Climate*, ***28*****(8)**, 2945–2967. https://doi.org/10.1175/JCLI-D-14-00475.1

Myers, T. A., & Norris, J. R. (2016). Reducing the uncertainty in subtropical cloud feedback.

Geophysical Research Letters, ***43*****(5)**, 2144–2148. https://doi.org/10.1002/2015GL067416

Myers, T. A., Mechoso, C. R., & Deflorio, M. J. (2017). Coupling between marine boundary layer clouds and summer- to-summer sea surface temperature variability over the North Atlantic and Pacific. *Climate Dynamics*, ***0*****(0)**, 1–15. https://doi.org/10.1007/s00382-017-3651-8

Nakamura, H., & Yamagata, T. (1999). *Beyond El Niño*. (A. Navarra, Ed.), *Climate in Flux*. Berlin, Heidelberg: Springer Berlin Heidelberg. https://doi.org/10.1007/978-3-642-58369-8

Nakamura, H., & Kazmin, A. S. (2003). Decadal changes in the North Pacific oceanic frontal zones as revealed in ship and satellite observations. *Journal of Geophysical Research*, ***108*****(C3)**, 3078. https://doi.org/10.1029/1999JC000085

Nakamura, H., Sampe, T., Tanimoto, Y., & Shimpo, A. (2004). Observed Associations Among Storm Tracks, Jet Streams and Midlatitude Oceanic Fronts. In *Geophysical Monograph Series* (Vol. 147, pp. 329–345). https://doi.org/10.1029/147GM18

Nakamura, H., Sampe, T., Goto, A., Ohfuchi, W., & Xie, S.-P. (2008). On the importance of midlatitude oceanic frontal zones for the mean state and dominant variability in the tropospheric circulation. *Geophysical Research Letters*, ***35*****(15)**, L15709. https://doi.org/10.1029/2008GL034010

Nakanishi, M., & Niino, H. (2006). An Improved Mellor–Yamada Level-3 Model: Its Numerical Stability and Application to a Regional Prediction of Advection Fog. *Boundary-Layer Meteorology*, ***119*****(2)**, 397–407. https://doi.org/10.1007/s10546-005-9030-8

Nakanishi, M., & Niino, H. (2009). Development of an Improved Turbulence Closure Model for the Atmospheric Boundary Layer. *Journal of the Meteorological Society of Japan*, ***87*****(5)**, 895–912. https://doi.org/10.2151/jmsj.87.895

Newman, M., Alexander, M. A., Ault, T. R., Cobb, K. M., Deser, C., Di Lorenzo, E., et al. (2016). The Pacific decadal oscillation, revisited. *Journal of Climate*. https://doi.org/10.1175/JCLI-D-15-0508.1

Norris, J. R., & Leovy, C. B. (1994). Interannual Variability in Stratiform Cloudiness and Sea Surface Temperature. *Journal of Climate*, ***7*****(12)**, 1915–1925. https://doi.org/10.1175/1520-0442(1994)007<1915:IVISCA>2.0.CO;2

Norris, J. R., Zhang, Y., & Wallace, J. M. (1998). Role of Low Clouds in Summertime Atmosphere–Ocean Interactions over the North Pacific. *Journal of Climate*, ***11*****(10)**, 2482–2490. https://doi.org/10.1175/1520-0442(1998)011<2482:ROLCIS>2.0.CO;2

Norris, J. R. (2000). Interannual and interdecadal variability in the storm track, cloudiness, and sea surface temperature over the summertime North Pacific. *Journal of Climate*, ***13*****(2)**, 422–430.

https://doi.org/10.1175/1520-0442(2000)013<0422:IAIVIT>2.0.CO;2

Norris, J. R., & Klein, S. A. (2000). Low cloud type over the ocean from surface observations. Part III: Relationship to vertical motion and the regional surface synoptic environment. *Journal of Climate*, ***13*****(1)**, 245–256. https://doi.org/10.1175/1520-0442(2000)013<0245:LCTOTO>2.0.CO;2

Ogawa, F., Nakamura, H., Nishii, K., Miyasaka, T., & Kuwano-Yoshida, A. (2012). Dependence of the climatological axial latitudes of the tropospheric westerlies and storm tracks on the latitude of an extratropical oceanic front. *Geophysical Research Letters*, ***39*****(5)**, 1–5. https://doi.org/10.1029/2011GL049922

Ogawa, F., & Spengler, T. (2019). Prevailing surface wind direction during air–sea heat exchange. *Journal of Climate*, ***32*****(17)**, 5601–5617. https://doi.org/10.1175/JCLI-D-18-0752.1

Ohishi, S., Tozuka, T., & Cronin, M. F. (2017). Frontogenesis in the Agulhas Return Current Region Simulated by a High-Resolution CGCM. *Journal of Physical Oceanography*. https://doi.org/10.1175/JPO-D-17-0038.1

Okajima, S., Nakamura, H., Nishii, K., Miyasaka, T., & Kuwano-Yoshida, A. (2014). Assessing the importance of prominent warm SST anomalies over the midlatitude north pacific in forcing large-scale atmospheric anomalies during 2011 summer and autumn. *Journal of Climate*. https://doi.org/10.1175/JCLI-D-13-00140.1

O'Neill, L. W., Chelton, D. B., Esbensen, S. K., & Wentz, F. J. (2005). High-resolution satellite measurements of the atmospheric boundary layer response to SST variations along the Agulhas Return Current. *Journal of Climate*, ***18*****(14)**, 2706–2723. https://doi.org/10.1175/JCLI3415.1

Otkin, J. A., & Greenwald, T. J. (2008). Comparison of WRF Model-Simulated and MODIS-Derived Cloud Data. *Monthly Weather Review*, ***136*****(6)**, 1957–1970. https://doi.org/10.1175/2007MWR2293.1

Pan, L.-L., & Li, T. (2008). Interactions between the tropical ISO and midlatitude low-frequency flow. *Climate Dynamics*, ***31*****(4)**, 375–388. https://doi.org/10.1007/s00382-007-0272-7

Paulson, C. A., & Simpson, J. J. (1977). Irradiance Measurements in the Upper Ocean. *Journal of Physical Oceanography*, ***7*****(6)**, 952–956. https://doi.org/10.1175/1520-0485(1977)007<0952:IMITUO>2.0.CO;2

Platnick, S. (2015). MYD08 _ D3 - MODIS / Aqua Aerosol Cloud Water Vapor Ozone Daily L3 Global 1Deg CMG. https://doi.org/10.5067/MODIS/MYD08_D3.061

Power, S., Casey, T., Folland, C., Colman, A., & Mehta, V. (1999). Inter-decadal modulation of the impact of ENSO on Australia. *Climate Dynamics*, ***15*****(5)**, 319–324.

https://doi.org/10.1007/s003820050284

Qiu, B., & Kelly, K. A. (1993). Upper-Ocean Heat Balance in the Kuroshio Extension Region. *Journal of Physical Oceanography*, ***23*****(9)**, 2027–2041. https://doi.org/10.1175/1520-0485(1993)023<2027:UOHBIT>2.0.CO;2

Qiu, B. (2001). Kuroshio and Oyashio Currents. *Encyclopedia of Ocean Sciences: Second Edition*, 1413–1425. https://doi.org/10.1016/B978-012374473-9.00350-7

Qiu, B., Chen, S., & Schneider, N. (2017). Dynamical links between the decadal variability of the Oyashio and Kuroshio Extensions. *Journal of Climate*, ***30*****(23)**, 9591–9605. https://doi.org/10.1175/JCLI-D-17-0397.1

Qu, X., Hall, A., Klein, S. A., & Caldwell, P. M. (2014). On the spread of changes in marine low cloud cover in climate model simulations of the 21st century. *Climate Dynamics*, ***42*****(9–10)**, 2603–2626. https://doi.org/10.1007/s00382-013-1945-z

Qu, X., Hall, A., Klein, S. A., & DeAngelis, A. M. (2015). Positive tropical marine low-cloud cover feedback inferred from cloud-controlling factors. *Geophysical Research Letters*, ***42*****(18)**, 7767–7775. https://doi.org/10.1002/2015GL065627

Radel, G., Mauritsen, T., Stevens, B., Dommenget, D., Matei, D., Bellomo, K., & Clement, A. (2016). Amplification of El Nino by cloud longwave coupling to atmospheric circulation. *Nature Geoscience*, ***9*****(2)**, 106–110. https://doi.org/10.1038/ngeo2630

Ramanathan, V., Cess, R. D., Harrison, E. F., Minnis, P., Barkstrom, B. R., Ahmad, E., & Hartmann, D. (1989). Cloud-radiative forcing and climate: Results from the earth radiation budget experiment. *Science*, ***243*****(4887)**, 57–63. https://doi.org/10.1126/science.243.4887.57

Reynolds, R. W., Rayner, N. A., Smith, T. M., Stokes, D. C., & Wang, W. (2002). An improved in situ and satellite SST analysis for climate. *Journal of Climate*. https://doi.org/10.1175/1520-0442(2002)015<1609:AIISAS>2.0.CO;2

Roemmich, D., & Gilson, J. (2009). The 2004-2008 mean and annual cycle of temperature, salinity, and steric height in the global ocean from the Argo Program. *Progress in Oceanography*, ***82*****(2)**, 81–100. https://doi.org/10.1016/j.pocean.2009.03.004

Schmidtko, S., Johnson, G. C., & Lyman, J. M. (2013). MIMOC: A global monthly isopycnal upper-ocean climatology with mixed layers. *Journal of Geophysical Research: Oceans*, ***118*****(4)**, 1658–1672. https://doi.org/10.1002/jgrc.20122

Seethala, C., Norris, J. R., & Myers, T. A. (2015). How Has Subtropical Stratocumulus and Associated Meteorology Changed since the 1980s?*. *Journal of Climate*, ***28*****(21)**, 8396–8410. https://doi.org/10.1175/JCLI-D-15-0120.1

Skamarock, W.C., Klemp, J. B., Dudhia, J., Gill, D. O., Zhiquan, L., Berner, J., et al. (2019). A Description of the Advanced Research WRF Model Version 4 NCAR Technical Note. *National Center for Atmospheric Research*, 145. https://doi.org/10.5065/1dfh-6p97

Skamarock, William C., & Klemp, J. B. (2008). A time-split nonhydrostatic atmospheric model for weather research and forecasting applications. *Journal of Computational Physics*, ***227*****(7)**, 3465–3485. https://doi.org/10.1016/j.jcp.2007.01.037

Skamarock, William C., Klemp, J. B., Dudhia, J., Gill, D. O., Barker, D. M., Wang, W., & Powers, J. G. (2008). A Description of the Advanced Research WRF Version 3. *National Center for Atmospheric Research*. https://doi.org/https://opensky.ucar.edu/islandora/object/technotes:500

Small, R. J., DeSzoeke, S. P., Xie, S. P., O'Neill, L., Seo, H., Song, Q., et al. (2008). Air–sea interaction over ocean fronts and eddies. *Dynamics of Atmospheres and Oceans*, ***45*****(3–4)**, 274–319. https://doi.org/10.1016/j.dynatmoce.2008.01.001

Smirnov, D., Newman, M., Alexander, M. A., Kwon, Y. O., & Frankignoul, C. (2015). Investigating the local atmospheric response to a realistic shift in the Oyashio sea surface temperature front. *Journal of Climate*. https://doi.org/10.1175/JCLI-D-14-00285.1

Sugimoto, S., Kobayashi, N., & Hanawa, K. (2014). Quasi-Decadal Variation in Intensity of the Western Part of the Winter Subarctic SST Front in the Western North Pacific: The Influence of Kuroshio Extension Path State. *Journal of Physical Oceanography*. https://doi.org/10.1175/JPO-D-13-0265.1

Takahashi, N. & Hayasaka, T. Air-sea interactions among oceanic low-level cloud, sea surface temperature, and atmospheric circulation on intra-seasonal timescale in summertime North Pacific based on satellite data analysis. under review in *Journal of Climate*.

Tanimoto, Y., Nakamura, H., Takashi Kagimoto, & Shozo Yamane. (2003). An active role of extratropical sea surface temperature anomalies in determining anomalous turbulent heat flux. *Journal of Geophysical Research*, ***108*****(C10)**, 3304. https://doi.org/10.1029/2002JC001750

Tanimoto, Y., Xie, S. P., Kai, K., Okajima, H., Tokinaga, H., Murayama, T., et al. (2009). Observations of marine atmospheric boundary layer transitions across the summer Kuroshio extension. *Journal of Climate*, ***22*****(6)**, 1360–1374. https://doi.org/10.1175/2008JCLI2420.1

Tanimoto, Y., Kanenari, T., Tokinaga, H., & Xie, S. P. (2011). Sea level pressure minimum along the Kuroshio and its extension. *Journal of Climate*. https://doi.org/10.1175/2011JCLI4062.1

Terai, C. R., Klein, S. A., & Zelinka, M. D. (2016). Constraining the low-cloud optical depth feedback at middle and high latitudes using satellite observations. *Journal of Geophysical Research: Atmospheres*, ***121*****(16)**, 9696–9716. https://doi.org/10.1002/2016JD025233

Terai, C. R., Zhang, Y., Klein, S. A., Zelinka, M. D., Chiu, J. C., & Min, Q. (2019). Mechanisms Behind the Extratropical Stratiform Low-Cloud Optical Depth Response to Temperature in ARM Site Observations. *Journal of Geophysical Research: Atmospheres*, ***124*(4)**, 2127–2147. https://doi.org/10.1029/2018JD029359

Thompson, G., Field, P. R., Rasmussen, R. M., & Hall, W. D. (2008). Explicit Forecasts of Winter Precipitation Using an Improved Bulk Microphysics Scheme. Part II: Implementation of a New Snow Parameterization. *Monthly Weather Review*, ***136*(12)**, 5095–5115. https://doi.org/10.1175/2008MWR2387.1

Tokinaga, H., Tanimoto, Y., Xie, S. P., Sampe, T., Tomita, H., & Ichikawa, H. (2009). Ocean frontal effects on the vertical development of clouds over the western North Pacific: In situ and satellite observations. *Journal of Climate*, ***22*(16)**, 4241–4260. https://doi.org/10.1175/2009JCLI2763.1

Tozuka, T., & Cronin, M. F. (2014). Role of mixed layer depth in surface frontogenesis: The Agulhas Return Current front. *Geophysical Research Letters*, ***41*(7)**, 2447–2453. https://doi.org/10.1002/2014GL059624

Tozuka, T., Cronin, M. F., & Tomita, H. (2017). Surface frontogenesis by surface heat fluxes in the upstream Kuroshio Extension region. *Scientific Reports*, ***7*(1)**, 1–9. https://doi.org/10.1038/s41598-017-10268-3

Tozuka, T., Ohishi, S., & Cronin, M. F. (2018). A metric for surface heat flux effect on horizontal sea surface temperature gradients. *Climate Dynamics*, ***51*(1–2)**, 547–561. https://doi.org/10.1007/s00382-017-3940-2

Wang, L., Li, T., & Zhou, T. (2012). Intraseasonal SST Variability and Air–Sea Interaction over the Kuroshio Extension Region during Boreal Summer*. *Journal of Climate*, ***25*(5)**, 1619–1634. https://doi.org/10.1175/JCLI-D-11-00109.1

Wang, L., Li, T., Zhou, T., & Rong, X. (2013). Origin of the intraseasonal variability over the north pacific in boreal summer. *Journal of Climate*, ***26*(4)**, 1211–1229. https://doi.org/10.1175/JCLI-D-11-00704.1

Wei, W., Li, W., Deng, Y., Yang, S., Jiang, J. H., Huang, L., & Liu, W. T. (2018). Dynamical and thermodynamical coupling between the North Atlantic subtropical high and the marine boundary layer clouds in boreal summer. *Climate Dynamics*. https://doi.org/10.1007/s00382-017-3750-6

Wielicki B. A., B. A., Barkstrom, B. R. Harrison, E. F. Lee, R. B., et al. (1996). Clouds and the Earth's Radiant Energy System (CERES): An Earth Observing System Experiment. *Bulletin of the American Meteorological Society*, ***77*(5)**, 853–868.

Wild, M., Folini, D., Schär, C., Loeb, N., Dutton, E. G., & König-Langlo, G. (2013). The global energy balance from a surface perspective. *Climate Dynamics*, ***40*****(11–12)**, 3107–3134. https://doi.org/10.1007/s00382-012-1569-8

Wood, R., & Bretherton, C. S. (2006). On the Relationship between Stratiform Low Cloud Cover and Lower-Tropospheric Stability. *Journal of Climate*, ***19*****(24)**, 6425–6432. https://doi.org/10.1175/JCLI3988.1

Wood, R. (2012). Stratocumulus Clouds. *Monthly Weather Review*, ***140*****(8)**, 2373–2423. https://doi.org/10.1175/MWR-D-11-00121.1

Wu, B., Lin, X., & Qiu, B. (2018). Meridional Shift of the Oyashio Extension Front in the Past 36 Years. *Geophysical Research Letters*, ***45*****(17)**, 9042–9048. https://doi.org/10.1029/2018GL078433

Wu, R., & Kinter, J. L. (2010). Atmosphere-ocean relationship in the midlatitude North Pacific: Seasonal dependence and east-west contrast. *Journal of Geophysical Research Atmospheres*, ***115*****(6)**, 1–12. https://doi.org/10.1029/2009JD012579

Xie, S. (2004). Satellite Observations of Cool Ocean–Atmosphere Interaction. *Bulletin of the American Meteorological Society*, ***85*****(2)**, 195–208. https://doi.org/10.1175/BAMS-85-2-195

Xu, H., Xie, S., & Wang, Y. (2005). Subseasonal Variability of the Southeast Pacific Stratus Cloud Deck*. *Journal of Climate*, ***18*****(1)**, 131–142. https://doi.org/10.1175/JCLI3250.1

Xu, H., Tokinaga, H., & Xie, S. P. (2010). Atmospheric effects of the Kuroshio large meander during 2004-05. *Journal of Climate*. https://doi.org/10.1175/2010JCLI3267.1

Yasunari, T. (1979). Cloudiness Fluctuations Associated with the Northern Hemisphere Summer Monsoon. *Journal of the Meteorological Society of Japan. Ser. II*, ***57*****(3)**, 227–242. https://doi.org/10.2151/jmsj1965.57.3_227

Yu, L., Jin Xiangze, & Weller, A. R. (2008). *Multidecade Global Flux Datasets from the Objectively Analyzed Air-sea Fluxes (OAFlux) Project: Latent and Sensible Heat Fluxes, Ocean Evaporation, and Related Surface Meteorological Variables*. *Woods Hole Oceanographic Institution OAFlux Project Technical Report (OA-2008-01)*. https://doi.org/10.1007/s00382-011-1115-0

Zelinka, M. D., & Hartmann, D. L. (2012). Climate feedbacks and their implications for poleward energy flux changes in a warming climate. *Journal of Climate*, ***25*****(2)**, 608–624. https://doi.org/10.1175/JCLI-D-11-00096.1

Zelinka, M. D., Grise, K. M., Klein, S. A., Zhou, C., DeAngelis, A. M., & Christensen, M. W. (2018). Drivers of the Low-Cloud Response to Poleward Jet Shifts in the North Pacific in

Observations and Models. *Journal of Climate*, ***31*(19)**, 7925–7947. https://doi.org/10.1175/JCLI-D-18-0114.1

Zhai, C., Jiang, J. H., & Su, H. (2015). Long-term cloud change imprinted in seasonal cloud variation: More evidence of high climate sensitivity. *Geophysical Research Letters*, ***42*(20)**, 8729–8737. https://doi.org/10.1002/2015GL065911

Acknowledgements

First of all, I would like to appreciate all the people who supported me during the course in Tohoku University.

I am grateful to Dr. T. Hayasaka for teaching me a fundamental basis of radiative transfer theory and cloud physics, and supervising my researches with many valuable discussions, constructive suggestions, enormous encouragements throughout the course. I acknowledge Dr. H. Iwabuchi for providing me many important comments about cloud physical process from a wide variety of viewpoints. I would like to offer my special thanks to Dr. K. Richards, Dr. B. Qiu, and Dr. N. Schneider of University of Hawaii at Manoa for giving me valuable suggestions about oceanography. I also thank to them for their kind hospitality during my stay in Hawaii. I appreciate the insightful feedback offered by Dr. T. Suga of Tohoku University, Dr. R. Yamaguchi of Pusan National University, Dr. J. Norris and Dr. SP. Xie of of University of California San Diego, Dr. A. Manda of Mie University, Dr. H. Okamoto of Kyushu University, and Dr. H. Kawai of Meteorological Research Institute. I also appreciate Dr. T. Yamazaki and other committee members for their time and helpful comments. Sincere gratitude goes to Dr. S. Katagiri of Kyushu University, Dr. M. K. Yoshioka of Nagoya University, Dr. P. Khatri of Tohoku University, Dr. K. Yamada of Nagano Prefectural Office, Dr. M. Saito of Texas A&M University for teaching me a basis of computers utilization and encouraging my studies. I also thank to the assistance by Ms. K. Akimoto. I would like to express my gratitude to Ms. Murni, Ms. X. Wang, Mr. M. Amma, Mr. H. Ooashi, Mr. T. Yamashita, Mr. T. Sato, Ms. H. Kato, Ms. A. Masuda, and all past and present members of the Radiation and Climate Physics laboratory in Tohoku University for their warm attitude and conversations.

This work was supported by a Grant-in-Aid from the Japan Society for the Promotion of Science (JSPS), Research Fellow JP18J10606 and Grant-in-Aid for Scientific Research B JP16H04046. I also acknowledge support from the International Joint Graduate Program in Earth and Environmental Science (GP-EES) and Tohoku University Division for Interdisciplinary Advanced Research and Education with continuous supports from Ms. S. Okuyama, Dr. S. Ozawa, and all the past and present member associated with the program.

Thank are extend to all of the research institute that provided me the datasets we used in this study. The Aqua/MODIS Cloud Daily L2 and L3 Global 1 Deg. The CMG dataset was acquired from the Level-1 and Atmosphere Archive Distribution System (LAADS) Distributed Active Archive Center (DAAC), located in the Goddard Space Flight Center in Greenbelt, Maryland, USA (https://ladsweb.nascom.nasa.gov/). CERES data were obtained from the NASA Langley Research Center CERES ordering tool at http://ceres.larc.nasa.gov/. OISST data were provided by the National Oceanic and Atmospheric Administration (NOAA). The global ocean heat flux and evaporation data were provided by the WHOI OAFlux project (http://oaflux.whoi.edu/, last access: 6 November 2018) funded by the NOAA Climate Observations and Monitoring (COM) program. ERA-Interim data were downloaded from the European Centre for Medium-Range Weather Forecasts (ECMWF) data server at http://apps.ecmwf.int/datasets/.

Finally, I would like to express special thanks to my parents Toshiaki and Hiroko Takahashi, and all the friends of mine for their supports and hearty encouragement throughout my daily life during the course.